THE STRUCTURE AND REACTIONS OF NEUTRON-RICH NUCLEI

Carlos A. BERTULANI

National Superconducting Cyclotron Laboratory, Michigan State University, East Lansing, MI 48824-1321, USA

L. Felipe CANTO

Instituto de Física, Universidade Federal do Rio de Janeiro, 21945 Rio de Janeiro, R.J., Brazil

and

Mahir S. HUSSEIN

Nuclear Theory and Elementary Particle Phenomenology Group, Instituto de Física da Universidade de São Paulo, C.P. 20516, 01498 São Paulo, S.P., Brazil

NORTH-HOLLAND

PHYSICS REPORTS (Review Section of Physics Letters) 226, No. 6 (1993) 281–376.
North-Holland

PHYSICS REPORTS

The structure and reactions of neutron-rich nuclei*

Carlos A. Bertulani[a], L. Felipe Canto[b] and Mahir S. Hussein[c]

[a] *National Superconducting Cyclotron Laboratory, Michigan State University, East Lansing, MI 48824-1321, USA*
[b] *Instituto de Física, Universidade Federal do Rio de Janeiro, 21945 Rio de Janeiro, R.J., Brazil*
[c] *Nuclear Theory and Elementary Particle Phenomenology Group, Instituto de Física da Universidade de São Paulo, C.P. 20516, 01498 São Paulo, S.P., Brazil*

Received September 1992; editor: G.E. Brown

Contents:

Abstract:

This article aims at reviewing the present status of the understanding of the structure and reactions of neutron-rich nuclei. The properties of the low-lying soft giant dipole resonance in ^{11}Li are discussed within several models proposed for the purpose. The existence of this collective mode in heavier neutron-rich nuclei is considered. The question of the separation energy of a single neutron and a dineutron is discussed.

The nuclear and Coulomb dissociation cross sections for ^{11}Li on several targets are calculated and compared to the available data. The question of the neutron halo is then considered in detail.

The elastic scattering of ^{11}Li and other unstable nuclei on several stable targets (p, ^{208}Pb, etc.) is discussed in detail. The signature of the halo on the elastic cross section σ_{el} is then assessed. Proposed experiments are discussed in the light of the theoretical prediction. The effect of the break-up channel (2n + ^{9}Li in ^{11}Li) on σ_{el} is thoroughly analysed. The total reaction cross section and total nuclear reaction cross section is also calculated using the microscopic $t\rho_1\rho_2$-Glauber theory. The production of π's is considered and model calculations are performed.

The low-energy fusion of neutron-rich nuclei with heavy targets is analysed. Having in mind the possibility that the low-lying soft giant-dipole resonance may greatly aid the system to fuse even at sub-barrier energies, the viability of produing superheavy elements are studied. The astrophysical implications of exotic nuclei are assessed and discussed. Finally, the momentum and angular distributions of fragments from ^{11}Li breakup are calculated and compared to the available data.

* Supported in part by the CNPq-Brazil and the NSF-USA.

1. Introduction

1.1. Generalities

The recent interest in drip-line nuclei only appeared after these nuclei could be studied in nuclear reactions, in particular due to the series of experiments carried out at Berkeley by Tanihata et al. [Ta 85a, b; Ko 88, 89]. Such experiments have also been performed at GANIL and at Michigan State University with intermediate energy beams [Mi 87; SL 89; An 90; Or 92; Ie 93]. In this introduction we shall concentrate on the most relevant aspects of the data and study especially the fragmentation of ^{11}Li. We shall closely follow the ideas discussed by Bertulani and Hussein [BH 90a]. The fragmentation of other neutron-rich nuclei, like ^{14}Be, should follow the same scheme. Among the several distinctive features of the experimental results, an intriguing one is related to the momentum distribution of the ^{9}Li fragments originating in the reaction ^{11}Li + target → ^{9}Li + X. These fragments originate from peripheral reactions and give information about the nuclear matter distribution near the surface of the ^{11}Li isotope. The perpendicular momentum distribution of the ^{9}Li fragments shows a "two-peak" structure [Ta 85a, b], with a narrow peak on top of a wider one (see fig. 1). The widths of gaussian fits to these peaks are given by $\sigma_{\text{wide}} = 95 \pm 12$ MeV/c for the wider peak, and $\sigma_{\text{narrow}} = 23 \pm 5$ MeV/c for the narrower one. Such structure has also been found in the reaction ^{14}Be + target → ^{12}Be + X. In the case of ^{11}Li it is known that the separation energy of the last two neutrons is [Th 75; Wo 88] $S_{2n} = 0.25 \pm 0.08$ MeV, while ^{10}Li is unbound by $S_{1n} = 0.8 \pm 0.25$ MeV.

Hansen and Jonson [HJ 87] have argued that it is the strength of the neutron pairing which is responsible for the differences in the separation energies of ^{11}Li and of other neutron-rich nuclei.

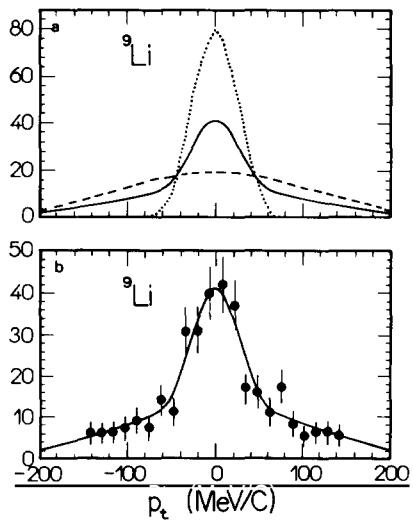

Fig. 1. (a) Calculated transverse momentum distribution of ^{9}Li in the reaction ^{11}Li + ^{12}C → ^{9}Li + 2n + X. The dashed (dotted) line is obtained by assuming knock-out of two neutrons from the core (halo) of ^{11}Li. The solid line represents the weighted sum of the two. (b) Comparison with the experimental data (for more details see chapter 4).

This pairing makes the bond between the two loosely bound neutrons much stronger than the respective bonds between each of them and the ^{9}Li core. That is, the ^{11}Li is much like a cluster nucleus with a dineutron system bound to the ^{9}Li core. In this general introduction we show that both the widths of the momentum distributions as well as the total cross sections can be explained by assuming a simple cluster-like structure for ^{11}Li as a dineutron bound to a ^{9}Li core. But we also show that analogous results can be obtained by considering the excitation of a soft vibration of the protons against the neutrons in ^{11}Li. The presently available data do not unambiguously distinguish between the two models. We also discuss some qualitative three-body dynamical effects in ^{11}Li.

1.2. Reactions of exotic nuclei

Due to the low energy necessary to remove the neutron pair, the reaction process is of peripheral nature. The fragmentation then originates due to the nuclear field when the tails of the nucleonic distributions just touch each other, or the Coulomb field even when the nuclei pass several tens of fermis far from each other. The scattering angle θ is therefore very small, and the momentum transfer in the reaction, Δp, is related to energy transfer by

$$\Delta p = p_f \cos\theta - p_i \cong E^*/v \,, \tag{1.1}$$

where v is the projectile velocity. Since the energy E^* transferred in peripheral processes is typically of order of few MeV, it cannot be absorbed by a single nucleon. The nucleon would carry a momentum $\sim (2mE^*)^{1/2}$, which is appreciably larger than that of eq. (1.1) for $v \sim c$. However, such energy could be absorbed by a nucleon pair, or a pair of clusters, which can have high kinetic energy and small total momentum, when the nucleons move approximately with opposite directions. The relation (1.1) can also be satisfied if collective excitations, like vibrational modes, are excited.

Let us assume that the energy E^* deposited in the nucleus with mass number A leads to its fragmentation into two pieces which fly apart with opposite momenta with the same magnitude p. If one of the fragments has mass number a, the following relations holds

$$E^* - \varepsilon = p^2/2(A-a)m_N + p^2/2am_N \,, \tag{1.2}$$

where m_N is the nucleon mass and ε is the binding energy between the two clusters. The momentum width of the fragments is obtained, after an average of (1.2), as

$$\langle p^2 \rangle = 2m_N \langle K \rangle a(A-a)/A \,, \quad \langle K \rangle = \langle E^* \rangle - \langle \varepsilon \rangle \,, \tag{1.3}$$

with $\langle K \rangle$ the average kinetic energy of the fragments.

This formula is very much like the one obtained by Goldhaber [Go 74] for the momentum width of a fragment of mass number a in the fragmentation of a nucleus of mass number A. No wonder, because both approaches rely on momentum and energy conservation. Goldhaber assumes that the momentum width results from an average of the net momentum obtained by adding the individual momenta of the nucleons inside the fragment at the exact moment it flies off the nucleus. This procedure relates $\langle p^2 \rangle$ to the Fermi momentum P_F of nucleus A. The final result (which assumes $\langle E^* \rangle \sim 0$) is eq. (1.3) with $2m_N\langle K \rangle$ replaced by $\frac{1}{5}P_F^2$.

Since the transferred energy depends on the specification of the target, as well as on the beam energy, then by means of a variation of these parameters the measurement of $\langle p^2 \rangle$ yields valuable information about $\langle E^* \rangle$. In the case of $^{11}\text{Li} \rightarrow {}^{9}\text{Li} + 2\text{n}$, the narrow peak with width $\langle p^2 \rangle^{1/2} = 23 \pm 5\,\text{MeV}/c$, gives $\langle K \rangle = 0.17 \pm 0.08$ MeV, while for the wide peak with width $\langle p^2 \rangle^{1/2} = 95 \pm 12\,\text{MeV}/c$ one obtains $\langle K \rangle = 2.9 \pm 0.8$ MeV. Since the binding energy ε of any pair of neutrons in ^{11}Li cannot be larger than some MeV (one could imagine that at least one of the neutrons comes from the inner part of ^{11}Li, where it is more tightly bound), the above results show that the energy E^* transferred in the process cannot be larger than some MeV, too. This means that the dissociation is very soft and occurs at very large impact parameters, probing the tail of the nuclear matter distribution in ^{11}Li. The average kinetic energy $\langle K \rangle$ associated with the narrow peak is of the same magnitude as the binding energy of the loosely bound neutrons. Then, it may give information about the correlation distance between the dineutron system and the ^{9}Li core, within the cluster-like hypothesis. On the other hand, the wider peak reveals that a more tightly bound neutron is taken out of ^{11}Li. An analysis of the dissociation cross section as a function of the relative final momentum of the fragments confirms the above hypothesis as we show next.

Assuming that the ^{11}Li possesses a binary cluster structure (dineutron + ^{9}Li), one can make simple estimates of the cross sections for its dissociation. Using a deuteron-like wave function for the pair of clusters and a strong absorption model, simple expressions were obtained by Bertulani and Baur [BB 88a]. The nuclear contribution to the differential cross section, in the limit that $q \rightarrow 0$, is obtained as

$$\mathrm{d}\sigma_{\mathrm{N}}/\mathrm{d}q \cong R_{\mathrm{T}} q^2/(\eta^2 + q^2)^2, \tag{1.4}$$

where q is the relative momentum of the clusters after the dissociation, R_{T} is the target radius, and $\eta = \sqrt{2\mu\varepsilon}/\hbar$, with μ equal to the reduced mass of the clusters.

The Coulomb contribution to the differential cross section (taking only the E1-multipole contribution) in the same limit, is given by ref. [BB 88a]

$$\frac{\mathrm{d}\sigma_{\mathrm{C}}}{\mathrm{d}q} = \tfrac{128}{3} Z_{\mathrm{T}}^2 \alpha \left(\frac{c}{v}\right)^2 \left(\frac{Z_1 A_2 - A_1 Z_2}{A}\right)^2 \frac{\eta q^2}{(\eta^2 + q^2)^4} \left(\ln (\gamma v/\delta\omega R)^2 - \frac{v^2}{2c^2} \right), \tag{1.5}$$

where $\gamma = (1 - v^2/c^2)^{-1/2}$ is the relativistic Lorentz factor, $\delta = 0.891$ and $\hbar\omega = \hbar^2(\eta^2 + q^2)/2\mu$. $A_i(Z_i)$ refers to the mass (charge) number of cluster i ($A = A_1 + A_2$) and $R = R_{\mathrm{T}} + R_{\mathrm{P}}$.

The above expressions reveal that the spread in q^2 is of order of $\langle q^2 \rangle \cong \eta^2$. This means that the relative kinetic energy of the clusters after the dissociation has on the average the same value as their binding energies. This is indeed what we obtained above for $\langle K \rangle$ associated with the narrow momentum component. Therefore, the narrow momentum component can be interpreted as originating from the removal of two neutrons weakly bound in ^{11}Li. The root-mean-square radius for ^{11}Li, supposed to be a deuteron-like system, is $\langle r^2 \rangle^{1/2} = (1/\sqrt{2})\eta \sim 5.8$ fm. The experimental value [Ta 85a, b] for the r.m.s. radius of the ^{9}Li core is about 2.5 fm. Therefore, the dineutron system forms a neutron *halo* around the ^{9}Li core.

As has been pointed out by Tanihata [Ta 88], the amount of kinetic energy associated with the broad momentum width ($\sim$ 3 MeV) is related to the binding energy of neutrons in the ^{9}Li core. As in the case of the ^{9}Li + 2n described above, a pair of neutrons in the ^{9}Li core can also absorb the

transferred energy in the reaction with their final relative momentum and energy obeying eq. (1.1). In this case the decay constant η in eqs. (1.4) and (1.5) can be related to the average binding energy of neutrons in the ^{9}Li core as $\eta = \sqrt{m_N \varepsilon_c}/\hbar$. Taking $\varepsilon_c \sim 3$ MeV, this yields a r.m.s radius of about 2.65 fm, which agrees well with the r.m.s. radius of ^{9}Li.

Neutrons coming out of the ^{9}Li core can also originate from its collective excitation. The most effective way of creating such excitations is by means of the Coulomb interaction. It gives the same "kick" to all Z protons inside ^{9}Li, leading to their collective motion. For collisions with impact parameter b, this kick leads to an energy transfer which can easily be calculated as [BB 87a] $\Delta E_1 = 2Z(Z_T e^2)^2/m_N b^2 v^2$, where Z_T is the target charge. But the protons are not free and they pull the neutrons together. This leads to the motion of the whole nucleus, and the Coulomb recoil that one obtains by assuming that the nucleus with mass number A is a rigid body is $\Delta E_2 = 2(ZZ_T e^2)^2/Am_N b^2 v^2$. The difference between these energies goes to the vibration of the Z protons against the N neutrons, and is

$$E^* = \Delta E_1 - \Delta E_2 = 2(NZ/A)(Z_T e^2)^2/m_N b^2 v^2 \,. \tag{1.6}$$

If we assume that only the protons and neutrons in the ^{9}Li participate in these vibrations ($N = 6$, $Z = 3$), and for ^{11}Li beams (0.8 GeV A) incident on Pb, one finds $E^* = 0.26$ MeV in a collision with $b = 15$ fm. This energy is fairly below the excitation energy of giant dipole resonances (GDR) in normal nuclei, which means that the excitation cross section of a giant dipole mode in the ^{9}Li core is small.

Indeed, assuming that this dipole resonance excited on the ^{9}Li core can be accounted for in the same way as a normal giant dipole resonance positioned at E_{GR}, and using the Thomas–Reiche–Kuhn (TRK) sum rule, one finds for the total Coulomb cross section

$$\sigma_{GR} = \frac{2}{\pi} Z_T^2 \alpha \left(\frac{c}{v}\right)^2 \frac{SR}{E_{GR}(\text{MeV})} \left[\xi K_0 K_1 - \frac{v^2 \xi^2}{2c^2}(K_1^2 - K_0^2) \right] \text{mb} \,, \tag{1.7}$$

$$SR = 60\,(NZ/A) \,,$$

where all modified Bessel functions, K_n, are functions of $\xi = E_{GR} R/\gamma\hbar v$, and N, Z and A refer to the neutron, charge and mass number of the ^{9}Li core (6, 3 and 9, respectively). Assuming that the resonance lies in the energy range $E_{GR} = 10$–20 MeV, and for beams with 0.8 GeV A incident on Pb, one finds $\sigma_{GR} \simeq 50$ mb.

One could think of other vibration modes in ^{11}Li, like all protons vibrating against all neutrons, or a ^{9}Li core vibrating against the dineutron system (such type of motion has been recently studied by Suzuki et al. [Ik 88; SI 90], which they called a pygmy resonance). For the former case ($N = 8$, $Z = 3$ and $A = 11$) we find $E^* = 0.29$ MeV, while for the latter case one makes the substitution of Z by $Z^2/(A-2)$ in the equation for ΔE_1 and obtains $E^* = 0.02$ MeV. From these values one sees that it is very improbable that the latter vibration mode could be excited. It is much more reasonable to think that another possible way for the ^{11}Li to absorb energy is by the excitation of vibrations of all protons against all neutrons in it. Due to the existence of the neutron halo, one might think that the protons move almost freely inside the ^{11}Li and that the excitation of such dipole vibrations will occur at very small energies (soft dipole mode). Nonetheless, these conclusions are based on the idea that the coupling of the last two neutrons in ^{11}Li and the core is very

strong. In fact, due to their low separation energy we expect the contrary to be true. Therefore, the excitation of the pigmy resonance might be attainable.

Kobayashi et al. [Ko 89] have measured the total cross section for the dissociation of ^{11}Li (into ^{9}Li + 2n) incident on several targets (Pb, Cu and C) with 0.8 GeV A beams. We shall refer to their particular result for Pb targets which has the advantage of having a large Z, and induces a large Coulomb cross section. They obtained the value $\sigma_C = 1.31 \pm 0.13$ b. In the ^{9}Li + 2n cluster model, the total cross section for direct Coulomb dissociation is obtained by an integration of (1.5) which results in

$$\sigma_{CD} = \tfrac{4}{3}\pi Z_T^2 \alpha^2 \left(\frac{c}{v}\right)^2 \left(\frac{Z_1 A_2 - A_1 Z_2}{A}\right)^2 \frac{1}{\eta^2}\left(\ln(\gamma\hbar v/\delta\varepsilon R)^2 - \frac{v^2}{2c^2}\right). \tag{1.8}$$

For the reaction cited above it gives $\sigma_{CD} \simeq 1.44 \pm 0.3$ b, where the uncertainties are due to the error in the binding energy.

The nuclear contribution to the direct break-up cannot be obtained by an integration of (1.4) because it was based on the impulse approximation, neglecting the interference with an eclipse term. Including such an effect the cross section is well described by the Glauber formula [Gl 55]

$$\sigma_{ND} = \tfrac{1}{6}\pi(2\ln 2 - \tfrac{1}{2})R_T/\eta\,. \tag{1.9}$$

In addition to this (diffractional) dissociation one has to account for the absorption of the 2n system by the target (stripping). The cross section for this process was obtained for the deuteron by Serber [Se 47]. For other cluster-like $a + (A - a)$ nuclei one has

$$\sigma_{NS} = \tfrac{1}{2}\pi(a/A)(R_T/\eta)\,. \tag{1.10}$$

For the reaction ^{11}Li + target $\rightarrow$ ^{9}Li + X one obtains $\sigma_{ND} = 270^{+100}_{-53}$ mb and $\sigma_{NS} = 165^{+63}_{-32}$ mb, respectively. One then sees that the Coulomb dissociation accounts for the main part of the measured cross section, although the nuclear contribution is not negligible. At this point we observe that the Coulomb–nuclear interference in these reactions may be neglected for the following reason. The nuclear contribution to the total cross section can at most come from those impact parameters (from b_{min} to b_{max}) for which the neutron halo of ^{11}Li touches the nuclear matter distribution of Pb. The contribution of the Coulomb field to the total cross section from this interval of impact parameters is, percentually, given by

$$\Delta = \ln(b_{max}/b_{min})/\ln(\gamma\hbar v/\delta\varepsilon b_{min})\,. \tag{1.11}$$

Using typical values of $b_{min} \simeq 10$ fm and $b_{max} \simeq 13$ fm, one finds $\Delta \simeq 5\%$. This means that only about 5% of the Coulomb contribution should interfere with the nuclear contribution. The reason is that, although the fragmentation induced by the Coulomb interaction may be small in a single collision, the interval of impact parameters contributing to the total cross section is very large, up to some hundreds of fermi. Therefore, we can write $\sigma_{total} \simeq \sigma_N + \sigma_C$. Adding the Coulomb dissociation, the nuclear diffraction dissociation, and the stripping cross sections one can reproduce quite well the experimental value of Kobayashi et al. [Ko 89] for the total cross sections for two-neutron removal from secondary beams of ^{11}Li incident on Pb.

If we now restrict our study to the Coulomb contribution to the dissociation, which is the dominant part of the cross sections, we find that the excitation of giant resonances as described above can also lead to large values of the cross sections. In fact, if we assume that the energy of excitation, E_{GR}, of a soft vibration mode in ^{11}Li is of order of 1 MeV, and that the contribution of this soft mode to the sum rule SR is of about 10%, we find (using $N = 8$, $Z = 3$ and $A = 11$) $\sigma_{GR} \simeq 1.3$ b. Due to its low binding energy, one of the main channels for the decay of this resonance must be the emission of the two neutrons. This indicates that the excitation of this soft dipole mode is another possible mechanism to explain the narrow momentum component in the data for $^{11}\text{Li} \rightarrow {}^{9}\text{Li} + \text{X}$, as well as the total cross section for the fragmentation.

From the present available data it seems impossible to find out whether the fragmentation $^{11}\text{Li} \rightarrow {}^{9}\text{Li} + \text{X}$ in secondary beam reactions proceeds via the direct break-up of a two-cluster system or by the excitation of a soft dipole mode. But note that the two mechanisms assume very distinct structures for ^{11}Li. The direct breakup assumes that the dissociation is a simple transition to the free continuum, while the excitation of a soft dipole mode is a sequential process for which the dissociation time depends on the width of this state. Since the Coulomb kick to the protons does not depend on either hypothesis, only one of the two mechanisms could be responsible for the measured cross sections. Due to the large errors in the knowledge of the binding energy of two neutrons in ^{11}Li, and also due to lack of information about the energy location as well as of the strength of the photonuclear cross section for ^{11}Li at the energies involved, precise theoretical calculations based on either of these models are not conclusive, and the agreement with the experimental data is not unique. Certainly, more experimental results and theoretical discussions are needed in order to determine which of the nuclear models are adequate.

The questions raised above are just examples of the subtle richness of reactions involving radioactive secondary beams. In the next sections of this chapter we make a closer inspection of the reaction mechanisms and nuclear models necessary to explain the reaction cross sections in radioactive secondary beam interactions.

1.3. Three-body considerations of the structure of exotic nuclei

It is obvious from the discussion presented in section 1.2 that subtle three-body dynamics is involved in generating the halo structure of ^{11}Li. In particular, we remind the reader that a bound 2n system in free space does not exist, a bound $^{9}\text{Li} + \text{n}$ system does not exist, and yet the $^{9}\text{Li} + 2\text{n}$ system is bound, albeit slightly. Migdal [Mi 73], back in 1973, addressed a question related to the above. It is of importance to reexamine the above, and eventually to understand the mechanism that generates the effective binding of the halo dineutron system in ^{11}Li. The purpose of this subsection is to summarize the recent study of Frederico and Hussein [FH 93] concerning the above questions.

Let us for the moment, take ^{9}Li to be structureless. The Hamiltonian that describes ^{11}Li then is given by

$$H = H_0 + U_{\text{n}^9\text{Li}} + U_{\text{n}'^9\text{Li}} + V_{\text{nn}'} , \tag{1.12}$$

where $U_{\text{n}^9\text{Li}}$ is the mean field felt by neutron n, and $V_{\text{nn}'}$ is the nn′ interaction (we call the two halo neutrons n and n′). The background Hamiltonian H_0 contains the kinetic-energy operators of the assumed structureless three particles. In what follows, we use arguments given by Landau and Lifshitz [LL 75] and Efimov [Ef 70; 81].

If the nn′ system forms a quasibound state, then the wave function of the bound ^{9}Li + 2n system is given by

$$\psi_{^{11}\mathrm{Li}(^9\mathrm{Li}+2\mathrm{n})} \approx \varphi(\boldsymbol{R})(\mathrm{e}^{-\alpha r}/r)\sqrt{\alpha/2\pi} \equiv \varphi(R)\psi_{2\mathrm{n}} , \tag{1.13}$$

where R is the distance between the core and the center of mass of the dineutron and r is the relative coordinate of the 2n system. α is related to the binding energy $\varepsilon_{2\mathrm{n}}$ of the 2n system, vis. $\alpha = (m_{\mathrm{N}}\varepsilon_{2\mathrm{n}}/\hbar^2)^{1/2}$.

The effective Schrödinger equation for $\varphi(\boldsymbol{R})$ is then obtained by multiplying the full three-body Schrödinger equation $H\psi_{^{11}\mathrm{Li}} = E\psi_{^{11}\mathrm{Li}}$ from the left by $\psi_{2\mathrm{n}}(\boldsymbol{r})$ and integrating over $\boldsymbol{r}$,

$$-\frac{\hbar^2}{2\mu_{\mathrm{N}}}\nabla_R^2\varphi(\boldsymbol{R}) + \frac{\alpha}{2\pi}\int \mathrm{d}^3r\,\frac{\mathrm{e}^{-2\alpha r}}{r^2}\left[U_{\mathrm{n}A}(|\boldsymbol{R}+\tfrac{1}{2}\boldsymbol{r}|) + U_{\mathrm{n}'A}(|\boldsymbol{R}-\tfrac{1}{2}\boldsymbol{r}|)\right]\varphi(\boldsymbol{R})$$

$$= (E - \alpha^2\hbar^2/m_{\mathrm{N}})\varphi(\boldsymbol{R}) , \tag{1.14}$$

$$\mu \equiv \tfrac{18}{11}m_{\mathrm{N}} .$$

Therefore an effective dineutron–core interaction can be defined from the above equation by

$$U_{\mathrm{eff}}(R) = (\alpha/2\pi)\int \mathrm{d}^3r(\mathrm{e}^{-2\alpha r}/r^2)[U_{\mathrm{n}A}(|\boldsymbol{R}+\tfrac{1}{2}\boldsymbol{r}|) + U_{\mathrm{n}'A}(|\boldsymbol{R}-\tfrac{1}{2}\boldsymbol{r}|)] \tag{1.15}$$

$$\approx U_{\mathrm{n}}(R) + (1/8\alpha^2)U_{\mathrm{n}}(R)/R . \tag{1.16}$$

Equation (1.16) was obtained by taking the limit $R/r \gg 1$ and keeping the lowest-order term. No restriction on the value of α was assumed. In the limit $\alpha \to 0$, however, a different effective interaction is obtained [TDA 87],

$$U^{(2)}_{\mathrm{eff}}(R) \approx \frac{\alpha}{\pi}\frac{1}{R^2}\int \mathrm{d}^3r\,[U_{\mathrm{n}A}(r) + U_{\mathrm{n}'A}(r)]\left(1 + \frac{4}{3}\frac{\langle r^2\rangle}{R^2} + \frac{16}{3}\frac{\langle r^2\rangle^2}{R^4} + \frac{64}{9}5\frac{\langle r^2\rangle^3}{R^6} + \cdots\right), \tag{1.17}$$

where $\langle r^2\rangle^{1/2}$ is the r.m.s. radius of ^{9}Li.

In obtaining eq. (1.17), the following steps were followed ($\alpha \to 0$):

$$\int \mathrm{d}r\,\frac{\mathrm{e}^{-2\alpha r}}{r^2}U(|\boldsymbol{R}+\tfrac{1}{2}\boldsymbol{r}|) = \int 8\mathrm{d}\xi\,\frac{\mathrm{e}^{-4\alpha|\xi-R|}}{4|\xi-R|}U(\xi) \simeq 2\int \mathrm{d}\xi\,\frac{1}{R^2}\left[1 + \frac{1}{3}\left(\frac{2\xi}{R}\right)^2 + \cdots\right]U(\xi) .$$

The terms odd in $\xi\cdot\hat{\boldsymbol{R}}$ average to zero.

A similar treatment is applied to $\int \mathrm{d}r(\mathrm{e}^{-2\alpha r}/r^2)U(|\boldsymbol{R}+\tfrac{1}{2}\boldsymbol{r}|)$.

The radial Schrödinger equation for the radial component of $\varphi(\boldsymbol{R})$, $\varphi(R)$, then takes the form

$$[-\mathrm{d}^2/\mathrm{d}R^2 + U_{\mathrm{eff}}(R)]\varphi(R)/R = (2\mu/\hbar^2)\varepsilon\varphi(R)/R , \tag{1.18}$$

where ε is the binding energy of the 2n–^{9}Li system, which we drop.

With eq. (1.17) the effective potential $U_{\rm eff}(R)$ becomes, to leading order,

$$U_{\rm eff}(R) \cong -\lambda/R^2 \quad \text{for large enough } R\,, \tag{1.19}$$

$$\lambda = \tfrac{18}{11} m_{\rm N} \frac{2\alpha}{\hbar^2 \pi} \int {\rm d}^3 r\,[|U_{{\rm n}A}(r)| + |U_{{\rm n}',A}(r)|] - l(l+1), \quad U_{{\rm n}A} = -|U_{{\rm n}A}|\,. \tag{1.20}$$

The solution to eq. (1.18) is given in Landau and Lifshitz and we give here the results. If $\lambda > \frac{1}{4}$, the potential $U_{\rm eff}$ produces an infinite number of bound states condensed at zero energy. This condition on the value of λ, supplies us with the following condition on the parameter α:

$$\alpha > \tfrac{11}{18} \cdot \tfrac{1}{8} \hbar^2 \pi [1 + 4l(l+1)] \left(m_{\rm N} \int {\rm d}^3 r\,[|U_{{\rm n}A}(r)| + |U_{{\rm n}',A}(r)|] \right)^{-1}\,. \tag{1.21}$$

Using (1.21) we can estimate the value of the binding energy of the ^{11}Li nucleus. The volume integral $\int {\rm d}^3 r\,|U_{{\rm n}A}(r)|$ is calculated by taking for $|U_{{\rm n}A}| = U_0 \rho_A(r)/\rho_A(0)$ with $U_0 = 50$ MeV and $\rho_A(r)$ being the matter density of ^{9}Li, which we take to be a Gaussian $\rho_A(r) = \rho_A(0) \exp(-r^2/a^2)$. From the Hartree–Fock calculation of Bertsch et al. [BBS 89], we have verified that the Gaussian form for ρ_A is quite reasonable. The r.m.s. radius of ^{9}Li is taken to be 2.224 fm. This then fixes $a = \sqrt{2/3} \cdot 2.224 = 1.82$ fm. The value of the volume integral thus comes out to be $U_0(\pi a^2)^{3/2} = 1667$ MeV fm^3.

Writing now $\alpha = [2(m_{\rm N}/2)\varepsilon_{2n}/\hbar^2]^{1/2}$, where $m_{\rm N}/2$ is the reduced mass of the dineutron, we have from eq. (1.21)

$$\varepsilon_{2n} > \left(\frac{11}{18}\right)^2 \left(\frac{\hbar^2}{m_{\rm N}}\right) \frac{\tfrac{3}{4}\pi^2 [1 + 4l(l+1)]^2}{16^2 [U_0(\pi a^2)^{3/2}]^2}\,({\rm keV})\,, \tag{1.22}$$

or

$$\varepsilon_{2n} > 0.379[1 + 4l(l+1)]^2\,({\rm keV})\,. \tag{1.23}$$

Note that the orbital angular momentum, l, refers to that of the Rydberg state.

Note further that taking approximately into account the higher-order terms in $U^{(2)}_{\rm eff}$, eq. (1.17), by replacing R which appears inside the large parentheses by the radius of the halo ($\sim$ 8 fm), results in lowering the numerical factor in eq. (1.23), from 0.379 to 0.379/1.40 = 0.271. We have finally

$$\varepsilon_{2n} > 0.271[1 + 4l(l+1)]^2\,({\rm keV})\,. \tag{1.24}$$

It is interesting to mention at this point that the experimentally determined value of the dineutron pairing energy is about 870 KeV. This fact together with eqs. (1.23) and (1.24) points out that the observed halo-like structure of the ground state of ^{11}Li may be a Rydberg state with a relative angular-momentum content of 0, 1, 2 and 3! (see table 1).

A "normal" ^{11}Li nucleus, mainly describable with the usual spherical shell model, would have the dineutron system occupying the $1p_{1/2}$ single particle level. There seems to be acting here a very intriguing mechanism that makes the 2n system occupy partially the $1d_{5/2}$ level or even the $1f_{7/2}$ level (of course we cannot be assured of the value of the total angular momentum j).

Table 1
Lower bounds on the dineutron energy versus orbital angular momentum. $\varepsilon_{2n}^{(1)}$ refers to eq. (1.22) while $\varepsilon_{2n}^{(2)}$ refers to eq. (1.23). The experimental dineutron pairing energy is 870 keV

l	$\varepsilon_{2n}^{(1)}$ (keV)	$\varepsilon_{2n}^{(2)}$ (keV)
0	0.379	0.271
1	30.699	24.661
2	236.875	169.375
3	909.98	650.671
4	2486.62	1778.031

To recapitulate, we see from the above discussion that just a slight change in the binding energy of the dineutron is enough to produce these Rydberg states in ^{11}Li. It would also seem possible that other Rydberg states with lower binding energies would appear in the ^{11}Li nucleus due to the long-range nature of the effective potential. Finally, it is found that values of the orbital angular momentum of up to $3\hbar$ may contribute to the structure of the ground state.

We should stress that the Pauli principle between the neutron and the core is taken into account in the n–core interaction potential; the n–n state is in the singlet S state and the Pauli principle is satisfied. The only contribution from the Pauli principle that we do not include is the one from the part of the three-body wave function where the two neutrons are simultaneously inside the core. But because we are considering weakly bound states this component of the wave function must be very small and consequently does not give rise to major changes in our results.

Before ending, we mention that extensive three-body calculations for ^{11}Li and other light exotic nuclei have appeared recently in the literature. In particular we mention the work of Esbensen and Bertsch [EB 92], Bang et al. [Ba 92], Johannsen et al. [JJH 90] and Zhukov et al. [Zh 91a, b].

2. Reaction cross section

2.1. Cluster model

As has been already mentioned, the fragmentation of neutron-rich nuclei has led to many unusual speculative ideas about their structure. Perhaps, the most interesting one is due to Hansen and Jonson [HJ 87], who proposed a cluster-like structure for ^{11}Li as composed of a dineutron system loosely bound to a ^{9}Li core. This hypothesis has had general support from several other authors [Mi 73; BB 88a; BH 90a; TS 90; JJH 90]. It seems that such a cluster structure occurs very often in light neutron-rich nuclei and results from a delicate balance between the neutron–neutron and neutron–core interactions [Mi 73]. The Hansen–Jonson model is supported by several facts. Firstly, the separation energy of two neutrons from ^{11}Li is very low [Th 75; Wo 88], $S_{2n} = 250 \pm 80$ KeV. Otherwise, the nucleus ^{10}Li would not exist [Wi 75], having a resonant continuum state at 800 ± 250 KeV. This means that the neutron–neutron interaction acquires a stronger attractive character in the presence of the ^{9}Li core. Secondly, the measurements of total reaction cross sections [Ko 89] of neutron-rich nuclei incident on several targets at 0.8 GeV A reveal a r.m.s. radius of 3.14 ± 0.06 fm for ^{11}Li, compared to a r.m.s. radius of 2.41 ± 0.02 fm for ^{9}Li. A large increase of the matter radius from ^{12}Be to ^{14}Be, and possibly from ^{15}B to ^{17}B, is also observed. The last two neutrons are responsible for the unusual increase of the matter radius and

for the appearance of a "neutron halo" in these nuclei. In the cluster model the existence of such a halo can be easily explained as due to the low binding energy of the dineutron system. In fact, by assuming a deuteron-like wave function for ^{11}Li and adjusting it to reproduce the binding energy of the dineutron system, an approximate r.m.s. distance of the dineutron to the core of 6 fm is obtained. This would essentially explain the r.m.s. radius of ^{11}Li as roughly given by $\frac{2}{11}R^{(2n)}_{\text{m.s.}} + \frac{9}{11}R^{(9)}_{\text{m.s.}} = 2\times 6/11 + 9\times 2.41/11 \cong 3.1$ fm.

Another support for the cluster model for ^{11}Li is that the experimentally determined [Ko 89] electromagnetic dissociation cross sections for ^{11}Li can be well described theoretically [HJ 87; BB 88a; BH 90a; TS 90; JJH 90]. The momentum distribution of the ^{9}Li fragments also fits well within this model, as shown in the last section. On the other hand, conventional shell-model calculations performed by Bertsch and collaborators [BF 89; BBS 89; BE 90] were able to produce an amount of electric dipole strength in ^{11}Li which is about 20% less than the reported value of the electromagnetic dissociation cross section of 0.9 b. The above result was obtained with a very small value of the binding of the $1P_{1/2}$ level. As concluded by Bertsch and Foxwell [BF 89], it may be essential to take cluster aspects into account. The still remaining difference between model calculations leading to 0.7 b and the reported experimental value of 0.9 b has led Bertsch et al. [BE 90] to question whether the experimental values of the electromagnetic dissociation cross sections [Ko 89] have been correctly extracted from the total cross sections.

Kobayashi et al. [Ko 89] assume that the nuclear cross section scales as $\sigma_N = 2\pi(R_P + R_T)\Delta$ which is characteristic of a peripheral process concentrated in a small ring of width Δ at the surface of the projectile. By adjusting the parameters of this scalling law for ^{12}C targets, where the Coulomb contribution to the total cross section is negligible, the "experimental" values of σ_N were obtained for other targets, and the Coulomb contribution σ_C to the cross section was inferred by subtraction. But since ^{11}Li has a long tail in its matter distribution, such a procedure is dubious. Assuming that the target is a "black disk", the nuclear striping of the outer nucleons in ^{11}Li should be

$$\sigma_N \sim 2\pi(R_P + R_T)\Delta P(R_T)\,, \tag{2.1}$$

where $P(R_T)$ is the probability that the outer neutrons will be removed from ^{11}Li. Due to long matter tail, this probability is not independent of R_T. Actually it should be approximately proportional to the area A of overlap between the target and the neutron halo in ^{11}Li. From simple geometrical considerations it is possible to show that $A \propto R_T$. That is, σ_N should increase like R_T^2, which has also as a consequence that σ_C^{exp} should be smaller than the values determined by Kobayashi et al. [Ko 89], and would come closer to the RPA calculations of Bertsch and Foxwell [BF 89] and Teruya et al. [Te 91] for σ_C. This is indeed a very relevant point since the electromagnetic dissociation of neutron-rich nuclei reveals important aspects of their intrinsic structure.

We analyse the interplay of the nuclear and the Coulomb interaction in the reaction process

$$^{11}\text{Li} + \text{target} \rightarrow {}^{9}\text{Li} + \text{anything}\,, \tag{2.2}$$

at kinetic energies of 800 MeV A, following the discussions by Bertulani, Baur and Hussein [BBH 91]. As shown in the last section the nuclear–Coulomb interference for the process (2.2) should be at most 5% of the total cross section. Then, we may write the cross section as

$$\sigma = \sigma_D^{(N)} + \sigma_S^{(N)} + \sigma_C\,, \tag{2.3}$$

where $\sigma_D^{(N)}$ is the elastic (diffractive) nuclear breakup of $^{11}\text{Li} \rightarrow {}^{9}\text{Li} + (2n)$ by the target and $\sigma_S^{(N)}$ is the inelastic (stripping) cross section arising when the (2n) system suffers an inelastic collision with

the target, while ^{9}Li survives intact. σ_C is the electromagnetic dissociation (Coulomb) cross section for $^{11}\text{Li} \rightarrow {}^9\text{Li} + (2n)$.

Nuclear peripheral processes in high-energy collisions involve the calculation of eikonal phases which are dependent on the nuclear densities at the surface and on the nucleon–nucleon scattering amplitudes. For a projectile a incident on a target A, the cross sections for peripherally induced processes are well described by adjusting the tails of the density functions so as to reproduce the correct values of the eikonal phases. This procedure results in an effective optical potential [Ka 75; RC 86] of the form

$$U_{aA} = \langle t_{NN} \rangle \pi^{3/2} \rho_A(0) \rho_a(0) (a_a^3 a_A^3 / a^3) e^{-r^2/a^2} , \tag{2.4}$$

where the nucleon parameters are given by

$$a = \sqrt{a_a^2 + a_A^2} , \qquad a_i^2 = (4R_i t + t^2)/4 \ln 5 ; \qquad R_i = 1.07 A_i^{1/3} \text{ fm} , \quad t = 2.4 \text{ fm} , \tag{2.5}$$

$$\rho_i(0) = [3A_i \exp(R_i^2/a_i^2)/8\pi R_i^3][1 + (\pi^2 t^2/19.36 R_i^2)]^{-1} .$$

The free nucleon–nucleon amplitude $\langle t_{NN}(E) \rangle$ at forward direction ($\theta = 0°$) can be deduced from the experiment. It can be written as

$$\langle t_{NN}(E) \rangle = -\tfrac{1}{2} \hbar v \langle \sigma_{NN} \rangle (\langle \alpha_{NN} \rangle + i) ,$$

where the brackets mean an isospin average of $t_{NN}(E)$ and α_{NN} over the projectile and target nucleons. For 800 MeV A, one may use [Ra 75]

$$\alpha_{pp} = 47.3 \text{ mb} , \qquad \sigma_{pn} = 37.9 \text{ mb} , \qquad \alpha_{pp} = 0.06 , \qquad \alpha_{pn} = -0.2 . \tag{2.6}$$

One observes that at such an energy the nucleon–nucleon scattering amplitude is almost totally imaginary, meaning that the optical potential (2.4) is almost completely absorptive.

The transition matrix element for the elastic (diffractive) breakup in DWBA is

$$T_{fi} = \langle \chi_{k_a}^{(-)}(\boldsymbol{R}) \phi_{xb,f}^{(-)}(\boldsymbol{r}) | [U_{xA}(\boldsymbol{r}_{xA}) + U_{bA}(\boldsymbol{r}_{bA}) - U_{aA}(\boldsymbol{R}_{aA})] | \chi_{k_a}^{(+)}(\boldsymbol{R}) \phi_{xb,i}^{(+)}(\boldsymbol{r}) \rangle , \tag{2.7}$$

where ϕ_{xb} is the wavefunction for the relative motion of x + b clusters (in our case b = dineutron, a = ^{11}Li, and x = ^{9}Li), and $\chi_a^{(+)}$ is the distorted wave for a. In the final state $\chi_a^{(-)}$ represents the distorted wave in the c.m. of x + b. In the way (2.7) is written, the matrix element of U_{aA} is zero because $\langle \phi_{xb,f}^{(-)} | \phi_{xb,i}^{(+)} \rangle = 0$.

We use the c.m. distorted waves

$$\chi_{a,i}^{(+)}(\boldsymbol{R}) = \exp(i\boldsymbol{K}_i \cdot \boldsymbol{R}) \exp\left(-\frac{i}{\hbar v} \int_{-\infty}^{z} U_{aA}(z', b) \, dz' + i\phi_C(b) \right) , \tag{2.8a}$$

$$\chi_{a,f}^{(-)*} = \exp(-i\boldsymbol{K}_f \cdot \boldsymbol{R}) \exp\left(-\frac{i}{\hbar v} \int_{z}^{\infty} U_{aA}(z', b) \, dz' + i\phi_C(b) \right) , \tag{2.8b}$$

where $\phi_C(b) = (Z_a Z_A \alpha)(v/c)^{-1} \ln(kb)$ is the Coulomb phase, and $\alpha = 1/137$.

For the relative-motion wave functions $\phi^{(+)}_{xb,i}$ and $\phi^{(-)}_{xb,f}$ we use simple Yukawa and plane-wave functions as in ref. [BB 88a]. All coordinates are referred to the lab system, with the target origin. The coordinates r_{xA} and r_{bA} are defined by

$$r_{xA} = R - (m_b/m_a)r\,, \qquad r_{bA} = R + (m_x/m_a)r\,.$$

Most of the integrals involved in (2.7) may be calculated analytically and the details of the calculations are shown elsewhere [BH 91a]. The breakup cross section is obtained by standard integrations over the phase space of the fragments. For $R_{^{11}Li}$, $R_{^{9}Li}$ and R_{2n} we use, 5.8, 2.41 and 1.6 fm, respectively. These values are compatible with the cluster wave function of ^{11}Li, adjusted to reproduce the binding energy of the dineutron. The three-body calculations of ref. [JJH 90] have shown that the most probable separation between these neutrons is 3.3 fm.

The "stripping" (inelastic breakup) cross section is given by [HM 85]

$$\sigma_S^N = \frac{\sqrt{\pi}}{\Lambda}\int d^2b_x |S_x(b_x)|^2 \int d^2b_{2n} |\phi_{^{11}Li}(|\boldsymbol{b}_x - \boldsymbol{b}_{2n}|)|^2 [1 - |S_{2n}(b_{2n})|^2]\,, \tag{2.9}$$

where $|S_x(b_x)|^2$ is to be interpreted as the probability that the fragment x (^{9}Li) will survive when hitting the target at an impact parameter b_x. Otherwise, $1 - S_{2n}(b_{2n})^2$ is the probability that the 2n system will suffer an inelastic collision with the target, and $d^3r_{2n}|\phi_{^{11}Li}(|\boldsymbol{b}_x - \boldsymbol{b}_{2n}|)|^2$ is the probability that the 2n system is found at distance $|\boldsymbol{b}_x - \boldsymbol{b}_{2n}|$ from ^{9}Li. The factor in front of (2.9) comes from the assumption that $\phi_{^{11}Li}$ can be described by a gaussian wave function, so that

$$|\phi_{^{11}Li}|^2 = (\Lambda^3/\pi\sqrt{\pi})\exp[-\Lambda^2(z_x - z_{2n})^2]\exp[-\Lambda^2(\boldsymbol{b}_x - \boldsymbol{b}_{2n})^2]\,. \tag{2.10}$$

Equation (2.10) was obtained after an integration over z_x and z_{2n}. The parameter Λ was chosen so that the stripping cross sections obtained by using (2.10) do not differ appreciably from what is obtained by using Yukawa-type wave functions. The proper value of Λ was found to be given by $\Lambda = (11.2\,\text{fm})^{-1}$. This parametrization allows us to write the stripping cross section in the elegant form (See appendix A)

$$\sigma_S^N = \frac{\pi}{\Lambda^2}\sum_{j=0}^{\infty}[1 - T_j^{(2n)}(\Lambda)]T_j^x(\Lambda)\,, \tag{2.11a}$$

$$T_j^{(i)}(\Lambda) = \frac{2(\Lambda^2)^{j+1}}{j!}\int_0^{\infty} b_i^{2j+1}\exp(-\Lambda^2 b_i^2)|S_i(b_i)|^2\,db_i\,, \quad i = x, b\,. \tag{2.11b}$$

Expression (2.11b) is obtained by means of a series expansion of the Bessel function which results from the integration of (2.9) over the azimuthal angle. The factors $|S_i(b_i)|^2$ are given by

$$|S_i(b_i)|^2 = \exp\left(-\frac{2}{\hbar v}\int_{-\infty}^{\infty}|\text{Im}\,U_i(b_i, z_i)|\,dz_i\right), \tag{2.12}$$

where U_i are the optical potentials for 2n + target and ^{9}Li + target, parametrized by eq. (2.4).

In addition to the nuclear fragmentation there is an important contribution from Coulomb dissociation, especially for large Z targets. We can use the formulas obtained by Bertulani and Baur [BB 88a] for the Coulomb dissociation of *cluster nuclei*, which in the limit of very low binding energy, can be written as

$$\sigma_{E1} = \tfrac{4}{3}\pi Z_T^2 \alpha^2 \left(\frac{c}{v}\right)^2 \left(\frac{m_x Z_b - m_b Z_x}{m_a}\right)^2 \frac{1}{\eta^2}\left(\ln\left(\frac{\gamma\hbar v}{\delta\varepsilon R}\right) - \frac{v^2}{2c^2}\right), \tag{2.13a}$$

$$\sigma_{E2} = \tfrac{1}{5}\pi Z_T^2 \alpha^2 \left(\frac{c}{v}\right)^4 \left(\frac{m_x^2}{m_a^2} Z_b + \frac{m_b^2}{m_a^2} Z_x\right)^2 \frac{\varepsilon^2}{\eta^4(\hbar c)^2}\left[\frac{2}{\gamma^2\xi^2} + \left(2 - \frac{v^2}{c^2}\right)^2 \ln(1/\delta\xi) - \frac{v^4}{2c^4}\right], \tag{2.13b}$$

$$\gamma = (1 - v^2/c^2)^{-1/2}, \quad \delta = 0.891\ldots, \quad \varepsilon = \hbar^2\eta^2/(2\mu_{bx}), \quad \xi = \varepsilon b_{min}/\gamma\hbar v .$$

The total Coulomb cross section is given quite accurately by (M1 does not contribute significantly)

$$\sigma_C = \sigma_{E1} + \sigma_{E2} . \tag{2.13c}$$

In the above equations ε is the binding energy of the cluster nucleus. We use $b_{min} = R_{^{11}Li} + R_T$, with $R_T = 1.2A_T^{1/3}$ fm. The total nuclear reaction cross section is given by

$$\sigma_R^N = 2\pi \int_0^\infty b\,db[1 - |S(b)|^2] , \tag{2.14}$$

where $|S(b)|^2$ is given by the eq. (2.12), but with the potential $U_{Li,A}$ constructed in the way of eqs. (2.4)–(2.6). To this reaction cross section one should add the contribution of the Coulomb interaction. The most important channel in this case is the two-neutron emission, which can be obtained within an RPA approach as in ref. [BF 89] and [Te 91], or within the cluster-model approach, as described above.

The cross section of the nuclear elastic breakup $\sigma_D^{(N)}$, stripping $\sigma_S^{(N)}$, electric dipole σ_{E1}^C and electric quadrupole σ_{E2}^C are given in table 2 together with the experimental data for the two-neutron removal of ^{11}Li incident on ^{12}C, ^{63}Cu and ^{208}Pb. The $\sigma_D^{(N)}$ and $\sigma_S^{(N)}$ for $\varepsilon = 0.2$ MeV were multiplied by a factor 1.23 in order that their sum with the Coulomb contribution would result in the experimental value for ^{12}C, which is 220 mb. The cross sections were also calculated for several other binding energies, from 0.17 MeV to 0.33 MeV.

The elastic breakup, and particularly the total Coulomb cross section, decreases appreciably with the binding energy, whereas the stripping cross section, having a geometrical character, does not depend on ε (if one assumes that the ^{11}Li radius is fixed).

In figure 2 we plot the nuclear contribution to the two-neutron removal cross section as compared to the experimental data. Due to the uncertainty of the binding energy of the dineutron, the calculated values lie between the two solid curves. One indeed observes that the calculated cross sections grow faster than the $A^{1/3}$ law, a result that was also obtained by Bertsch et al. [BE 90] with a different method.

Table 2
The elastic (σ_N^{elast}), inelastic (σ_N^{inel}), nuclear ($\sigma_N = \sigma_N^{elast} + \sigma_N^{inel}$), electric dipole ($\sigma_{E1}$), electric quadrupole ($\sigma_{E2}$), Coulomb ($\sigma_C = \sigma_{E1} + \sigma_{E2}$), nuclear experimental (σ_N^{exp}), and Coulomb experimental (σ_C^{exp}) cross sections in mb for the dissociation of ^{11}Li (0.8 GeV/nucleon) projectiles incident on several targets, as a function of the binding energy of the ^{9}Li + dineutron system; $^{11}Li + X \rightarrow {}^9Li +$ anything

ε	σ_{elast}^N	σ_{inel}^N	σ_N	σ_{E1}	σ_{E2}	σ_C	σ_N^{exp}	σ_C^{exp}
$^{11}Li + {}^{12}C$								
0.17	79	136	215	9.1	0.5	9.6		
0.2	76	136	212	7.6	0.4	8.0	220	0
0.25	73	136	209	5.9	0.3	6.2	±10	
0.3	70	136	206	4.8	0.2	5.0		
0.33	69	136	205	4.3	0.2	4.5		
$^{11}Li + {}^{63}Cu$								
0.17	187	223	410	203	8	211		
0.2	180	223	403	169	6	175	320	210
0.25	170	223	393	131	5	136	±20	±40
0.3	162	223	385	105	4	109		
0.33	158	223	381	94	3	97		
$^{11}Li + {}^{208}Pb$								
0.17	339	315	654	1565	43	1608		
0.2	324	315	639	1295	33	3128	420	890
0.25	304	315	619	996	24	1020	±30	±100
0.3	289	315	604	803	17	820		
0.33	281	315	596	717	15	732		

By choosing the binding energy of $\varepsilon = 0.2$ MeV, we find the following parametrization of $\sigma_N = \sigma_D^N + \sigma_S^N$ with A_T:

$$\sigma_N = (aA_T^{1/3} + bA_T^{2/3} + c)\,\text{mb}\,; \qquad a = 98.7\,, \quad b = 2.284\,, \quad c = -25.89\,. \tag{2.15a, b}$$

For large values of A_T, the above equation results in an appreciable deviation from the $A_T^{1/3}$ scaling law.

In contrast to the above results, the nuclear contribution to the total reaction cross section agrees perfectly with the experimental data, as shown in table 3, for five different targets. Data are from Kobayashi et al. [Ko 89]. As expected the nuclear reaction cross section is given by the sum of the geometrical areas of the nuclei. Due to the low binding energy of ^{11}Li it also practically agrees with the definition of [Ko 89] for the "interaction" cross section

$$\sigma_I = \pi(R_A + R_{Li})^2\,; \qquad R_A = (1.355A^{1/3} - 0.365)\,\text{fm}\,, \quad R_{^{11}Li} = (3.14 \pm 0.06)\,\text{fm}\,.$$

Again, we adjust our results so that the data for a berylium target could be reproduced. This amounted to a normalization factor of 1.18. Other studies of the nuclear contribution to the two-neutron removal cross sections of ^{11}Li projectiles have been done by Yabana, Ogawa and Suzuki [YOS 92a, b] and by Riisager et al. [Ri 92].

The electromagnetic dissociation experimental cross sections obtained in ref. [Ko 89] are within the limits of the theoretical pure cluster results, as shown in fig. 3. We observe that the scale

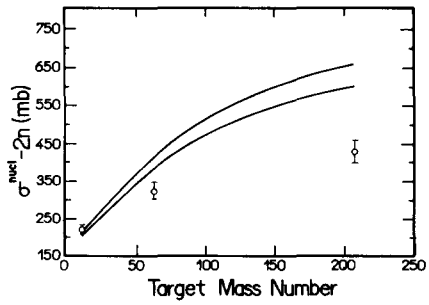

Fig. 2. Two-neutron removal cross sections of ^{11}Li (0.8 GeV/nucleon) projectiles due to the nuclear interaction with the targets, as a function of the target number. Due to the uncertainty of the binding energy of ^{11}Li, the theoretical results lie between the two solid curves. The experimental data of Kobayashi et al. [Ko 89] are also shown.

Table 3
Reactions cross sections (in barn) of ^{11}Li + target

Target	σ_{exp} (b)	σ_{theory}(b)
Be	0.98 ± 0.02	0.98
C	1.04 ± 0.02	1.02
Al	1.41 ± 0.04	1.36
Cu	2.10 ± 0.06	2.00
Pb	3.66 ± 0.08	3.48

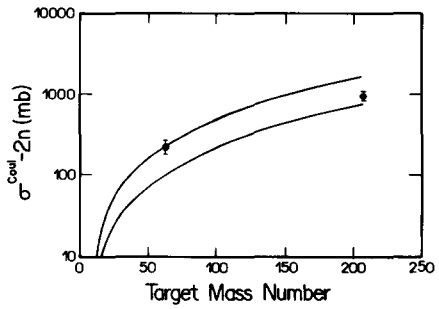

Fig. 3. Same as fig. 2, but for the electromagnetic dissociation of ^{11}Li.

is logarithmic and that the Coulomb cross section is strongly dependent on the binding energy of the dineutron + ^{9}Li. This dependence is approximately proportional to the inverse of ε [see eq. (2.13a)]. The lower solid curve in fig. 3 corresponds to $\varepsilon = 0.33$ MeV, while the upper curve corresponds to $\varepsilon = 0.17$ MeV. If the nuclear contribution to the process actually scales as in eq. (2.15a), the experimental values of the Coulomb contribution (fig. 3) should be smaller. In this case, the cluster model would not reproduce the experimental data on Coulomb dissociation, being larger by 20–30%, especially for high Z targets. However, the RPA results of refs. [BF 89] and [Te 91] would then fall within the "experimental" results.

The merit of the cluster model is that it gives the necessary amount of the electromagnetic dipole strength at low energies, so that the Coulomb dissociation cross section of ^{11}Li turns out to be appreciable. The matrix elements for the photodisintegration of ^{11}Li within the cluster model were first calculated by Bertulani and Baur [BB 88a]. From their results we obtain for the electric dipole strength distribution

$$\frac{dB(E1;\uparrow)}{d(\hbar\omega)} = \frac{3\hbar^2 e^2}{\pi^2 \mu_{bx}} \left(\frac{Z_x m_b - Z_b m_x}{m_a} \right)^2 \frac{\sqrt{\varepsilon(\hbar\omega - \varepsilon)^{3/2}}}{(\hbar\omega)^4}, \tag{2.16}$$

where $\mu_{bx}(\varepsilon)$ is the reduced mass (binding energy) of the cluster system. The dipole strength function for ^{11}Li, assuming $\varepsilon = 0.2$ MeV, has a peak at $\hbar\omega = 0.32$ MeV. In spite of the fact that the cluster model as described here is strongly simplified, the above results indicate that in order to

obtain the correct amount of electric dipole strength of ^{11}Li at low energies, it is necessary either to make unconventional changes in the mean field as done in ref. [BF 89], or include cluster aspects in the shell-model calculations, as was done in refs. [TS 90] and [JJH 90], and in the RPA calculation as was done in ref. [Te 91].

From (2.16) we obtain for the total dipole strength in the cluster model, integrated over energy,

$$B(\mathrm{E1}) = \frac{3\hbar^2 e^2}{16\pi\mu_{\mathrm{bx}}\varepsilon}\left(\frac{Z_{\mathrm{x}}m_{\mathrm{b}} - Z_{\mathrm{b}}m_{\mathrm{x}}}{m_{\mathrm{a}}}\right)^2 . \tag{2.17}$$

For ^{11}Li, using $\varepsilon = 0.2$ MeV, we obtain $B(\mathrm{E1})/e^2 = 2.25\ \mathrm{fm}^2$ in the cluster model, which is about 80% of the cluster sum rule for dipole excitations [Al 82] and 7% of the total nuclear dipole sum rule. This means that in order to reproduce the experimental data on the Coulomb dissociation of ^{11}Li, an appreciable amount of the strength of the dipole response in ^{11}Li should be located at the ^{9}Li + 2n channel. The Coulomb cross section is given by $\sigma_{\mathrm{C}} = \int n(\omega)\sigma_\gamma(\omega)\,\mathrm{d}\omega/\omega$, where $\sigma_\gamma(\omega)$ is the photonuclear cross section and $n(\omega)$ is a smooth function of ω (approximately a logarithm of ω). Therefore, the key information about the nuclear structure is contained in $\int \sigma_\gamma(\omega)\,\mathrm{d}\omega/\omega$ which is directly proportional to the (non-energy weighted) integrated B(E1) values [BB 88b].

2.2. *Hybrid RPA–cluster model for the dipole strength function of ^{11}Li*

It is well known that in nuclei with excess neutrons, low excited dipole states might decouple from the giant dipole state while maintaining their appreciable transition strengths [HK 74; Mo 71; SI 90]. This implies a larger electromagnetic dissociation than in normal stable nuclei.

A possible model that could account for the measurement of large electromagnetic dissociation of ^{11}Li is the excitation of a soft giant dipole resonance (SGR) at very low excitation energies (≈ 0.5 MeV) followed by its decay into ^{9}Li + 2n. Whereas cluster models that mock up the SGR can account for the data, conventional RPA calculation produces very little strength at the required energies, unless a rather unrealistic value of the binding energy of the $p_{1/2}$ orbit (≈ 0.2 MeV) is used [BF 89]. The experimentally known value of the one-neutron separation energy is about 1 MeV and for such a value of ε_{p} too small a cross section is obtained (≈ 0.25 b against the experimental value of 0.9 b). It is worthwhile here to mention that the separation energy of the 2n cluster in ^{11}Li is about 0.2 MeV. Thus the modified RPA calculation of Bertsch and Foxwell [BF 89] with $\varepsilon_{\mathrm{p}} = 0.2$ MeV, mocks up the pairing interaction between the valence neutrons by a rather subtle correction to the mean field [BE 91].

A more natural treatment, within RPA, is to enlarge the p–h configuration space to accommodate the dineutron–dineutron hole excitations. Thus one ends up treating ^{11}Li as composed of three species of particles: protons, neutrons and dineutrons (the dineutron is treated as structureless).

The purpose of this section is to develop the above hybrid RPA–cluster model for ^{11}Li in order to verify the possible enhancement of the low-lying dipole strength.

We choose the Woods–Saxon potential of Bertsch and Foxwell [BF 89] with parameters that result in a $p_{1/2}$ energy of 1.0 MeV. The continuum RPA calculation is done using the complex energy method [Gi 87; To 87; Te 88] except for the inclusion of 2n–2n hole excitations. The dineutron potential is chosen such as to produce the correct dineutron separation energy of $\varepsilon = 0.2$ MeV. This is done easily by taking an usual shell-model Woods–Saxon interaction with an effective nucleon mass of $2M_{\mathrm{N}}$. The single particle configurations included in the calculation are shown in tables 4 and 5 with the corresponding energies.

Table 4
The parameters of the Woods–Saxon potential well used in the calculation of the dipole response $U_{n,p}(r) = V_{n,p} f(r) + l\sigma V_{ls} f'(r)$, $f(r) = \{1 + \exp[(r - R)/a]\}^{-1}$

Protons, neutrons	dineutron
$V_n = -40.99$ MeV	$V_{2n} = -8.61$ MeV
$V_p = -59.82$ MeV	
$V_{ls} = -15.5$ MeV fm	$V_{ls} = 0.0$
$a = 0.65$ fm	$a = 0.65$ fm
$R = 2.78$ fm	$R = 6.2$ fm

Table 5
Calculated single-particle energies in MeV and widths in MeV for neutrons, protons and dineutron, using the code TABOO (A.F.R. de Toledo Piza, University of São Paulo, Internal Report, unpublished)

Orbit	neutron	proton	dineutron
$1s_{1/2}$	−17.74	−30.5	
$1p_{3/2}$	−5.15	−14.55	
$1p_{1/2}$	−0.96	−6.95	
$1d_{5/2}$	1.83 − i0.17	−0.34	
$2s_{1/2}$	6.1 − i6.5	−0.14	−0.20
$2d_{3/2}$	18.8 − i6.0	10.05 − i2.7	
$2p_{1/2}$			2.0 − i2.0

The RPA calculation was then done taking for the residual interaction a Landau–Migdal one (with $g = g' = 0$ and $f_0' = 1.5$), with $R_0 = 3.16$ fm and $C = 447$ MeV fm^3. The B(E1) strength is found distributed over excitation energy as shown in fig. 4. Besides the usual GDR at $E \approx 16$ MeV, not shown in the figure, we find a strongly collective state, the "soft" GDR, at $E = 1.81$ MeV. Since the width of the $2p_{1/2}$ dineutron single particle state is found to be about 4 MeV, we conjecture that our soft GDR has a similar width. The B(E1) value of the soft mode is found to be 2.38 e^2 fm^2 which corresponds to $\approx 85\%$ of the dipole cluster sum rule [A1 82] and 8% of the usual TKR sum rule. Our findings concerning the soft GDR are in complete accord with the results obtained by Sagawa and Honma [SH 90] using the sum rule approach.

The cross sections for Coulomb excitation of electric dipole states in the projectile nucleus (which is by far the dominant excitation mode in highly energetic Coulomb collisions) is given by [BB 88c]

$$\sigma_C = \int n(\omega)\sigma_{E1}(\omega)\,d\omega/\omega\,, \tag{2.18}$$

$$n(\omega) = (2/\pi)Z_T^2\alpha(c/v)^2\,[\xi K_0 K_1 - (v^2\xi^2/2c^2)(K_1^2 - K_0^2)]\,, \tag{2.19}$$

where K_0 (K_1) is the modified Bessel function of zeroth (first) order, as functions of

$$\xi = \omega b_0/\gamma v\,, \quad b_0 = R_T + R_{^{11}Li}\,. \tag{2.20}$$

b_0 is equal to the sum of the target, R_T, and projectile, $R_{^{11}Li}$, radii. We use $R_T = 1.2\,A_T^{1/3}$ fm and $R_{^{11}Li} = 3.2$ fm. The radius of ^{11}Li was obtained from the weighted average $R_{^{11}Li} = \frac{9}{11}R_{^9Li} + \frac{2}{11}R_{2n}$, where $R_{^9Li}$ and R_{2n} are given in table 4. In terms of the electric dipole reduced matrix elements B(E1; ω) of the excited nucleus for the excitation energy $\hbar\omega$, we can write

$$\sigma_{E1}(\omega) = \tfrac{16}{9}\pi^3(\omega/c)\,dB(E1;\omega)/d(\hbar\omega)\,. \tag{2.21}$$

The $dB/d(\hbar\omega)$ values were calculated in the RPA method as described above.

For $\omega \leq 1$, which is the case for the most relevant part ($\hbar\omega < 40$ MeV) of the RPA response function (see fig. 4) one can use

$$\xi K_0 K_1 - (v^2\xi^2/2c^2)(K_1^2 - K_0^2) \approx \tfrac{1}{2}\ln[(0.681/\xi)^2 + 1]\,. \tag{2.22}$$

For states with energy $\hbar\omega = 1$ MeV one finds that the above expression, eq. (2.22), results in the value 2.95 for ^{11}Li + ^{208}Pb collisions. However, for $\hbar\omega = 20$ MeV one obtains the value 0.32. That is, B(E1, ω) values with low energy (≈ 1 MeV) are weighted by a factor 9 times larger in the integral (2.18) than states with large energies (≈ 20 MeV). In conclusion, a small enhancement of the B(E1; ω) values at low energies may increase the cross section (2.18) considerably. Inserting (2.21) and (2.22) in (2.18) we get, with $E \equiv \hbar\omega$,

$$\sigma_C \approx 1.3 \times 10^{-3} Z_T^2 \int \frac{dB}{dE} \frac{1}{e^2} \ln[(210/Eb_0)^2 + 1]\, dE\,(\mathrm{fm}^2)\,, \tag{2.23}$$

which is a good approximation to determine the Coulomb excitation cross sections for ^{11}Li projectiles incident with 800 MeV A on a target (Z_T, A_T). In eq. (2.23) E is given in MeV and b_0 in fm.

For Cu and Pb targets, with the RPA response calculated above, we obtain

$$\sigma_C = 130\,\mathrm{mb} \quad \text{for} \quad {}^{11}\mathrm{Li} + \mathrm{Cu}; \qquad \sigma_C = 682\,\mathrm{mb} \quad \text{for} \quad {}^{11}\mathrm{Li} + \mathrm{Pb}\,. \tag{2.24}$$

These values of σ_C are to be compared to the experimentally extracted values of $\sigma_C = 210 \pm 40$ mb and $\sigma_C = 890 \pm 100$ mb, respectively.

The cross section for ^{11}Li + Pb given above is almost identical to the value obtained by Bertsch and Foxwell [BF 89] using a different model. The contribution to the cross section of the excitations at $E > 10$ MeV is about 65 mb. We also find a strong linear dependence of σ_C on the width of the resonance. Allowing a variation of $\Gamma^{\uparrow}$, we obtain for ^{11}Li + Pb, $\sigma_C = \sigma_C^0(1 + 0.84\Gamma^{\uparrow})$ where σ_C^0 is the cross section with $\Gamma^{\uparrow} = 0$.

It is interesting to mention at this point that a pure cluster model, does generate a large dipole strength at low excitation energies. In fact, the expression for dB/dE one obtains in this case is given by eq. (2.16) which, for the ^{11}Li nucleus, with ε, the separation energy of the dineutron, equal to 0.2 MeV, peaks at $E = \frac{8}{5}\varepsilon = 0.32$ MeV and has a peak value of $4.1\, e^2\,\mathrm{fm}^2$. Notice that the photo–nuclear cross section $\sigma_{E1}(E)$ of eq. (2.21) with the above cluster model $dB(E1)/dE$, peaks at $E = 2\varepsilon = 0.4$ MeV and has a peak value of 1.61 fm^2. The dashed curve in fig. 4 corresponds to eq. (2.16). With the above distribution the cross section σ_C, eq. (2.18), comes out close to our RPA–cluster calculation if $\Gamma^{\uparrow}$ is taken to be 5 MeV.

Finally, it is worthwhile to mention that the experimental data for the electromagnetic dissociation of 800 MeV A ^{11}Li projectiles on Pb are 1.72 ± 0.65 b for the total cross Coulomb section and

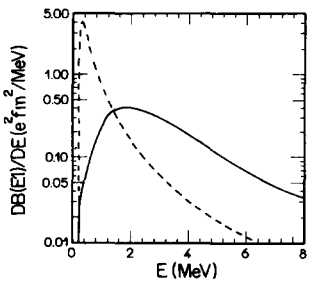

Fig. 4. Calculated dipole strength distribution in the $E < 10$ MeV region. Solid curve corresponds to the RPA–cluster while the dashed one represents the pure-cluster model eq. (2.16). See text for details.

0.89 ± 0.1 b for the 2n-removal channel [Ko 89]. It is by no means clear to which extent the RPA response function includes other decay channels besides the two-neutron emission. This fact actually may present an additional difficulty in relating the Coulomb excitation cross section obtained with the RPA approach and the experimental two-neutron removal cross sections.

In the next section we present a calculation of the Coulomb dissociation cross section as a function of energy for several models of $dB(E1)/dE$ and compare with the available data.

2.3. *Low-energy behavior of ^{11}Li dissociation cross section*

Recently, Sustich [SU 92], has presented a detailed calculation of the Coulomb dissociation cross section for three models of dipole strength distribution as a function of ^{11}Li bombarding energy for reactions on a ^{197}Au target. This type of calculation is quite important as it clearly shows the sensitivity of the low-energy cross section to the model used for the ^{11}Li dipole response. Sustich found that the data point at 30 MeV A measured by Anne et al. [An 90] can be best accounted for by the single particle model of Bertsch and Foxwell [BF 89]. The more recent correlated-state model of Bertsch and Esbensen [BE 91] underestimates the cross section by factor of 2, while the cluster model [BB 88a; BH 90a; BBH 91] overestimates the cross section by a factor of 2. The large-basis nonspurious shell-model calculation by Hayes and Strottman [HS 90] also underestimates the cross sections. Both the single particle and correlated-state model account well for the data at 790 MeV A [Ko 89] whereas the cluster model again overestimates the cross section at this energy by about 15%.

The formula used by Sustich for the Coulomb dissociation cross section, however, is only valid at high energies, as pointed out by Bertulani and Baur [BB 88c]. At lower energies, a more complicated expression for the cross section must be used.

The Coulomb dissociation cross section is given by eq. (2.18) which can be rewritten as

$$\sigma_C = \tfrac{16}{9}\pi^3\alpha \int dE\, n_{E1}(E) \frac{1}{e^2} \frac{dB(E1)}{dE} \tag{2.25}$$

where E is the excitation energy, α is the fine structure constant, and $dB(E1)/dE$ is the dipole response function of the nucleus.

Expressions for $n_{E1}(E)$ appropriate for high-energy collisions can be found in textbooks [Ja 75]. At lower energies, Winther and Alder [WA 79] have shown that such an expression may be used to a good approximation, if a rescaling of the impact parameter of the form

$$b \to b + \tfrac{1}{2}\pi Z_1 Z_2 e^2/m_0 v^2 \gamma \tag{2.26}$$

is done. In fact, as shown by Aleixo and Bertulani [AB 89] such an approximation yields only a 10–20% discrepancy with an exact numerical calculation. It was also shown that the approximation is worse if one goes to lower excitation energies. Since the important part of the dipole response function is located at very low energies for unstable nuclei such as ^{11}Li, it is therefore appropriate to discuss this question more closely.

In this section we are mainly interested in giving a more accurate description of the Coulomb excitation of unstable nuclei, which becomes increasingly important as the binding energy of the excited nucleus decreases. We do not want to promote one or the other nuclear model which enters

eq. (2.25) through the dipole response $dB(E1)/dE$. Indeed, we find it more exciting when discrepancies between the models show up so that one can have deeper physical understanding of the phenomena under scrutiny.

In ref. [BB 88c] it was shown that an analytical expression for $n_{E1}(E)$, which is valid for all bombarding energies, can be obtained (we observe that the original formula for the dipole case appearing in ref. [BB 88c] has a misprinted sign in one of its terms)

$$n_{E1}(E) = (2/\pi)Z_1^2\alpha e^{-\pi\eta}(c/v)^2\Bigg(-\xi K_{i\eta}K'_{i\eta} - \tfrac{1}{2}(c/v)^2\xi^2 \times\left\{K_{i\eta+1}K_{i\eta-1} - K_{i\eta}^2 - \frac{i}{\varepsilon_0}\left[K_{i\eta}\left(\frac{\partial K'_\mu}{\partial\mu}\right)_{i\eta} - K_{i\eta}\left(\frac{\partial K_\mu}{\partial\mu}\right)_{\mu=i\eta}\right]\right\}\Bigg), \tag{2.27}$$

where Z_1 and v are the target charge and the projectile (^{11}Li) velocity, respectively. α is the fine structure constant, ε_0 is the eccentricity factor of the lowest allowed Coulomb trajectory, that is

$$\varepsilon_0 = \begin{cases} 1 & \text{for} \quad 2a > R\,, \\ R/a - 1 & \text{for} \quad 2a < R\,, \end{cases} \tag{2.28}$$

where $R = R_T + R_p$ is the sum of the target- and projectile-matter radii. The quantities η and ξ are defined by $\eta = \omega a/\gamma v$ and $\xi = \varepsilon_0\eta$, where ω is the excitation frequency, $a = Z_1Z_2e^2/2E_{c.m.}$ is half the distance of closest approach for a head-on collision, and $\gamma = (1 - v^2/c^2)^{-1/2}$.

The function $K_{i\eta}$ is the modified Bessel function with imaginary order. $K'_{i\eta}$ means the derivative of $K_{i\eta}$ with respect to the argument. At high energies the above expression for n_{E1} reduces to eq. (2.19) which is the form used by Sustich, even at the rather low energy of 30 MeV A. We should point out, however, that Sustich [Su 92] included recoil corrections to (2.19) which should render his calculation accurate to within 20%.

Before presenting our calculation of σ_C based on eq. (2.27) for the different models of $dB(E1)/dE$, we discuss the behavior of the function $K_{i\eta}$ given by the integral [AS 64] (see appendix B for details)

$$K_{i\eta}(\xi) = \int_0^\infty \exp(-\xi\cosh x)\cos\eta x\,dx\,. \tag{2.29}$$

These functions are not tabulated, and have to be obtained by means of the numerical evaluation of the integral at the r.h.s. of (2.29). The functions $K_{i\eta+1}$ and $K_{i\eta-1}$ are not needed since

$$K_{i\eta+1}(\xi)K_{i\eta-1}(\xi) = (\eta^2/\xi^2)K_{i\eta}^2(\xi) + K'^2_{i\eta}\,. \tag{2.30}$$

In fig. 5 we show the functions $K_i(\xi)$ and $K_{5i}(\xi)$ versus ξ. It is easy to understand the oscillatory behavior of $K_{i\eta}(\xi)$ versus ξ for small values of ξ, by using the stationary phase method. By writing $\cos\eta x = \frac{1}{2}(e^{i\eta x} + e^{-i\eta x})$ and since the integral of eq. (2.29) is even in x, one may take only the $e^{i\eta x}$ branch of the cosine and extend the lower limit of integration to $-\infty$. Changing x to $x + i\pi$ and

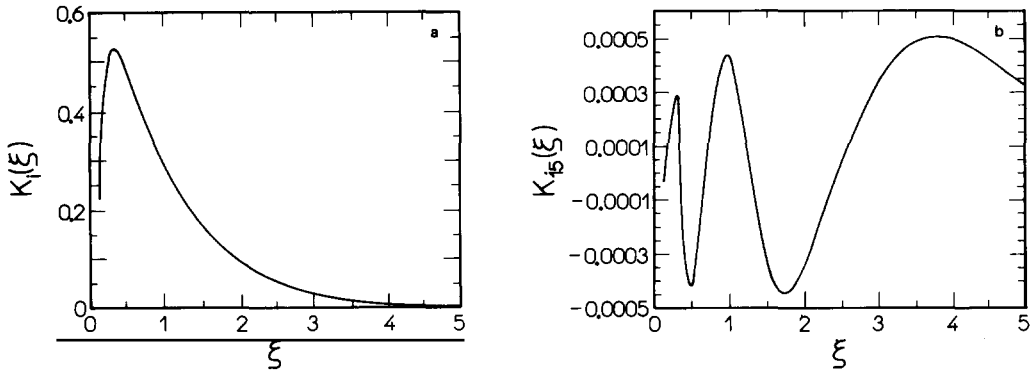

Fig. 5. The function $K_{i\eta}(\xi)$ versus ξ. (a) $\eta = 1$, (b) $\eta = 5$.

using the stationary phase method, we find

$$K_{i\eta}(\xi) \cong \tfrac{1}{2} e^{-\pi\eta/2} [4Y/(\xi^2 - \eta^2)]^{1/4} \operatorname{Ai}(Y) , \tag{2.31a}$$

$$Y = -(\eta \cosh^{-1}(\eta/\xi) - \sqrt{\eta^2 - \xi^2})^{2/3} (\tfrac{3}{2})^{2/3}, \quad \eta > \xi , \tag{2.31b}$$

$$Y = (\xi \sqrt{1 - \eta^2/\xi^2} - \eta \sin^{-1} \sqrt{1 - \eta^2/\xi^2})^{2/3} (\tfrac{3}{2})^{2/3}, \quad \eta < \xi . \tag{2.31c}$$

In eq. (2.31a) $\operatorname{Ai}(Y)$ is the Airy function. This function oscillates for negative values of its argument ($\xi < \eta$) and dies out as $e^{-\xi}$ for large positive values of Y, just as fig. 1b shows. Further, the local period of the oscillations goes as $\Delta\xi \simeq 2\pi\xi/\eta$. Thus, even for small values of η, the function $K_{i\eta}(\xi)$ oscillates at very small values of ξ. In fig. 5a, these oscillations are not shown. A further study of the properties of this function is given in appendix B.

We further verified that the representation (2.31) is also valid for $K_0(\xi)$. Finally, we remark that for our present purposes the argument of the modified Bessel function is related to its order through $\xi = \varepsilon_0 \eta$; and since $\varepsilon_0 \geq 1$, ξ is equal to or larger than η and thus the low-ξ oscillations are not relevant.

Since we want to give a description of the Coulomb excitation process which will be useful for the analysis of Coulomb dissociation of unstable nuclei in general, we observe that for collisions of tens of MeV per nucleon and above, $R \gg a$, that is, $\xi = \varepsilon_0 \eta \gg \eta$. In this case one may use the approximation

$$K_{i\eta}(\xi) \cong K_0(\xi) - \eta^2 [K_1(\xi) - K_0(\xi)] , \tag{2.32}$$

which simplifies eq. (2.31a) enormously since the $K_0(\xi)$ and $K_1(\xi)$ functions are much easier to handle than the $K_{i\eta}(\xi)$ functions.

Further simplifications can be done by noting that

$$\xi = \varepsilon_0 \eta \cong \hbar\omega R/\gamma\hbar v = E_{ex} R/\gamma\hbar v \ll 1 , \tag{2.33}$$

for excitation energies $E_{ex} \ll \gamma\hbar v/R$, which are the important energies involved in the excitation

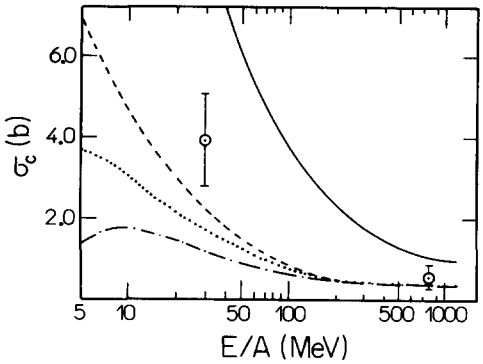

Fig. 6. The Coulomb dissociation cross section for different models of dB/dE. The two data points are from ref. [Ko 89] (E = 790 MeV/nucleon) and ref. [An 90] (E = 30 MeV/nucleon). Full curve: cluster model. Dashed curve: independent-particle model. Dotted curve: correlated-state model. Dashed–dotted curve: hybrid RPA–cluster model. See text for details.

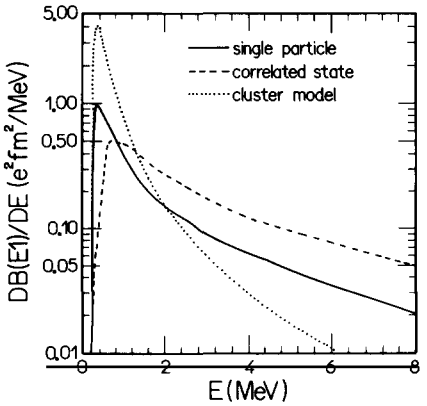

Fig. 7. Dipole response of ^{11}Li in the single-particle (solid), correlated-state (dashed) and cluster (dotted) models.

process of very unstable nuclei. Using the approximation $K_1 \simeq 1/x$ and $K_0 \simeq \ln(\delta/x)$, where $\delta = 1.123\ldots$, one gets

$$n_{E1}(E) \cong (2/\pi)Z_1^2\alpha e^{-\pi\eta}(c/v)^2((1-2\eta^2+\eta^2/\xi)\ln(\delta/\xi) - \xi\eta^2[1/\xi^2+\ln^2(\delta/\xi)] - \tfrac{1}{2}(c/v)^{-2}\xi^2\{1/\xi^2 - \ln^2(\delta/\xi) + \eta^2[(1/\xi^2)\ln^2(\delta/\xi) + 2\ln^2(\delta/\xi) + 2(\xi-1)/\xi]\}) . \quad (2.34)$$

We turn now to the results obtained for σ_C, eq. (2.25), using for the dipole strength distribution $dB(E1)/dE$ different models discussed recently in the literature. In fig. 6 we show a comparison among the cross sections obtained with the modified independent particle model [BF 89], the correlated state model [BE 91], the hybrid RPA–cluster model [Te 91], and the cluster model [BB 88a]. Our results diverge in an important way from those of Sustich [Su 92] in that none of the models account for the low-energy data point (E_{lab} = 30 MeV A). Whereas the cluster model overestimates the cross section, the other models fall short in value. The recent calculation of Lenske and Wambach [LW 90], using the quasiparticle RPA method, also fall short in value (the cross section for this case is not shown in the figure as it almost coincides with the independent-particle result). The dipole response in these models are shown in fig. 7 (see also fig. 4). Bertulani and Sustich [BS 92a] have shown that the Coulomb excitation of higher multipoles (M1, E2, ...) in ^{11}Li is small and can be neglected.

2.4. Nonperturbative character of Coulomb breakup of weakly bound nuclei

As we have seen in the last sections, Coulomb excitation of unstable nuclei is a very useful technique to access information on the structure and excitation response function of such nuclei. This is especially true for the study of neutron- or proton-rich nuclei with very small binding energies.

Many of the exotic nuclei, like ^{11}Li do not have bound states besides the ground state, i.e., any excitation leads to their fragmentation. The Coulomb fragmentation cross section is roughly

inversely proportional to the separation energy of the fragments [BB 88a]. Therefore, it can be very large for weakly bound projectiles incident on large-Z targets.

One should expect that perturbation theory fails in describing the breakup process when the cross sections attain very high values. In fact, we show that the breakup probability calculated with first-order perturbation theory is close to unity. This can be understood with the use of simple arguments. The energy transferred by the Coulomb field to the excitation of a projectile nucleus, with N neutrons and Z protons, incident with velocity v on a target nucleus with charge eZ_T at an impact parameter b is approximately given by (see section 1.2) $E^* = 2(NZ/A)(Z_T e^2)^2/m_N b^2 v^2$, where m_N is the nucleon mass. For ^{11}Li projectiles ($N = 8$, $Z = 3$) incident on lead at $b = 15$ fm and $v \approx c$, one gets $E^* \approx 0.3$ MeV. This energy is more than sufficient to break ^{11}Li apart, since the separation energy of two neutrons from this nucleus is about 0.25 MeV. This means that at small impact parameters the breakup probability is of order of unity and a nonperturbative treatment of the breakup process should be carried out.

Nonperturbative techniques like semiclassical coupled-channels calculations can be used in this case. However, there is an insufficient amount of experimental data with details about the structure of the unstable nuclei, to justify a complicated calculation. Since this is the final information that one wants to obtain, a clearer understanding of the reaction mechanism is more useful at this stage. The cluster model seems to be very appropriate to achieve this goal. It has been used with success for the determination of the main characteristics of reactions induced by ^{11}Li projectiles. Owing to its simplicity the matrix elements of Coulomb breakup can be easily calculated. In this section we describe the semiclassical coupled-channels calculations recently developed in ref. [BC 92].

2.4.1. *Coulomb breakup of loosely bound clusters*

Let us consider a projectile nucleus composed of two clusters with charges eZ_b and eZ_c, and masses m_b and m_c, respectively, incident on a target with charge eZ_T. We assume that the projectile follows a straight-line trajectory with velocity v and impact parameter b. The interaction potential (neglecting magnetic interactions and nuclear forces) responsible for the breakup of the projectile, is given by

$$V = \gamma Z_T e^2 \left(\sum_{k=b,c} \frac{Z_k}{[(y_k - b)^2 + \gamma^2 (z_k - vt)^2]^{1/2}} - \sum_{k=b,c} \frac{Z_k}{(b^2 + \gamma^2 v^2 t^2)^{1/2}} \right), \tag{2.35}$$

where $\gamma = (1 - v^2/c^2)^{-1/2}$, and y_k, z_k represent the transverse and longitudinal coordinates of the particles, respectively.

In the dipole approximation, expression (2.35) becomes*),

$$\begin{aligned} V &= \frac{\gamma Z_T e^2}{(b^2 + \gamma^2 v^2 t^2)^{3/2}} \sum_{k=b,c} Z_k (b y_k + v t z_k) \\ &= \sqrt{\tfrac{2}{3}\pi}\, [\gamma Z_T e^2/(b^2 + \gamma^2 v^2 t^2)^{3/2}] (Z_b m_c/m_a - Z_c m_b/m_a) \\ &\quad \times r \{ ib [Y_{11}(\hat{r}) + Y_{1-1}(\hat{r})] + \sqrt{2}\, v t Y_{10}(\hat{r}) \}, \end{aligned} \tag{2.36}$$

where r is the vector from b to c and $m_a = m_b + m_c$. The first (second) term inside the curly brackets represents the transverse (longitudinal) part of the interaction.

*) It is important to quote here that in fact the magnetic dipole interaction $j \cdot A = (v/c \cdot j) V$ has to be added to (2.35) so that the term proportional to t in (2.36) comes out correctly. This can be achieved by using the continuity equation.

In first-order time-dependent perturbation theory, the probability amplitude for the projectile breakup, i.e., the transition from the ground state $|0\rangle$ to a state $|\boldsymbol{q}\rangle$ in the continuum is given by

$$a^{(1)}_{(\boldsymbol{q})} = \frac{1}{i\hbar}\int_{-\infty}^{t} \exp[-i(E_0 - E_q)t'/\hbar]\,\langle \boldsymbol{q}|V(t')|0\rangle\,dt' \,. \tag{2.37}$$

For loosely bound projectiles the ground state can be represented by a Yukawa wave function $\phi_0(\boldsymbol{r}) = Ne^{-\eta r}/r$, where N is the normalization factor, and $\eta = \sqrt{2\mu_{bc}B}/\hbar$, with μ_{bc} equal to the reduced mass of the (b + c) system and B the binding energy. Neglecting final-state interactions, the states $|\boldsymbol{q}\rangle$ are given by $\phi_{\boldsymbol{q}}(\boldsymbol{r}) \equiv \langle \boldsymbol{r}|\boldsymbol{q}\rangle = e^{i\boldsymbol{q}\cdot\boldsymbol{r}} - e^{iqr}/r(\eta + iq)$, where the wave number q is related to the energy E_q as $E_q = \hbar^2 q^2/2\mu_{bc}$. The second term of $\langle \boldsymbol{r}|\boldsymbol{q}\rangle$ guarantees the orthogonality and completeness of the initial and final states.

The dipole matrix elements are given by [BB 88a]

$$\langle \boldsymbol{q}|rY_{1m}(\hat{\boldsymbol{r}})|0\rangle = i4\sqrt{2\pi\eta}\,[q/(q^2 + \eta^2)^2]\,Y_{1m}(\boldsymbol{q}) \,. \tag{2.38}$$

To first order, the breakup probability is obtained by integrating the square modulus of (2.37) over the density of final states, i.e.,

$$P^{(1)}(b, t) = 2P^{(1)}_{m=1} + P^{(1)}_{m=0} = \int |a^{(1)}_{(\boldsymbol{q})}|^2 \frac{d^3q}{(2\pi)^3} \,, \tag{2.39}$$

summed over the beam-axis components of the angular momentum carried by the Coulomb field, $m = 0, \pm 1$. The integral over q is easily accomplished if one uses the sudden approximation, which is valid for

$$(b/\gamma v)(E_q + B) \ll 1 \,. \tag{2.40}$$

For weakly bound nuclei, as ^{11}Li, $E_q + B \approx 1$ MeV, and at bombarding energies $E_{lab} \sim 1$ GeV, the above reaction shows that the sudden approximation is valid for impact parameters $b < 300$ fm.

Within the sudden approximation we can omit the exponential factor in (2.37) and the integrals can be evaluated analytically as (α is the fine structure constant)

$$P^{(1)}(b, t) = \tfrac{1}{6}[(Z/\eta b)(c/v)]^2\,[Z_b(m_c/m_a) - Z_c(m_b/m_a)]^2$$
$$\times\left[\left(1 + \frac{\gamma vt/b}{\sqrt{1 + (\gamma vt/b)^2}}\right)^2 + \frac{1}{1 + (\gamma vt/b)^2}\right] . \tag{2.41}$$

The first (second) term inside the large square brackets arises from the transverse (longitudinal) part of the interaction potential (2.36). It is clear that only the transverse contribution survives at $t = \infty$. The longitudinal contribution cancels since the component of the electric field along the beam axis is an odd function of time. The breakup probability at $t = \infty$ is given by

$$P^{(1)}(b, \infty) = \tfrac{2}{3}[(Z/\eta b)\,(c/v)]^2\,[Z_b(m_c/m_a) - Z_c(m_b/m_a)]^2 \,. \tag{2.42}$$

For grazing collisions with heavy targets at intermediate energies the breakup probabilities of eq. (2.42) are close to (or even exceed) unity. Therefore, first-order perturbation theory cannot be used. However, if the sudden approximation holds, a nonperturbative closed expression can still be derived. The amplitude can then be written as [neglecting the longitudinal component of the interaction potential (2.36)]

$$a_{(q)}^{(S)} = \langle q | \exp\left(\frac{1}{i\hbar}\int_{-\infty}^{\infty} V(t)\,dt\right)|0\rangle = \langle q | \exp(-i\mathscr{C} r \sin\theta \sin\phi)|0\rangle\,, \tag{2.43}$$

$$\mathscr{C} = (2Z_T \alpha c/bv)[Z_b(m_c/m_a) - Z_c(m_b/m_a)]\,. \tag{2.44}$$

Using the completeness relation

$$\phi_0(r)\phi_0^*(r') + \frac{1}{(2\pi)^3}\int \phi_q^*(r)\cdot\phi_q(r')\,d^3q = \delta(r - r')\,, \tag{2.45}$$

one finds

$$P^{(S)}(b) = \int |a_{(q)}^{(S)}|^2 \frac{d^3q}{(2\pi)^3} = 1 - \frac{\eta^2}{4\pi^2}\left|\int d^3r \frac{e^{-2\eta r}}{r^2}\exp(-i\mathscr{C} r\sin\theta\sin\phi)\right|^2\,. \tag{2.46}$$

The above integral can be easily evaluated and the result is

$$P^{(S)}(b) = 1 - (4\eta^2/\mathscr{C}^2)[\arctan(\mathscr{C}/2\eta)]^2\,. \tag{2.47}$$

When $\mathscr{C}/2\eta \ll 1$ (large impact parameters) the above relation reproduces the first-order result (2.42). On the other hand, if $\mathscr{C}/\eta$ is large, one gets to lowest order in $\eta/\mathscr{C}$,

$$P^{(S)}(b) = 1 - \pi^2\eta^2/\mathscr{C}^2\,.$$

A comparison between the sudden approximation and the first-order breakup probabilities for the reaction ^{11}Li + Pb → ^{9}Li + 2n + Pb at 30 MeV A is shown in fig. 8, as a function of b. The failure of the first-order approximation at small impact parameter is clearly seen.

The results of eqs. (2.41), (2.42) and (2.47) were obtained on the basis of the sudden approximation. In the example considered, the ^{11}Li breakup probability is appreciable even for large relative energies in the projectile frame ($E_q \sim 2$ MeV), where the sudden approximation starts to break down. In addition, the treatment of this section cannot account for the energy distribution of the breakup cross section. A more powerful coupled-channels treatment is therefore desirable. However, one faces the difficulty that the final states are in the continuum (one would have to consider a continuous channel label) and the coupling matrix elements present divergence problems, caused by the nonlocalized behavior of the continuum wave functions. This difficulty is avoided by a discretization of the continuum along the lines proposed by Bär and Soff [BS 85] in their nonperturbative calculations of atomic ionization by heavy ions. We shall use the same treatment of the continuum and develop a set of semiclassical coupled-channels equations.

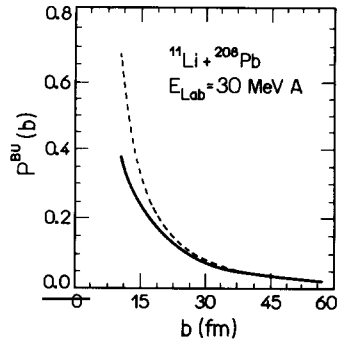

Fig. 8. Coulomb breakup probabilities of ^{11}Li projectiles incident on lead at 30 MeV/nucleon, as a function of the impact parameter b. The solid line corresponds to the nonperturbative sudden approximation. The dashed line corresponds to first-order perturbation theory.

2.4.2. *Discretization of the continuum and semiclassical treatment of the coupled-channels problem*

Our basis of time-dependent discrete states is defined as

$$|\phi_0\rangle = \exp(-iE_0 t/\hbar)|0\rangle\,, \quad E_0 = -B\,; \qquad |\phi_{jlm}\rangle = \exp(-iE_j t/\hbar)\int \Gamma_j(E)|E, lm\rangle\,dE\,, \tag{2.48}$$

where $|E, lm\rangle$ are continuum wave functions of the projectile fragments (without the interaction with the target), with good energy and angular-momentum quantum numbers E, l, m. The functions $\Gamma_j(E)$ are assumed to be strongly peaked around an energy E_j in the continuum. Therefore, the discrete character of the states $|\phi_{jlm}\rangle$ (together with $|\phi_0\rangle$) allows an easy implementation of the coupled-states calculations. We assume that the projectile has no bound excited states. This assumption is often the rule for very loosely bound systems. The orthogonality of the discrete states (2.48) is guaranteed if

$$\int dE\,\Gamma_i(E)\Gamma_j(E) = \delta_{ij}\,. \tag{2.49}$$

For the continuum set $|Elm\rangle$ we use, for the sake of simplicity, the plane wave basis

$$\langle r\,|\,Elm\rangle = u_{l,E}(r)\,Y_{lm}(\hat{r}) = (2\mu/\hbar^2)^{3/4}(E^{1/4}/\sqrt{\pi})\,j_l(qr)\,Y_{lm}(\hat{r})\,, \tag{2.50}$$

which obey the normalization condition ($E = \hbar^2 q^2/2\mu$)

$$\langle Elm\,|\,E'l'm'\rangle = \delta_{ll'}\delta_{mm'}\delta(E - E')\,. \tag{2.51}$$

These states arise from the partial wave expansion of the plane wave $\exp(i\boldsymbol{q}\cdot\boldsymbol{r})$. Writing the time-dependent Schrödinger equation for $\Psi(t) = \sum a_{jlm}\phi_{jlm}$, taking the scalar product with the basis states and using orthonormality relations, we get the equations

$$i\hbar\frac{da_{jlm}}{dt} = \sum_{j'l'm'} V_{jlm;\,j'l'm'}\,a_{j'l'm'}\exp[-i(E_{j'} - E_j)t/\hbar]\,. \tag{2.52}$$

We use the index $j = 0$ for the ground state $|0\rangle$ and $j = 1, 2, \ldots$ for the discretized continuum states. $V_{jlm;\, j'l'm'}$ are the matrix elements $\langle \phi_{jlm}|V|\phi_{j'l'm'}\rangle$.

For $\Gamma_j(E)$ we consider two different sets of functions. Firstly the set $\Gamma_1(E), \ldots, \Gamma_N(E)$;

$$\Gamma_j(E) = 1/\sqrt{\sigma} \quad \text{for} \quad (j-1)\sigma < E < j\sigma\,,$$
$$= 0\,, \qquad \text{otherwise}\,. \tag{2.53}$$

This set corresponds to histograms of constant height $1/\sqrt{\sigma}$ and width σ. The states $\Gamma_j(E)$ trivially satisfy the orthonormalization condition (2.49). They present the advantage of leading to simple analytical expressions for the coupling matrix elements. On the other hand, they have discontinuities at the edges, which lead to numerical difficulties. The second set consists of the functions

$$\chi_j(E) = N_{n_j}(E/\sigma)^{n_j^2}\exp[-n_j(E/\sigma)]\,. \tag{2.54}$$

The normalization constant

$$N_{n_j} = (1/\sqrt{\sigma})[(2n_j)^{2n_j^2+1}/(2n_j^2)!]^{1/2}\,, \tag{2.55}$$

guarantees that $\int \chi_j(E)\chi_j(E)\,\mathrm{d}E = 1$. The functions χ_j are peaked at $E = n_j\sigma$ and have width $\approx \sigma$. The integer $n_j = Kj$ is proportional to the index j and the proportionality constant, a small integer K, is a parameter of the set which determines the overlap of two consecutive functions χ_j and χ_{j+1}. Three consecutive functions χ_4, χ_5 and χ_6 are shown in fig. 9 for $K = 3$ and $\sigma = \frac{40}{3}$ KeV. With this choice χ_5 is peaked at the maximum of the experimental breakup cross section ($E \approx 250$ KeV) of ^{11}Li projectiles (see fig. 12). However, this set fails to satisfy the orthogonality condition (2.49). This shortcoming can be fixed by the definition of a new set $\Gamma_j(E)$ of linear combinations

$$\Gamma_j(E) = \sum_{k=1}^{N} C_{jk}\chi_k(E)\,, \tag{2.56}$$

with the coefficients C_{jk} determined so that the resulting combinations are orthogonal. These coefficients can be found by means of an orthogonalization procedure as, e.g., the Gram–Schmidt method [BF 69]. The result of the application of this method to the functions of fig. 9a is shown in fig. 9b. The set of eqs. (2.56) has the advantages of being continuously derivable and of leading to reasonably simple coupling matrix elements.

A comparison between basis states $\phi_{jlm}(r)$ generated with each of these sets [through eq. (2.48)] is made in figs. 10a, b. We chose for convenience the parameters $\sigma = 40$ KeV, $j = 5$ for the first set (eq. 2.53) and $K = 3, j = 5, \sigma = 13.3$ KeV for the second set (eq. 2.54). With this choice one of the E_j is equal to 200 KeV for both sets. We take $l = 1$, $m = 1$, as example. One observes that the discrete wave functions ϕ_{jlm} decrease fast enough with r, so that the matrix elements $\langle \phi_{jlm}|rY_{1\mu}|\phi_{j'l'm'}\rangle$ are finite. The use of the histograms (2.53) for $\Gamma_j(E)$ leads to beats in ϕ_{jlm}, as displayed in fig. 10a. These beats are the result of the discontinuous nature of $\Gamma_j(E)$ and arise from the interference from the borders of the histograms. Due to this behavior, the numerical evaluation of $\langle \phi_{jlm}|rY_{1\mu}|\phi_{j'l'm'}\rangle$ is more involved than with the second set of Γ_j functions (2.55). Indeed, as we see from fig. 10b the beats disappear with the use of the basis set (2.55). Although the use of a plane-wave basis allows the derivation of simple results with both sets, this fact is of relevance for future improvement of the calculations.

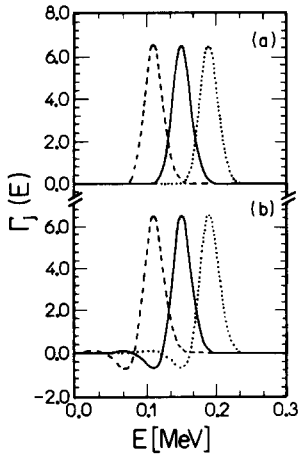

Fig. 9. A set of functions given by the expression (2.54), (a) before and (b) after orthogonalization.

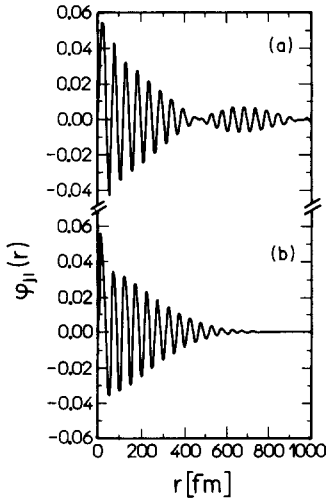

Fig. 10. Radial wave functions for the discretized continuum using (a) the histogram, and (b) the continuous set. We used $E_j = 200$ keV and $l = 1$.

Using (2.48) and the properties of the spherical harmonics one finds

$$V_{ljm;\,j'l'm'} = \frac{(-1)^m}{\sqrt{2}}\gamma Z_T e^2\left(Z_c\frac{m_b}{m_a} - Z_b\frac{m_c}{m_a}\right)\frac{\sqrt{(2l+1)(2l'+1)}}{(b^2+\gamma^2v^2t^2)^{3/2}}\begin{pmatrix} l & 1 & l' \\ 0 & 0 & 0\end{pmatrix}$$

$$\times\left\{ib\left[\begin{pmatrix} l & 1 & l' \\ -m & 1 & m'\end{pmatrix} + \begin{pmatrix} l & 1 & l' \\ -m & -1 & m'\end{pmatrix}\right] + \sqrt{2}\,vt\begin{pmatrix} l & 1 & l' \\ -m & 0 & m'\end{pmatrix}\right\} I_{jl;\,j'l'}\,, \quad (2.57a)$$

$$I_{jl;\,j'l'} = \int r^3\,dr \int dE\,\Gamma_j(E)\int dE'\,\Gamma_{j'}(E')u^*_{l,E}(r)u_{l',E'}(r)\,. \quad (2.57b)$$

From (2.57a) one deduces that the interaction potential is different from zero only if $|l - l'| = 1$, as expected. A discussion of the use of the dipole approximation is presented later in this section.

The use of the plane-wave basis is especially useful because, exploiting the recursion and closure relations of the spherical Bessel functions, one obtains the general result

$$I_{jl;\,j'l'} = (\hbar^2/\mu)[\tfrac{1}{2}(l+l'+2)F_{jj'} + \delta_{l,l'+1}G_{j,j'} + \delta_{l+1,l'}G_{j'j}]\,, \quad (2.58)$$

$$F_{jj'} = \int dq\,\Gamma_j(E)\Gamma_{j'}(E), \qquad G_{jj'} = \int dq\,q\Gamma_j(E)\frac{d}{dq}\Gamma_{j'}(E)\,, \quad (2.59)$$

with $E = \hbar^2q^2/2\mu$. Explicit forms can be found for each basis set.

(a) *Histogram.* Applying this relation to the histogram set (2.53), one can show that for $j, j' \neq 0$

$$I_{jl;\,j'l'} = \hbar\sqrt{\frac{2}{\mu\sigma}}\begin{cases} \tfrac{1}{2}(l+l'+1)(\sqrt{j}-\sqrt{j-1}) & \text{if} \quad j = j'\,, \\ -(-1)^{(j+l-j'-l')/2}\sqrt{\tfrac{1}{2}(j+j'-1)} & \text{if} \quad |j-j'| = 1\,, \\ 0 & \text{otherwise}\,. \end{cases} \quad (2.60)$$

For $j = 0$ or $j' = 0$, only the integral with l or $l' = 1$ is necessary, and the result is

$$I_{00;j1} = I_{j1;00} = (\sqrt{2\eta\sigma}/\pi)[E_j^{3/4}/(E_0 + E_j)^2](\hbar^2/2\mu)^{3/4}\,, \quad E_j = (j - \tfrac{1}{2})\sigma\,. \tag{2.61}$$

(b) *Continuous basis.* For the set of continuous energy functions (2.55) one finds, for $j, j' \neq 0$

$$\begin{Bmatrix} F_{jj'} \\ G_{jj'} \end{Bmatrix} = \sqrt{\frac{\mu\sigma}{2\hbar^2}} \sum_{n,n'} C_{jn} C_{j'n'} N_n N_{n'} \frac{\Gamma(n^2 + n'^2 + \frac{1}{2})}{(n + n')^{n^2 + n'^2 + 1/2}} \begin{Bmatrix} 1 \\ 2n'^2 - n'(2n^2 + 2n'^2 + 1)/(n + n') \end{Bmatrix}, \tag{2.62}$$

where $\Gamma(z)$ is the gamma function and we simplified the notation using $n \equiv n_j$. For $j = 0$ or $j' = 0$, one finds

$$I_{00;j1} = I_{j1;00} = \frac{\sqrt{2\eta\sigma}}{\pi} \frac{E_j^{3/4}}{(E_0 + E_j)^2} \left(\frac{\hbar^2}{2\mu}\right)^{3/4} \sum_n \frac{n^2!}{n^{n^2+1}} \sqrt{\frac{(2n)^{2n^2+1}}{(2n^2)!}}\, C_{jn}\,. \tag{2.63}$$

As we have seen above, the use of the plane-wave basis results in the elegant derivation of $I_{jl;j'l'}$ represented by eqs. (2.58) and (2.59). Nonetheless, the s-wave ($l = 0$) state of eq. (2.50) is not orthogonal to the bound-state wave function. To restore orthogonality one has to add an extra piece to this function. We expect however that this approximation does not affect our results appreciably since to access this state one needs at least two transitions: the $00 \to j1$ followed by $j'1 \to j'0$. But the latter transition competes with the transition to the ground state, $j1 \to 00$, which is the dominant one. A more severe restriction is the use of plane waves to describe the continuum. A realistic calculation would have to use outgoing waves for $u_{l,E}^{(+)}(r)$ which would carry information about the final interactions of the b + c system.

2.4.3. Results and discussions

We now use the theory delineated above to study the breakup of ^{11}Li projectiles incident on heavy targets at energies around 30 MeV/nucleon. In fig. 11 we show the integrals $I_{jl;j'l'}$ for the continuum–continuum coupling ($j, j' \neq 0$). In particular we choose $l = 0$ and $l = 1$. The coupling $j0 \to j' = j, 1$, solid line in fig. 11a, is a reorientation effect in which the transition involves only a change in the angular momentum ($l = 0$ to $l = 1$ in this case) of the state. We show also in fig. 11a $I_{j0;j'1}$ for transitions between states with different energies. In particular we take the transition between neighboring states, with $j' = j + 1$ (dashed line). We use the results obtained with the continuous energy set, eqs. (2.62) and (2.63). One observes that while for $j' = j$ the integral decreases with energy, for $j' = j + 1$ it increases steadily. These results reproduce the trend shown by eq. (2.60). In fig. 11b it is shown how $I_{j0;j'1}$ varies as a function of $E_{j'}$, for a fixed $E_j = 0.2$ MeV. One observes that it is maximum for neighboring energy states and has an oscillatory behavior. This has the consequence that the $j, j' \neq j$ coupling will practically not contribute to the total breakup probability, $P_{(E)}^{\mathrm{BU}}$, since its contribution will be washed out.

The breakup probability per unit energy interval, $P_{(E)}^{\mathrm{BU}}$, is given by

$$P_{(E)}^{\mathrm{BU}} = \sum_{ij} \Gamma_i(E)\Gamma_j(E)Q_{ij}\,, \quad Q_{ij} = \mathrm{Re}\left(\sum_{lm} a_{ilm}^* a_{jlm}\right). \tag{2.64a, b}$$

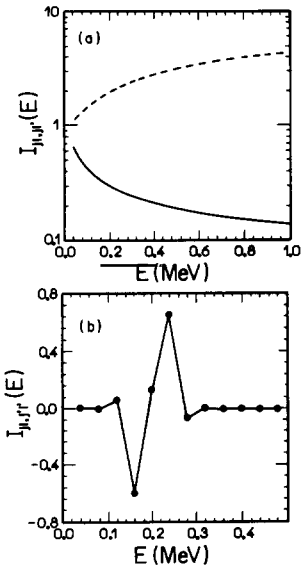

Fig. 11. (a) Radial matrix elements, eq. (2.57b) for the transition $j \to j+1$ (dashed line), and for the $j \to j$ one (solid line). We used $l = 0$ and $l' = 1$. (b) Radial matrix elements for the transition $j \to j'$, keeping $E_j = 200$ keV and varying $E_{j'}$.

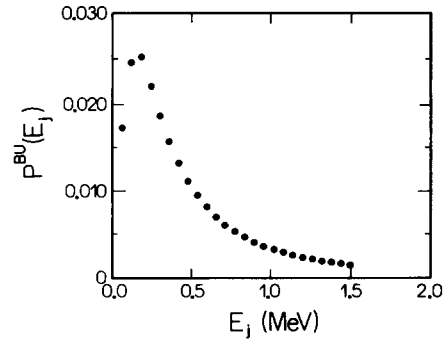

Fig. 12. Coulomb breakup probability, per unit energy interval (MeV^{-1}), of ^{11}Li projectiles incident on lead at 30 MeV/nucleon and $b = 15$ fm, as a function of the final total kinetic energy of the fragments.

In fig. 12 we show the breakup probability per unit energy interval for the reaction ^{11}Li + Pb at 30 MeV A and $b = 15$ fm, calculated from eq. (2.64a) by solving the coupled differential equations (2.52) for a_{ilm}. We see that the energy distribution of the fragments is peaked at $E \sim 0.25$ MeV. Therefore, the most relevant momentum transfer to the ^{11}Li nucleus occurs at $q = \sqrt{2\mu_{bc}B}/\hbar \sim 20\,\mathrm{fm}^{-1}$. The validity of the dipole approximation for the interaction potential (2.57) to calculate the continuum–continuum coupling can only be justified for $qr \ll 1$. But, as shown in fig. 10, the discretized wave functions extend up to 400 fm. Thus, unless the matrix elements for the continuum–continuum coupling, eq. (2.57b), have its main contribution from $r \ll 20$ fm, the dipole approximation is not valid. The $j' = j$ coupling does satisfy this requirement. In this case the wave functions have equal energies, but different angular momenta. This causes an asymptotically ($r \gg 1/q$) constant phase difference between the wave functions entering in $I_{jl;\,jl'}$. This leads to cancellations in the integrand of eq. (2.57) for large r. The situation is different for $j' \neq j$. In this case the integrand has contributions from larger values of r and these contributions increase with energy. With a correct treatment of the multipole expansion of the interaction potential (2.35) the integrals $I_{jl,\,j'\neq j,\,l'}$ would decrease with E. We expect that the transitions $00 \to j', l = 1$ and $j', l = 1 \to 00$ dominate the excitation process, so that the matrix elements between states with $j \neq j' \neq 0$ do not play an important role. Also, to minimize the consequence of the break down of the dipole approximation in the continuum–continuum coupling for $j \neq j'$, we use in our calculation a large parameter K (we take $K = 4$). This leads to small $I_{j\neq j'}$.

In fig. 13 the solid line represents P^{BU}, the total breakup probability [eq. (2.64a) integrated over energy], as a function of the dimensionless parameter $\tau = vt/b$, for $b = 15$ fm. This is obtained by solving the coupled channels eqs. (2.52) for a time t and calculating the sum $P^{BU}(t) = \sum_{j\neq 0} |a_{jlm}(t)|$. The dashed line corresponds to the first-order perturbation calculation in the sudden limit (eq. 2.41). The breakup probability occurs in a time scale of $\Delta t \sim b/v$. This comparison indicates a reduction in the breakup probability, arising from high-order processes.

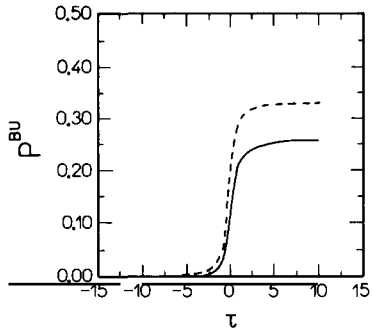

Fig. 13. Coulomb breakup probabilities of ^{11}Li projectiles incident on lead at 30 MeV per nucleon, as a function of $\tau = vt/b$.

The total cross section is given by

$$\sigma^{BU} = 2\pi \int_{b_{min}}^{\infty} b\,db\,P^{BU}(\infty)\,. \tag{2.65}$$

The value of b_{min} is chosen according to Winther and Alder [WA 79], as (see section 2.4)

$$b_{min} = R_P + R_T + \pi Z_P Z_T e^2/4E_{lab}\,, \tag{2.66}$$

where R_P (R_T) is the projectile (target) radius. For ^{11}Li we use $R_P = 3.14$ fm, while for the target we use $R_T = 1.2\,A^{1/3}$. The above formula includes a recoil correction on the Coulomb excitation cross section, given by the last term which depends on the bombarding energy, E_{lab}. Our results are shown in table 6. In the first column we give the cross sections of our nonperturbative approach and in the second the prediction of first-order perturbation. The experimental values for the electromagnetic dissociation cross section of ^{11}Li projectiles incident on Pb at several bombarding energies are shown in the third column [Bl 91; Ko 89]. It is not clear from the experimental data of Blank et al. [Bl 91] which fraction of these cross sections goes into the ^{9}Li + 2n channel, but due to its binding energy the breakup probability into this channel is dominant and a direct comparison with our results is possible. We see that, while for high bombarding energies the results of the two theoretical approaches are practically the same, at low energies they differ by about 20%. This is due to the large breakup probabilities which occur for reactions around some tens of MeV per nucleon [HPB 91]. The coupled-channels calculation result gives a better value of the cross section at this energy.

Table 6
Comparison among the cross sections for the Coulomb breakup of ^{11}Li incident on lead, obtained within the first-order perturbation, $\sigma^{(1)}$, and with the coupled-channels calculation, σ. The last column gives the experimental values of refs. [Bl 91; Ko 89]

E_{lab} (MeV A)	$\sigma^{(1)}$ (b)	σ (b)	σ_{exp} (b)
790	1.01	0.94	0.89 ± 0.1
86.2	3.5	2.8	1.37 ± 1.43
69.9	3.8	3.1	2.96 ± 0.83

The inclusion of higher-order effects in the Coulomb breakup treatment of ^{11}Li projectiles has also been recently studied by Baur, Bertulani and Kalassa [BBK 92] and by Shyam, Banerjee and Baur [SBB 92], Bertsch and Bertulani [GB 92], and by Canto, Donangelo and Schultz [CDS 92].

3. Elastic scattering

3.1. Optical-model analysis

Recent work [Br 88; BS 88; KB 88; St 89] has established that the elastic scattering of light heavy-ion systems such as ^{12}C + ^{12}C, ^{16}O + ^{12}C and ^{16}O + ^{16}O shows sufficient transparency for the cross sections to be dominated by far side scattering [HM 84; MS 84]. In particular, there is often the appearance of a prominent (but damped) rainbow [St 89; HM 84; MS 84]. It has been speculated that exotic nuclei like ^{11}Li would exhibit much stronger absorption because of the weak binding of the excess neutrons so that there would no longer be far side dominance. Then the scattering would be more characteristic of the scattering by a black sphere for which the near side and far side amplitudes are equal at all angles and their interference produces marked diffractive oscillators [HM 84; MS 84]. However, we shall show here that there are good reasons to believe that this is not so, and that the scattering is still dominated by refraction.

3.1.1. Construction of the optical potential

Here we describe the construction of the complex optical potential, $U = V + iW$. The real potential was obtained from the folding model, using the DDM3Y effective nucleon–nucleon interaction described elsewhere [Br 88; BS 88; KB 88], together with realistic representations of the nuclear density distributions [Sa 79]. For ^{11}Li we took the spherical Hartree–Fock densities of Bertsch et al. [BBS 89] which were shown to account for the interaction cross sections measured at $E/A = 790$ MeV, while a shell-model density [Sa 79] was used for ^{12}C. The DDM3Y interaction is both energy- and density-dependent, and has successfully described [Br 88; BS 88; KB 88] the scattering of stable light heavy-ion systems over a range of energies $E/A \approx 10$ to 120 MeV.

The resulting folded potentials $V_F(r)$ for ^{11}Li + ^{12}C and ^{12}C + ^{12}C at $E/A = 85$ MeV [SMH 91] are compared in fig. 14. As expected, the ^{11}Li potential is more diffuse than the ^{12}C one because of the greater radial extent of the ^{11}Li density; the ^{11}Li potential has a r.m.s. radius of 4.38 fm compared to 3.99 fm for ^{12}C. Also shown in fig. 14 is the result of omitting the contributions of the two valence neutrons from the ^{11}Li density distribution. These two neutrons only give rise to about 10% of the folded potential at small radii, but are responsible for almost all of it at large distances (50% at $r = 7.5$ fm, where the potential is -1 MeV, and 90% at $r = 10$ fm, for example). The potentials for $E/A = 30$ MeV are similar in shape but stronger by 50 to 60%. Their other characteristics are very similar to those shown in fig. 14.

The folding model was "calibrated" by using the ^{12}C + ^{12}C potentials to fit scattering data for this system at the corresponding energies. It was found to be adequate (see fig. 15a) to use the folded shape for both real and imaginary parts of the potential at $E/A = 85$ MeV, with a complex renormalization factor so that we have $U(r) = (N_R + iN_I)V_F(r)$. However, this assumption was not satisfactory at the lower energy of $E/A = 30$ MeV, as indicated by the dot–dash curve in fig. 15b. A much better fit to the data at this energy (solid curve) was obtained by using an imaginary potential $W(r)$ of Woods–Saxon shape. In both cases, the normalization N_R required for the real potential was close to unity.

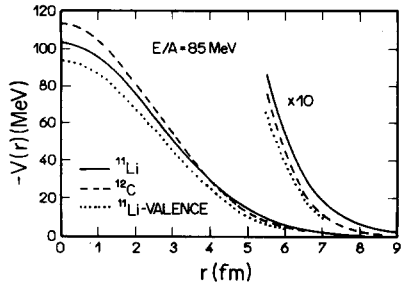

Fig. 14. Comparison of the unrenormalized ($N = 1.0$) folded potentials for ^{11}Li + ^{12}C and ^{12}C + ^{12}C, using the DDM3Y effective nucleon–nucleon interaction for $E/A = 85$ MeV. Also is the potential obtained when the two "valence" neutrons are omitted from the ^{11}Li density distribution.

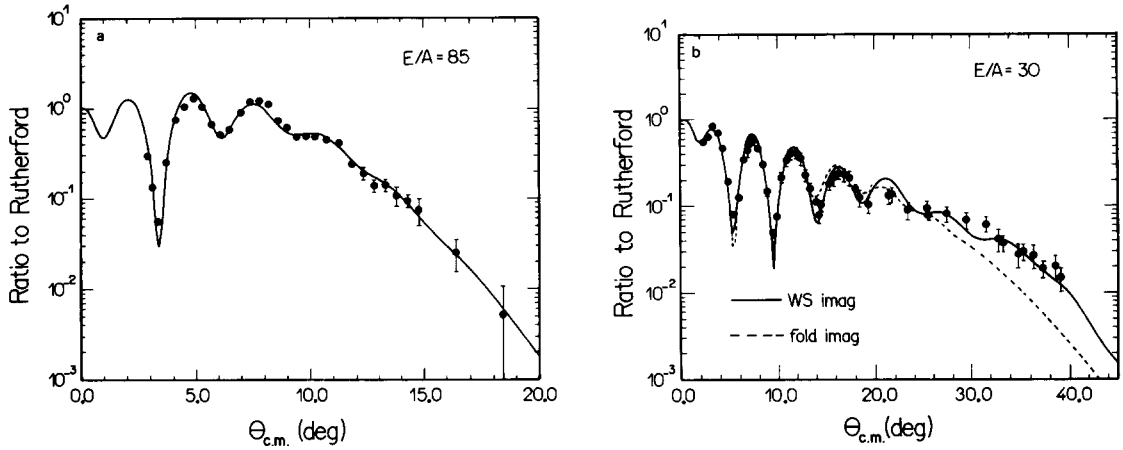

Fig. 15. Fits to the measured [Bu 84] elastic cross sections for ^{12}C + ^{12}C. (a) At $E/A = 85$ MeV, using the folded potential of fig. 14 times $N = 1.175 + 0.725$i. The corresponding reaction cross section is $\sigma_A = 1000$ mb. (b) At $E/A = 30$ MeV. The potential used for the full curve had the folded potential times $N = 0.814$ for the real part and a Woods–Saxon imaginary part ($W_0 = 18.2$ MeV, $r_W = 1.158$ fm, $a_W = 0.584$ fm). The dashed curve is the best fit obtained using the folded shape for both real and imaginary parts, with $N = 0.842 + 0.573$i. The corresponding reaction cross sections are 1236 and 1214 mb, respectively.

The loose structure of ^{11}Li allows it to be fragmented more easily than ^{12}C and this could result in some modification of the ^{11}Li + ^{12}C real potential compared to that for ^{12}C + ^{12}C. The analogous breakup of ^{6,7}Li and ^{9}Be has been found [SY 83; HO 89; Sa 89; Ya 89] to contribute a repulsive term to their real potentials and to increase the strength of the absorptive potentials. The possible effects of this for ^{11}Li are explored here at $E/A = 30$ MeV. However, the explicit calculation [Sa 89; Ya 89] for ^{6}Li has shown breakup to be much less important at higher energies of $E/A \gtrsim 100$ MeV. We assumed this to be true also for the real potential for ^{11}Li, although we did consider the effects of an additional weak absorptive potential of very long range. The possibility of such a term arises because, although the separation energy of a single neutron from ^{11}Li is about 1 MeV, the pair of valence neutrons has a separation energy of only 0.2 MeV. This implies a pairing energy of 0.8 MeV and suggests a cluster model of ^{11}Li as a dineutron very weakly bound to a ^{9}Li core [HJ 87]. Such a picture is consistent with the observation [Ko 88, 89] of a relatively sharp peak in the perpendicular momentum distribution of ^{9}Li fragments from ^{11}Li breakup (see section 7). The absorption from the elastic channel due to this fragmentation could be represented in the optical potential by an imaginary term of exponential form with a range determined

essentially [CDH 91a] by the 2n separation energy of 0.2 MeV; that is, at larger r we may use the phenomenological form

$$\Delta W(r) = -W_p \exp(-r/\alpha), \quad \alpha \approx 7.98 \text{ fm}. \tag{3.1}$$

We can place some constraint on variations of the optical potential away from the simple folding model described above by requiring that the predicted reaction cross section σ_A remain "reasonable". Although measurements of $\sigma_A(E)$ for the exotic projectiles are not yet available at the energies considered here, some guidance can be obtained from other measurements.

3.1.2. Reaction cross-section systematics

First, we note that the cross sections referred to here, measured [Ta 88; Ta 85a; Ta 85b; Ko 88; Ko 89] at $E/A \sim 1$ GeV, are so-called interaction cross sections; that is, part of the reaction cross section σ_A in which the neutron and/or proton number of the projectile is changed. Hence inelastic excitations are omitted and therefore the true reaction cross section is underestimated, which should be compared to an optical-model prediction. (The deficiency has been estimated [Ja 78] to be about 5%.) This does not seem to be a problem at the lower energies, where the measured cross section can be identified with $\sigma_A(E)$.

The measured [Ko 87] and calculated [PD 81; Ma 88] reaction cross sections are found to vary very slowly with energy above $E/A \sim 100$ MeV, so that the values measured [Ta 88] at $E/A \sim 1$ GeV provide some guide as to their values at $E/A = 85$ MeV. For example, the interaction cross section for ^{11}Li + ^{12}C at $E/A = 790$ MeV was measured to be 1047 ± 40 mb. Since ^{11}Li has no bound excited states, and hence no inelastic scattering, we may identify this with the reaction cross section. The measured [Ja 78] value for ^{12}C + ^{12}C at $E/A = 870$ MeV was 939 ± 40 mb; the value of σ_A may be [Ja 78] about 5% larger. Thus the measured ratio for ^{11}Li to ^{12}C is 1.12 ± 0.04, and the ratio of the reaction cross sections is probably even closer to unity. Projectile fragmentation, which is facilitated by the weak binding of ^{11}Li, contributes [Ko 88, 89] about 40% of its reaction cross section at $E/A = 790$ MeV. The production of ^{9}Li is responsible for about one-half of this [Ko 88, 89]. It is possible that fragmentation may be somewhat more important at $E/A = 85$ MeV, thus enhancing the reaction cross section for ^{11}Li relative to that for ^{12}C.

The σ_A for ^{12}C + ^{12}C at $E/A = 83$ MeV has been measured [Ko 87] to be 965 ± 30 mb, which is almost unchanged from its value at the much higher energy. If this were also true for ^{11}Li + ^{12}C, we would predict $\sigma_A \approx 1030$ to 1080 mb for this system at $E/A = 85$ MeV. Even if the ^{11}Li fragmentation cross section were doubled at the lower energy, we would only anticipate $\sigma_A \approx 1500$ mb.

There is more uncertainty at the lower energies where the breakup of loosely bound projectiles becomes more important [SY 83; HO 89; Sa 89; Ya 89]. The average cross sections for a variety of neutron-rich projectiles, over ranges of energies up to 60 MeV per nucleon, and on a target of ^{28}Si, have shown [Mi 87] a roughly linear dependence upon their neutron excess, $N - Z$. (This has been associated [Sh 89] with the diffuseness of the neutron density distribution which increases with neutron excess.) The observed behavior can be represented approximately [Mi 87; Sh 89] by the relation (for a given $A = N + Z$),

$$\sigma_A(N \neq Z)/\sigma_A(N = Z) \approx 1.0 + \alpha(N - Z), \quad \alpha \approx 0.060 \pm 0.005. \tag{3.2}$$

The measured [Ko 87] cross section for $^{12}C + ^{12}C$ at $E/A = 30$ MeV is $\sigma_A = 1316 \pm 40$ mb. Optical-model analyses [Br 88; BS 88; KB 88] of the elastic differential cross sections at the same energy imply a value about 70 mb smaller. If the relation (3.2) is assumed to hold also for ^{12}C as target, it predicts the σ_A for $^{11}Li + ^{12}C$ to be about 30% larger, or about 1710 mb. However, at $E/A = 790$ MeV, the measured σ_A for ^{11}Li on ^{12}C is about 200 mb larger [Ta 85a, b] than a simple extrapolation of the values for the lighter Li isotopes would indicate; this increase has been attributed [BBS 89] to the last two neutrons in ^{11}Li occupying the more weakly bound $0p_{1/2}$ orbit. If this increment persists, or is even larger, at the lower energy, we could anticipate a reaction cross section of as much as 2 b for $^{11}Li + ^{12}C$ at $E/A = 30$ MeV.

3.1.3. Optical-model predictions

Figure 15a shows a fit to the scattering data [Bu 84] for $^{12}C + ^{12}C$ at 85 MeV/nucleon, using the corresponding folded potential multiplied by $N = 1.175 + 0.725i$. The calculated reaction cross section is 1000 mb, compared to the value 965 ± 30 mb measured [Ko 87] at $E/A = 83$ MeV. The same complex renormalization factor N was then applied to the folded potential for $^{11}Li + ^{12}C$. The calculated scattering for the two systems, in ratio to the corresponding Rutherford cross sections, is compared in fig. 16. The predicted $\sigma_A = 1197$ mb for ^{11}Li is 20% larger than for ^{12}C as the projectile.

The most noticeable feature of the comparison of the $\sigma/\sigma_R(\theta)$ ratios for ^{11}Li and ^{12}C in fig. 16 (solid and dotted curves, respectively) is the considerably enhanced ratio for ^{11}Li. However, this is somewhat misleading because the Rutherford cross section for $^{12}C + ^{12}C$ is four times larger than those for $^{11}Li + ^{12}C$ simply because of the greater charge on ^{12}C. Consequently, the cross sections themselves for the two systems are similar in magnitude over most of the angular range shown. In both cases, we see far side dominance [HM 84; MS 84] beyond about 5°.

The scattering of ^{11}Li at the larger angles may be damped by increasing the imaginary strength N_I; for example, doubling it ($N_I = 1.45$) gives $\sigma_A = 1474$ mb, which as concluded above might be close to a reasonable upper limit for the expected value at this energy. The far side scattering amplitude is reduced more by the increase in absorption than is the near side one, consequently the two become closer in magnitude and the far side/near side interference structure seen in the angular distribution (dash–dotted curve in fig. 16) is enhanced.

Simply increasing N_I increases σ_A while preserving the shape of the imaginary potential. However, it may seem more reasonable that ^{11}Li scattering is characterized by an imaginary potential of longer range than for ^{12}C. One such possibility is to add a surface-peaked, long-ranged

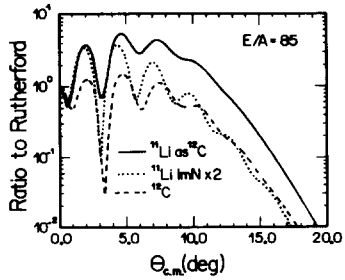

Fig. 16. Elastic cross sections predicted for $^{11}Li + ^{12}C$ at $E/A = 85$ MeV, using the folded potentials in fig. 14 times $N = 1.175 + 0.725i$ (solid curve) and $N = 1.175 + 1.45i$ (dashed curve), shown in ratio to the Rutherford cross sections for this system. The corresponding reaction cross sections are 1197 and1474 mb, respectively. Also shown for comparison (dotted curve) is the best fit to the $^{12}C + ^{12}C$ data from fig. 15a. (Note that the Rutherford cross sections for $^{12}C + ^{12}C$ are approximately four times larger than those for $^{11}Li + ^{12}C$.)

absorptive term, which easily increases the reaction cross section. For example, the use of a Woods–Saxon-derivative imaginary term with a peak magnitude of 1 MeV, radius 6 fm and diffuseness 1.5 fm increases σ_A by 32% to 1576 mb. However, the effect on the elastic angular distribution is much less marked, being more like a uniform reduction by about 30% for $\theta > 5°$, with almost no change in shape.

The extreme in long-ranged absorption is provided by the model of eq. (3.1). We found, for example, that adding such a term with a strength of $W_p = 400$ KeV to the folded potential with $N = 1.1175 + 0.725i$ increased σ_A from the "bare" value of 1197 mb to 1859 mb. This implies over 600 mb of $^{11}Li \rightarrow {}^{9}Li + n^2$ breakup from this cluster configuration, which seems excessive. Nonetheless, the effect on the elastic angular distribution is negligible! The reason for the apparent paradox is that this term predominantly produces absorption from very high partial waves, and thus very large impact parameters, which contribute to small scattering angles. A few percent reduction in the ratio to Rutherford is difficult to observe at these angles, but can correspond to a large absorption because the Rutherford cross section is very large there.

We conclude that the elastic differential cross section for $^{11}Li + {}^{12}C$ at $E/A = 85$ MeV probably lies between the two curves shown in fig. 16, and exhibits refractive features as strong as $^{12}C + {}^{12}C$ scattering at the same energy.

Figure 15b shows fits to $^{12}C + {}^{12}C$ data [Bu 84] at this energy. The best fit obtained by assuming the imaginary potential to have the same folded shape as the real one (dashed curve) requires a renormalization by $N = 0.842 + 0.573i$ and is not satisfactory. A superior fit (solid curve) is obtained with $N_R = 0.814$ and Woods–Saxon imaginary potential with $W_0 = 18.2$ MeV, $r_W = 1.1158$ fm and $a_W = 0.584$ fm. This imaginary potential is less diffuse than the folded one.

The corresponding real and imaginary potentials were constructed for $^{11}Li + {}^{12}C$ and their radial shapes are compared in fig. 17. The scatterings predicted for ^{11}Li and ^{12}C are compared in fig. 18. The scattering obtained for ^{11}Li when the same folded shape for the real and imaginary parts (with $N = 0.842 + 0.573i$) is used is also shown in fig. 18, and results in greater absorption ($\sigma_A = 1469$ mb) than when a Woods–Saxon imaginary shape with the same parameters as $^{12}C + {}^{12}C$ is used ($\sigma_A = 1230$ mb). Again, the ratio to Rutherford for ^{11}Li is ~ 4 times greater than for ^{12}C at small angles because of its smaller charge. It is even larger for $25° > \theta > 10°$ when the Woods–Saxon imaginary part is used, indicating enhanced far side dominance [HM 84; MS 84] compared to the $^{12}C + {}^{12}C$ case. Also, an interesting dip appears in the angular distribution near 30° in this case (solid curve in fig. 18). A near side/far side decomposition [HM 84; MS 84] shows that this is an Airy minimum in the far side scattering. It can be made much more prominent by increasing W_0 from 18.2 to 24 MeV. However, the minimum is removed by the very much stronger absorption at small radii that occurs with the use of the folded shape for the imaginary potential. (The latter reaches a strength of $-97i$ MeV at $r = 0$ when $N_I = 0.573$, compared to the $-18.2i$ MeV for the Woods–Saxon one.)

It was argued in section 3.1.2 above that the reaction cross section for $^{11}Li + {}^{12}C$ at this energy might be as large as 2 b. Increasing the imaginary Woods–Saxon strength W_0 is not an efficient way of increasing σ_A; doubling W_0 to 36 MeV only increases σ_A by about 15%, to 1411 mb, but has a larger effect on the angular distribution. The ratio $d\sigma/d\sigma_R(\theta)$ is reduced considerably for $\theta > 10°$ and oscillations are introduced. However, it seems more plausible, because of the more diffuse density distribution of ^{11}Li, that the Woods–Saxon diffuseness, rather than its strength, should be increased from that appropriate for ^{12}C. Using $a_W = 1.0$ fm raises σ_A by 40% to 1714 mb; it also has an interesting effect on the angular distribution (see fig. 19). The cross sections are reduced considerably between 6° and 22° but then the residual Airy minimum seen previously near 30° is removed and replaced by a smooth fall-off.

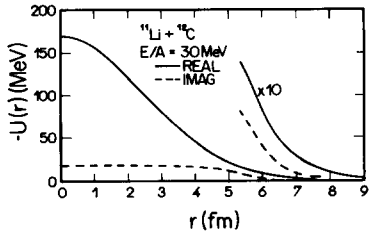

Fig. 17. The unrenormalized ($N_R = 1.0$) folded potential for ^{11}Li + ^{12}C at $E/A = 30$ MeV. Also shown is the Woods–Saxon imaginary potential for ^{11}Li + ^{12}C using the parameter values obtained from fitting ^{12}C + ^{12}C data (fig. 15b).

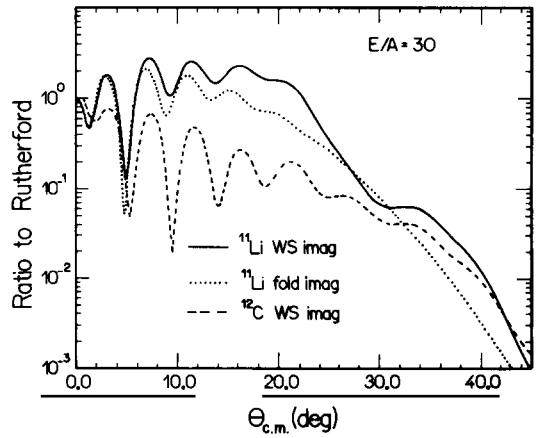

Fig. 18. Elastic cross sections predicted for ^{11}Li + ^{12}C at $E/A = 30$ MeV, using the folded potential in fig. 17 times $N = 0.814$, plus the imaginary potential shown there (solid curve), shown in ratio to the Rutherford cross sections for this system. Also shown (dashed curve) is the result of using the folded shape for both real and imaginary parts, with renormalization $N = 0.842 + 0.573$i. The corresponding reaction cross sections are 1230 and 1469 mb, respectively. The best fit (dotted curve) to the ^{12}C + ^{12}C data is also given for comparison. (Note that the Rutherford cross sections for ^{12}C + ^{12}C are approximately four times larger than for ^{11}Li + ^{12}C.)

The *ad hoc* introduction of a very diffuse surface absorption term (chosen to have the shape of the derivative of a Woods–Saxon potential) can easily increase σ_A. For example, one with a peak strength of $W_D = 2$ MeV centered at $R_D = 6$ fm ($r_D = 1.33$ fm) and with $a_D = 1.5$ fm gives $\sigma_A = 2193$ mb. However, the effect on the elastic angular distribution (fig. 19) is not dramatic, consisting essentially of a reduction in magnitude of $d\sigma/d\sigma_R(\theta)$ by about a factor of 3 for $\theta > 5°$. (We note that it still has a more "refractive" appearance than that for ^{12}C + ^{12}C and a residue of the Airy minimum near 30° remains.)

The extreme of a long-ranged absorptive term is represented by the cluster breakup form of eq. (3.1). The increment in σ_A that this produces is closely proportional to the strength W_p. The choice $W_p = 285$ keV gives $\sigma_A = 2$ b, but just as at $E/A = 85$ MeV, it has no noticeable effect on the elastic angular distribution.

It is possible that fragmentation of ^{11}Li makes the real optical potential significantly less attractive at this lower energy [Sa 89; Ya 89]. We explored the kind of effects this might have by reducing the strength of the folded real potential by 30% (using a renormalization factor $N_R = 0.57$ instead of the $N_R = 0.814$ obtained from the fit to the ^{12}C + ^{12}C data). Two examples are shown in fig. 20, both using the Woods–Saxon imaginary potential, one with the same imaginary parameters as for ^{12}C + ^{12}C and the other with a_W increased to 1.0 fm. The reaction cross sections are almost unchanged from the values obtained using the full $N_R = 0.814$, but there are large effects on the angular distributions. Simply reducing the real potential by 30% introduces a deep minimum near 22° as well as more interference structure at other angles. A near side/far side decomposition [HM 84; MS 84] for this case shows that the sharp dip near 22° is again an Airy minimum in the far side scattering. Indeed, by slowly reducing N_R, one can see that it is the same one that is seen near 30° with the full $N_R = 0.814$, but the angle at which it occurs has moved forward as the real

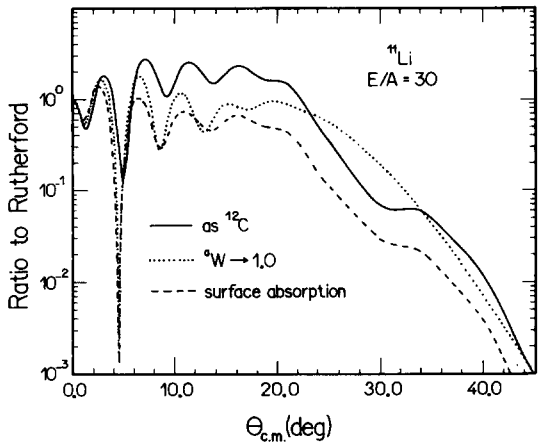

Fig. 19. The effect of increasing the absorption on ^{11}Li + ^{12}C scattering at E/A = 30 MeV. The solid curve is the same as in fig. 18, while the dashed curve has the imaginary diffuseness increased to a_W = 1.0 fm. The dotted curve shows the effect of adding a surface absorption term; a Woods–Saxon derivative with W_D = 2 MeV, R_D = 6 fm and a_D = 1.5 fm was used.

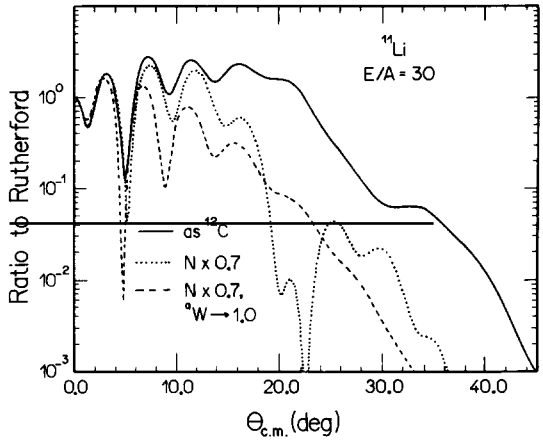

Fig. 20. The effect of reducing the strength of the real potential by 30% on ^{11}Li + ^{12}C scattering at E/A = 30 MeV. The solid curve is the same as in fig. 18 (N = 0.814) while the dashed curve shows the effect of reducing N to 0.57 without changing the imaginary potential. The dotted curve was obtained by also increasing the imaginary diffuseness to a_W = 1.0 fm.

potential strength is reduced. By chance, the choice of $N_R = 0.57$, in conjunction with this imaginary potential, is close to maximizing the destructive interference between the inner and outer contributions that give rise to the Airy structure of the rainbow [HM 84; MS 84]. It would be very interesting to see whether the actual scattering of ^{11}Li + ^{12}C in this energy region reveals any structures like these.

The angular distribution resulting from both reducing N_R by 30% and increasing the imaginary diffuseness to a_W = 1.0 fm has a more conventional appearance (fig. 20) and no sign remains of the Airy minimum. However, comparison with the dot–dashed curve in fig. 19 shows that use of the smaller N_R value has had a larger effect here also. Clearly the scattering at this energy is very sensitive to the real potential.

In summary, we see that we can make predictions for ^{11}Li + ^{12}C scattering at this energy with much less confidence, although our calculations help to delineate the kind of features to look for when measurements are made. In particular, it is important to have some measure of the behavior of the cross sections at larger angles ($>15°$, say), where they begin to fall into the shadow region, and where we have seen the possibility of some distinctive rainbow features occurring.

3.1.4. Contributions from the valence or "halo" neutrons

One is tempted to think of the excess neutrons, especially the two valence ones that occupy the $0p_{1/2}$ orbital in the Hartree–Fock description [BBS 89], as forming a "halo" around a more compact core nucleus. While it is true that the neutron distribution extends to much larger radii than the proton, (see, e.g., ref. [TS 90]), so that the r.m.s. radii are 3.08 and 2.21 fm, respectively, it is not obvious how to identify the "halo" component unambiguously. An operational definition might be provided by the momentum measurements [Ko 88, 89] on ^{9}Li fragments which imply two groups of neutrons in ^{11}Li. It is natural to identify the group with a narrow momentum distribution, and hence associated with the larger radial extent, with the most weakly bound valence neutrons. We made this assumption and recalculated the folded potential by omitting these

two neutrons from the ^{11}Li density distribution. Using only the (real and imaginary) potential generated by the remaining nine nucleons, with the same $N = 1.175 + 0.7225i$, has little effect on the ^{11}Li + ^{12}C scattering at $E/A = 85$ MeV, except for reducing the reaction cross section by 16% and "stretching" the angular distribution out in angle slightly. The latter effect reflects the smaller radius (r.m.s. radius = 4.01 fm) of the folded potential obtained when only the nine core nucleons are included, as compared to when the full density is used (r.m.s. radius = 4.315 fm).

As we have seen (for example, fig. 20), the scattering at $E/A = 30$ MeV is more sensitive to changes in the real potential. Omitting the valence neutron contributions to the folded potential produces a similar stretching of the Fraunhofer oscillations in the angular distribution as observed at the higher energy, but the reduced attraction also results in generally smaller cross sections at the larger angles (fig. 21). Also, the reduced attraction has the effect of moving the Airy minimum forward from 30° to about 26°.

The calculations shown in fig. 21 were made using the Woods–Saxon imaginary potential obtained from the fit to ^{12}C + ^{12}C scattering, but similar effects of omitting the valence contribution to the real potential are seen whatever the choice of imaginary potential. On the other hand, the magnitudes of the reaction cross sections are changed by two percent or less.

It appears that it is not possible to obtain any clear signature of an extended neutron halo by the study of the elastic differential cross sections. The effects of the two valence neutrons are small at the higher energy, while their contribution to the real potential produces changes at the lower energy that are comparable to other uncertainties in our predictions.

Our predictions for the scattering of ^{11}Li + ^{12}C are somewhat uncertain, but they should help to delineate the kind of features to be sought when measurements are made. The primary positive result is that no support was found for speculations that the breakup of light, neutron-rich nuclei would make their elastic scattering take on the diffractive characteristics of strong-absorption scattering. It was important, in reaching this conclusion, to place reasonable constraints upon the allowed size of the reaction cross section.

The interpretation of this finding is that the additional refraction in the surface region accompanying the larger extent of the excess neutrons more than compensates for the extra absorption that is allowed. Thus the elastic scattering tends to remain far side dominated [HM 84; MS 84].

The scattering at $E/A = 30$ MeV can be very sensitive to the real potential strength and its relation to the imaginary one. Under some circumstances (e.g., fig. 20), we found a dramatic Airy

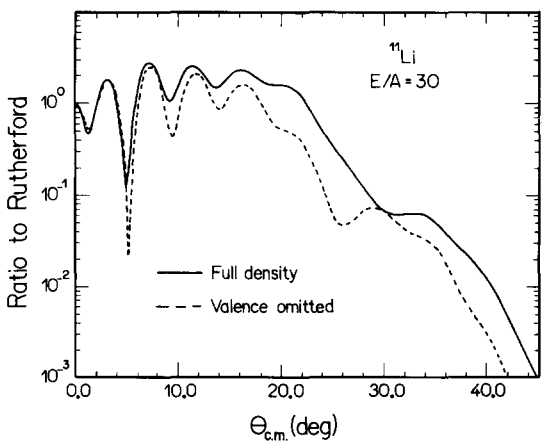

Fig. 21. The effect on the scattering ^{11}Li + ^{12}C at $E/A = 30$ MeV of omitting the two valence neutrons of ^{11}Li when constructing the real folded potential.

minimum appearing in the angular distribution. This would provide a good probe of the optical potential present in the actual scattering of these ions.

The possibility of a very long-ranged absorptive tail due to the fragmentation of a ^{9}Li + 2n cluster configuration was found to be very effective in increasing the predicted reaction cross section. In fact, as discussed in detail in section 3.3, the inclusion of the dynamic polarization potential in the calculation, results in an elastic scattering angular distribution which is damped by a factor of 40% compared with the bare calculation.

3.2. Multiple-scattering theory approach

It is by now clear that neutron- or proton-rich nuclei are intrinsically qualitatively different many-body systems from normal stable nuclei. Both the mean-field aspects as well as the nature of the correlations among the nucleons are apparently quite different in the two systems. Nonelastic reactions, e.g., fragmentation and single neutron emission have been reported and show clear indication of the existence of a halo. Further tests of the halo hypothesis are certainly needed to settle the question.

The simplest process, elastic scattering, however, has not been measured. This stems basically from the low current of the secondary beam namely, e.g., ^{11}Li. Recently, it has been reported that elastic angular distribution of ^{11}Li from hydrogen is being accomplished at much lower energies (100 MeV/nucleon) [Ta 92]. It is therefore of interest to do a preliminary qualitative calculation to assess the importance of the halo in the elastic angular distribution. In the previous sections this question has been posed in the context of heavy ions, with the major conclusion being that systems such as ^{11}Li + ^{12}C behave in much the same way as, e.g., ^{12}C + ^{12}C [SMH 91]. Stronger refractive effects were found for ^{11}Li + ^{12}C. The purpose of the present section is to extend the study to the much simpler systems p + ^{11}Li and α + ^{11}Li. Would the halo also bring in more refraction or does long-range absorption rather dictate the scenario? This is the question we address here.

Our study is based on the Glauber theory with the optical potential determined from the usual multiple-scattering series with medium effects taken fully into account.

3.2.1. Elastic scattering amplitude in eikonal approximation

We present in this section the pertinent formulae used in our calculation of the elastic scattering angular distribution. We ignore spin–orbit effects and thus write for the elastic scattering amplitude, $f(\theta)$,

$$f(\theta) = -ik \int_{-\infty}^{\infty} db\, bJ_0(qb)(e^{i\chi(b)} - 1)\,, \quad k^2 = 2\mu E_{c.m.}/\hbar^2\,, \tag{3.3}$$

where μ is the reduced mass, J_0 is the ordinary Bessel function of order zero, b is the impact parameter and q is the momentum transfer, $q = 2k\sin(\theta/2)$. The phase $\chi(b)$ contains a nuclear and a Coulomb piece and is given by

$$\chi(b) = \chi_N(b) + \chi_C(b)\,; \quad \chi_N(b) = -\frac{1}{\hbar v}\int_{-\infty}^{\infty} dz\, V_N[(b^2 + z^2)]$$

$$\chi_C(b) = (2Z_1Z_2e^2/\hbar v)\,[\ln(kb) + \tfrac{1}{2}\,E_1(b^2/r^2_{m.s.})]\,, \tag{3.4}$$

where $E_1(x)$ is the exponential integral, defined as

$$E_1(x) = \int_x^\infty \frac{e^{-t}}{t} dt \,. \tag{3.5}$$

The Coulomb phase [Fa 70] $\chi_C(b)$ is finite for $b = 0$, yielding

$$\chi_C = (2Z_1 Z_2 e^2/\hbar v)\,[\ln(kr_{m.s.}) - C]\,, \tag{3.6}$$

where $C = 0.577\ldots$ is the Euler constant. The constant $r_{m.s.}$ appearing in the above equations is equal to the root mean square radius of ^{11}Li, $r_{m.s.} = 3.14$ fm. V_N is the complex nuclear potential and v is the relative velocity. In section 3.2.3 we shall give a detailed discussion of the α–^{11}Li optical potential needed for the calculation of $\chi_N(b)$. In what follows we proceed with our discussion of the general features of the eikonal amplitude (3.3).

Because of the logarithmic divergence of $\chi_C(b)$ with increasing b, it is convenient to write $f(\theta)$ as

$$f(\theta) = -ik \int_0^\infty db\, bJ_0(qb)\{\exp[i\chi_C(b)] - \exp[i\chi(b)]\} + f_C(\theta) = f_N(\theta) + f_C(\theta)\,, \tag{3.7}$$

where $f_C(\theta)$ is given by the usual expression

$$f_C(\theta) = -(\eta/2k \sin^2 \tfrac{1}{2}\theta)\exp\{i[2\sigma_0 - \eta \ln(\sin^2 \tfrac{1}{2}\theta)]\}\,, \tag{3.8}$$

where $\sigma_0 = \arg\Gamma(1 + i\eta)$ and $\eta = Z_1 Z_2 e^2/\hbar v$. We use eq. (3.7) in our numerical calculation.

It has been proven useful [HM 84] to decompose $f(\theta)$ into its near and far side components. This is accomplished by first writing the Bessel function in terms of $H_0^{1(2)}(qb)$, the Hankel function of order zero and first (second) type. Asymptotically, these functions behave as running waves. With that the amplitude $f(\theta)$ can be written as $f(\theta) = f_{near}(\theta) + f_{far}(\theta)$, where $f_{near}(\theta)\,[f_{far}(\theta)]$ is given by (3.3) with $J_0(qb)$ replaced by $\frac{1}{2} H_0^{(2)}(qb)\,[\frac{1}{2} H_0^{(1)}(qb)]$.

In the limit when $\chi_C(qb)$ is negligible and $\chi_N(qb)$ is pure imaginary (no refraction) it is easy to see that the following relation holds [HM 84; CIH 85]:

$$f_{near}(\theta) = -f^*_{far}(\theta)\,. \tag{3.9}$$

The above results in an angular distribution that exhibits simple black-disk Fraunhofer diffraction patterns since the near and far amplitudes are equal in magnitude. In our case of $\alpha + {}^{11}$Li one expects strong refractive effects arising both from the Coulomb and nuclear interactions. In particular, the elastic scattering of α particles from several targets has clearly established the phenomenon of nuclear rainbow; a situation characterized by the dominance of the far side component over the near side. At very small angles one always encounters the opposite situation, namely, $f_{near}/f_{far} \gg 1$, owing to the influence, on the angular region, of Coulomb repulsion which affects mostly f_{near}.

To better understand the above features, it is useful to rely on the stationary phase method, more commonly applied to the partial wave expansion of $f(\theta)$. Here we summarize the major findings of ref. [HM 84] involving the stationary phase evaluation of the eikonal amplitude, eq. (3.3).

Whenever the phase $\chi(b)$ is large, which is expected to be the case in our system, the stationary-phase method becomes applicable. We obtain for the near and far contributions

$$f_{\text{near}}(\theta) \approx -\tfrac{1}{2}\,\mathrm{i}kb_{\text{N}}\,[2\pi\mathrm{i}/|\chi''(b_{\text{N}})|]^{1/2}\exp[\mathrm{i}\chi(b_{\text{N}})]\,H_0^{(2)}[q(b_{\text{N}})b_{\text{N}}]\,, \tag{3.10}$$

$$f_{\text{far}}(\theta) \approx -\tfrac{1}{2}\,\mathrm{i}kb_{\text{F}}[2\pi\mathrm{i}/|\chi''(b_{\text{F}})|]^{1/2}\exp[\mathrm{i}\chi(b_{\text{F}})]\,H_0^{(1)}[q(b_{\text{F}})b_{\text{F}}]\,, \tag{3.11}$$

where $b_{\text{N(F)}}$ are determined from the stationary phase conditions

$$\pm\, q = (\mathrm{d}/\mathrm{d}b)\chi(b)|_{b_{\text{N(F)}}}\,, \tag{3.12}$$

which, when eq. (3.4) is used, gives

$$\pm\, q = -\frac{1}{\hbar v}\int_{-\infty}^{\infty}\mathrm{d}z\,\frac{b}{(b^2+z^2)^{1/2}}\,\frac{\mathrm{d}V_{\text{N}}[(b^2+z^2)^{1/2}]}{\mathrm{d}(b^2+z^2)^{1/2}} + \frac{2Z_1Z_2e^2}{\hbar v}\,\frac{1}{b}\,, \tag{3.13}$$

where we have neglected the term inside the square brackets of eq. (3.4) for $\chi_{\text{C}}(b)$.

Notice that the Coulomb term represents the high-energy limit of the usual formula $2\tan(\eta/kb)$. The easiest way to appreciate the above equation is to consider, in the application of the stationary phase method, only the real part of the nuclear phase $\chi_{\text{N}}(b)$, and accordingly, the integrand in eq. (3.13) is real and positive at the energies considered here. This allows real solutions of the above equations to correspond to scattering in the illuminated region. Complex solutions would then be associated with the classically forbidden region.

A simple analytical evaluation of eq. (3.13) is normally not possible when a Woods–Saxon potential is used for V_{N}. Approximate formulae, however, can be obtained in the acceptable limit of small diffuseness (compared to the radius). We obtain

$$\pm\, q = (k/E)\sqrt{2b}\,[(V_0/\sqrt{a_{\text{r}}})g'(x)]\,,\quad x = (b-R)/a_{\text{r}}\,, \tag{3.14}$$

where V_0 is the strength (positive) of the assumed Woods–Saxon real potential, a_{r} is its diffuseness and $g(x)$ is a function evaluated in ref. [HM 84] and is given by

$$g(x) = \bar{v} - (\mu/2v)\,\{1-\exp[-2\bar{v}^2/(\mu+1)]\} + (\mathrm{e}^{\mu/2}/\bar{v}\sqrt{2\mu})\,\mathrm{erfc}\,[\sqrt{\mu/2}]\sqrt{\pi/2}\,, \tag{3.15}$$

$$\mu = \exp\{[(b-R)/a_{\text{r}}]\bar{v}^2\}\,, \tag{3.16}$$

where $\bar{v}$ is the solution of the equation

$$\bar{v} = \tfrac{1}{2}\coth\,[\tfrac{1}{2}(x+\bar{v}^2)]\,. \tag{3.17}$$

For $-x \gg 1$, $\bar{v} \approx \sqrt{-x}$ and one obtains, for small b,

$$g(x) = \sqrt{-x} - \frac{1-\mathrm{e}^{x}}{2\sqrt{-x}} + \frac{\mathrm{e}^{-x/2(1-x)}}{\sqrt{2(1-x)}}\sqrt{\frac{\pi}{2}}\,\mathrm{erfc}\,[-x/2(1-x)]^{1/2}\,. \tag{3.18}$$

On the other hand, for large b, $x > 0$ and one finds here $\bar{v} \approx 1/\sqrt{2}$ and

$$g(x) \approx \sqrt{2/e}\, e^{-x} . \tag{3.19}$$

Therefore, a simple formula which can be used to obtain b_N is

$$q = -(k/E)(2b_N\sqrt{2/e})^{1/2}(V_0/\sqrt{a_r}) \exp[-(b_N - R)/a_r] + 2\eta/b_N . \tag{3.20}$$

The above equation clearly gives two solutions for b_N. One corresponds to predominantly Coulomb, and the other to nuclear scattering. The limiting value of q above, with no real solution for b_N, represents the rainbow momentum transfer and is obtained from the condition $dq/db_N = 0$ or

$$q_r = [-a_r/b_N^r + 1]\, 2\eta/b_N^r . \tag{3.21}$$

At $E_{lab} \approx 100$ MeV for α scattering, one has a small η and a value of b_N^r which is equal to or larger than $R_{^{11}Li}$ in $p + {}^{11}Li$ or the sum of the radii $R_\alpha + R_{^{11}Li}$ in $\alpha + {}^{11}Li$. This shows that q_r is rather small. In fact, our detailed numerical calculation to be presented below demonstrates that q_r is close to zero. This indicates that the $q > q_r$ scattering region is predominantly far sided and dominated by the nuclear attraction at smaller values of b. Further, one anticipates to see greater sensitivity to the details of the nuclear potential in $f(\theta)$ and accordingly corrections to the double or single folding potentials arising from higher-order effects (correlations) can be tested. We turn to a detailed discussion of V_N for $\alpha + {}^{11}Li$.

3.2.2. Elastic scattering of $p + {}^{11}Li$, $p + {}^{9}Li$ and $p + {}^{12}C$

In this section, we apply the formalism developed in the previous section to the elastic scattering, of $p + {}^{11}Li$ and compare it to that of $p + {}^{9}Li$ and $p + {}^{12}C$. We choose the laboratory energy to be 100 MeV. Our aim here is to assess the qualitative effect of the neutron halo in ^{11}Li on the angular distribution. To further understand the phenomenon, we also make the comparison at $E_{lab} = 800$ MeV.

In fig. 22 we show the calculated proton and neutron densities for ^{9}Li, ^{11}Li and ^{12}C. These results were taken from the Hartree–Fock calculation of Bertsch et al. [BBS 89]. To exhibit clearly the spatial extent of the two valence neutrons (in the $1P_{3/2}$ level) in ^{11}Li we show in fig. 23 the difference $\delta\rho_n \equiv \rho_n^{^{11}Li} - \rho_n^{^{9}Li}$. It is clear that the two valence neutrons contribute to the density in the region 2 fm $< r <$ 5 fm. Notice that at $r < 2$ fm the contribution is negative. Further, the matter radius of ^{9}Li is about 2.5 fm. We next construct the $p + A$ optical potential. This we do using the $t\rho$ approximation with medium corrections. At $E_{lab} = 100$ MeV, the average, medium modified nucleon–nucleon optical potential is given by [HRB 91]

$$U_N(r) = \langle t_{pn}\rangle \rho_n(r) + \langle t_{pp}\rangle \rho_p(r) , \tag{3.22}$$

$$t_{pN} = -(E/k)\bar{\sigma}_{pN}(\xi_{pN} + i) , \qquad N = p \text{ or } n , \quad \xi_{pp} = 1.87 , \quad \xi_{pn} = 1.00 . \tag{3.23}$$

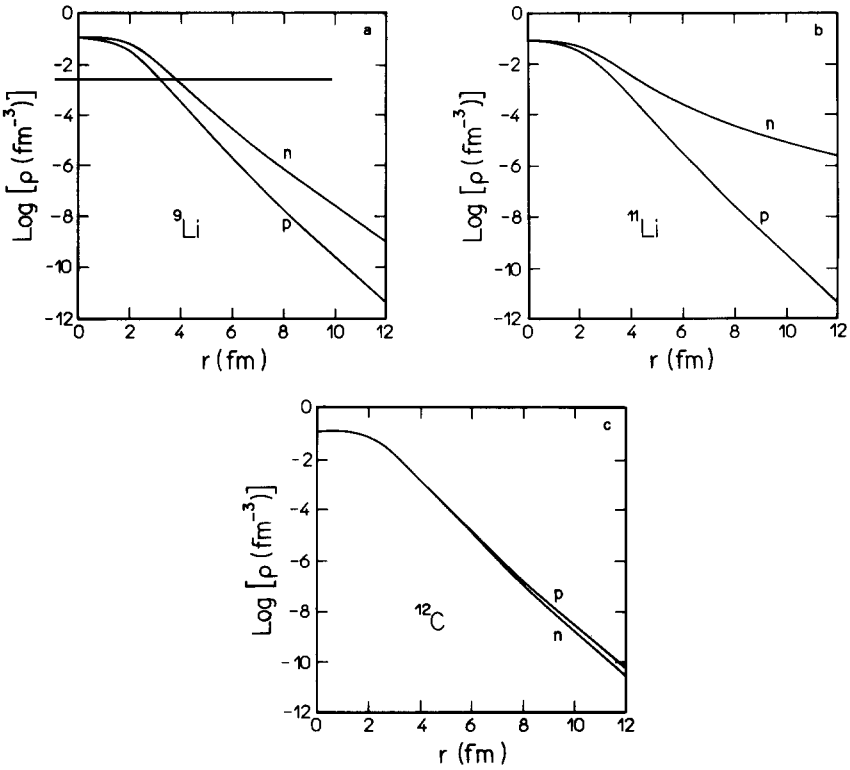

Fig. 22. The Hartree-Fock densities of neutrons and protons for (a) ^{9}Li, (b) ^{11}Li and (c) ^{12}C (ref. [BBS 89]).

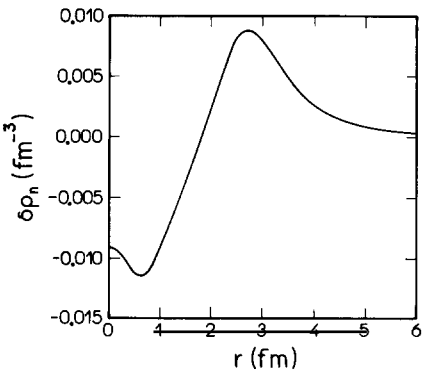

Fig. 23. The difference $\rho_n^{^{11}\mathrm{Li}} - \rho_n^{^{9}\mathrm{Li}}$ versus r.

The Pauli-corrected nucleon–nucleon total cross section is given by [HRB 91]

$$\bar{\sigma}_{\mathrm{pN}} = \sigma_{\mathrm{pN}}(E) P(E_{\mathrm{F}}/E) , \tag{3.24}$$

$$P(x) = \begin{cases} 1 - \frac{7}{5}x , & x \le \frac{1}{2} , \\ 1 - \frac{7}{5}x + \frac{2}{5}x(2 - 1/x)^{5/2} , & x \ge \frac{1}{2} , \end{cases} \tag{3.25}$$

$$E_{\mathrm{F}}^{(\mathrm{N})} = (\hbar^2/2m_{\mathrm{N}})(k_{\mathrm{F}}^{(\mathrm{N})})^2 , \qquad k_{\mathrm{F}}^{(\mathrm{N})} = [3\hbar^2 \rho_{\mathrm{N}}(r)]^{1/3} , \qquad \sigma_{\mathrm{pp}} = 33.2 \text{ mb} , \quad \sigma_{\mathrm{pn}} = 72.7 \text{ mb} . \tag{3.26}$$

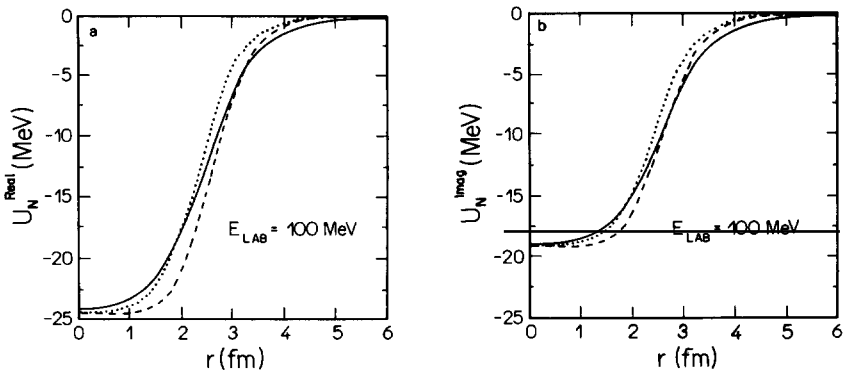

Fig. 24. The $t\rho$ optical potential for p + ^{9}Li (dotted), p + ^{11}Li (solid) and p + ^{12}C (dashed) at E_{lab} = 100 MeV. (a) real, (b) imaginary.

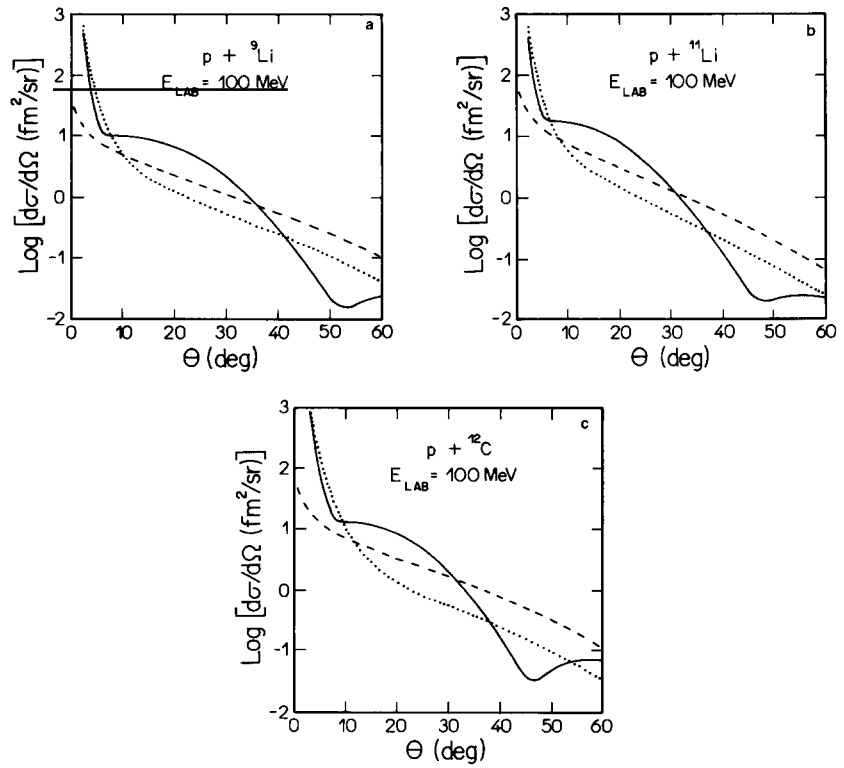

Fig. 25. The elastic scattering differential cross section (solid line) versus center-of-mass angle for (a) p + ^{9}Li, (b) p + ^{11}Li and (c) p + ^{12}C at E_{lab} = 100 MeV. Also shown are the near (dotted) and far (dashed) contributions.

In fig. 24 we show the resulting optical potential for the three systems p + ^{9}Li, p + ^{11}Li and p + ^{12}C. They look very similar except for the strength which is larger the heavier the target is, as expected from eq. (3.22) and fig. 22. However, the p + ^{11}Li has a much larger diffuseness as anticipated owing to the presence of the halo. In all cases, the real part is attractive. Absorption is also strong owing to the strong coupling to the single nucleon knockout channel.

The elastic scattering angular distributions calculated from eq. (3.7) are shown in fig. 25. The near contribution and the far contribution to $d\sigma/d\Omega$ are also shown individually. In all three cases,

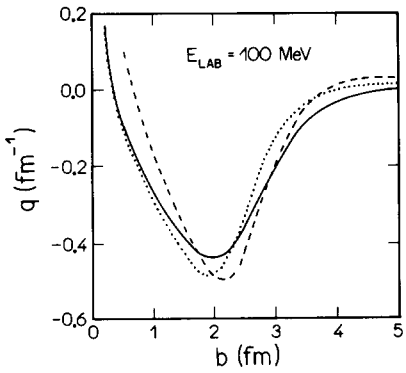

Fig. 26. The momentum transfer function $q(b(\vartheta))$ for the three systems studied. The solid line is for ^{11}Li, the dotted line is for ^{9}Li, and the dashed line is for ^{12}C.

the far side component dominates over the near side one, at least in the $\theta > 10°$ region. However, a very important qualitative change due to the relatively large size of ^{11}Li (the halo) is the fact that the position of the minimum occurs at $\theta = 30°$ in ^{9}Li, $\theta = 28°$ in ^{11}Li and $\theta = 31°$ in ^{12}C, clearly showing the influence of the greater extention of the matter distribution in ^{11}Li. This feature should be easily tested experimentally.

To further understand the nature of the scattering, we have also calculated the momentum transfer function $q(b(\theta))$ of eq. (3.13) for the three systems. This function, in the Glauber theory, has a similar role as the classical deflection function extensively studied in the semiclassical treatment of scattering, e.g., of heavy ions. In fig. 26 we show the real part of $q(b(\theta))$ versus b for the three systems under study. Again, whereas the region $0 < b < 3$ fm is as expected from general nuclear systematics, the region $b > 3$ fm exhibits clearly the effect of the halo. Appreciably larger impact parameters seem to contribute to the scattering of p + ^{11}Li than to the scattering of p + ^{9}Li and p + ^{12}C for a given value of the momentum transfer (angle).

To complete the comparison among the three systems, we performed the elastic scattering calculation at $E_{lab} = 800$ MeV A. Although the experiment at this energy is very difficult, owing to the very low current of the ^{11}Li secondary beam, we felt that such a comparison would further elucidate the question of the neutron halo. Thus in figs. 27, 28 and 29 we present the corresponding $t\rho$ optical potential, the elastic scattering angular distribution with its near–far decomposition and the momentum transfer function, respectively. The nucleon–nucleon total cross sections and the parameters ξ_{pN} used in the calculation were taken from the literature and are $\sigma_{pp} = 47.3$ mb, $\sigma_{pn} = 37.9$ mb, $\xi_{pp} = 0.06$ and $\xi_{pn} = -0.2$.

At $E_{lab} = 800$ MeV A, the real part of the $t\rho$ optical potential is repulsive and the imaginary part is quite strong (fig. 27). The momentum transfer function emphasizes this point in fig. 29. This favors a situation of almost equality between the near and far contributions to $d\sigma/d\Omega$. The resulting Fraunhofer pattern is clearly seen in fig. 28 for the three systems. Unfortunately, at this higher energy, the change in the oscillatory pattern of $d\sigma/d\Omega$ arising from the neutron halo is very small, making its study at this energy quite difficult. Finally, to complete the comparison between the three systems, we present the values of the total reaction cross section σ_R at the two energies considered in table 7. Although, σ_R for p + ^{11}Li is considerably larger than that of p + ^{9}Li and p + ^{12}C at both energies, the trend with energy, namely $\sigma_R(E_{lab} = 800\ \text{MeV}) < \sigma_R(E_{lab} = 100\ \text{MeV})$, is fully understood from the general behaviour of σ_{NN} and nuclear transparency [HRB 91].

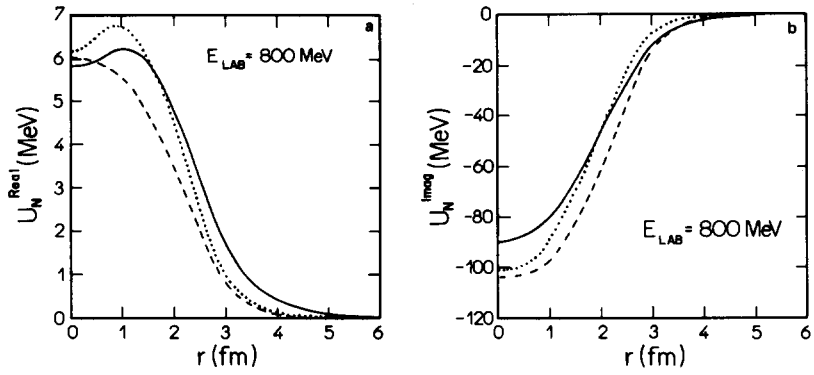

Fig. 27. Same as fig. 24 at E_{lab} = 800 MeV.

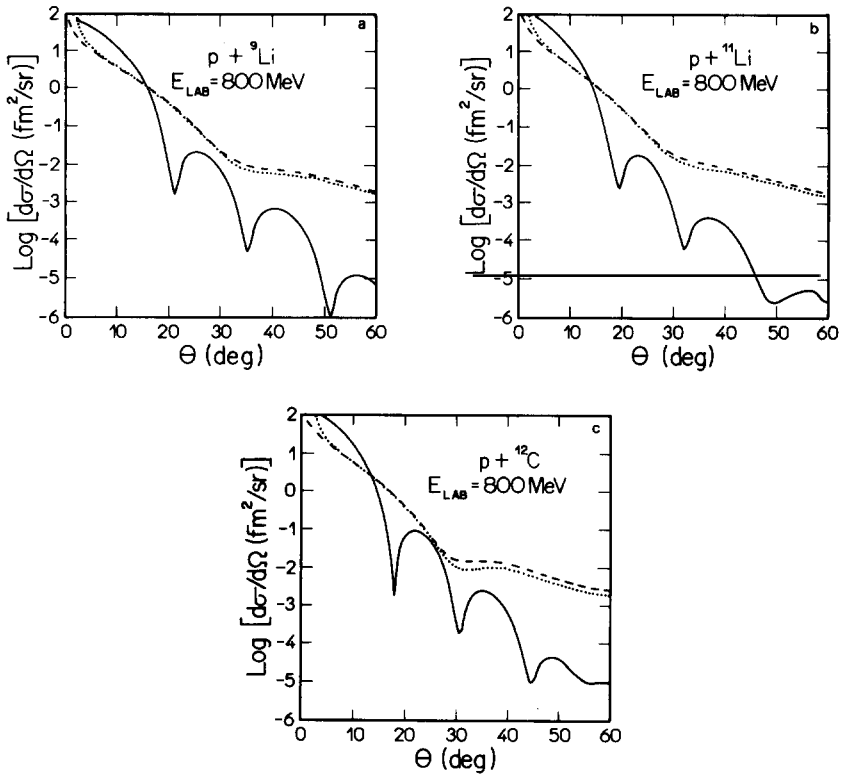

Fig. 28. Same as fig. 25 at E_{lab} = 800 MeV.

3.2.3. *The optical potential for the α + ^{11}Li system*

In this section, we extend our study (see also ref. [ABH 91]) of p + ^{11}Li to the case of α + ^{11}Li [ABH 92]. The tightly bound α-particle should prove an interesting probe as it represents, at low energies, a heavier charged "nucleon". To what extend the halo of ^{11}Li is sensitive to the size of the impinging particle, is a question that can be partly answered by comparing the two systems p + ^{11}Li and α + ^{11}Li at relatively low energies. We take this to be E_{lab} = 26 MeV A, since precise data [Pl 71] on the elastic scattering of p from α exist and can be used to extract the p–α optical potential. This potential is then used to calculate the α–^{11}Li single folding optical potential. Since

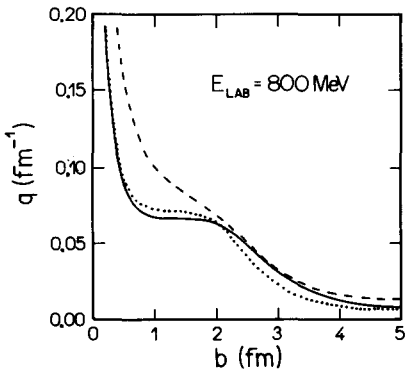

Fig. 29. Same as fig. 26 at $E_{lab} = 800$ MeV.

Table 7
Total reaction cross section for the system p + X

X	E (MeV)	σ_R (mb)
^{12}C	100	357.64
	800	344.68
^{11}Li	100	597.20
	800	474.11
^{9}Li	100	339.25
	800	288.58

the energy is too low for the usual [HRB 91] single folding approximation to the potential to be valid, we also calculate the second-order contribution which carries important information about nucleon–nucleon short-range correlations in the nucleus. We then write, for the first-order potential

$$V_N^{(1)}(\boldsymbol{r}) = \int d^3r'\, V_{p\alpha}(\boldsymbol{r} - \boldsymbol{r}')\rho_{Li}(\boldsymbol{r}') \,. \tag{3.27}$$

The potential extracted from the elastic scattering of protons from α particles at 26 MeV A laboratory energy is shown in fig. 30. The elastic scattering data of [Pl 71] are shown in fig. 31. The core neutrons and protons in ^{11}Li certainly feel a potential which is slightly different from $V_{p\alpha}$ because of medium effects. On the other hand, the halo neutrons in the $1p_{3/2}$ levels, being very loosely bound, should behave almost as free neutrons. So, the "experimental" $V_{p\alpha}$ of fig. 30 should be quite adequate in describing their interaction with α.

In principle, a better treatment for the α + ^{11}Li interaction would be taking a double folding potential for the ^{9}Li + α interaction, and a single folding one for the interaction of the halo,

$$V_N^{(1)} = \langle t_{NN} \rangle \int d^3r'\, \rho_\alpha(r')\rho_{^9Li}(\boldsymbol{r} - \boldsymbol{r}') + \int d^3r'\, V_{n\alpha}(\boldsymbol{r} - \boldsymbol{r}')\rho_{2n}(\boldsymbol{r}') \,, \tag{3.28}$$

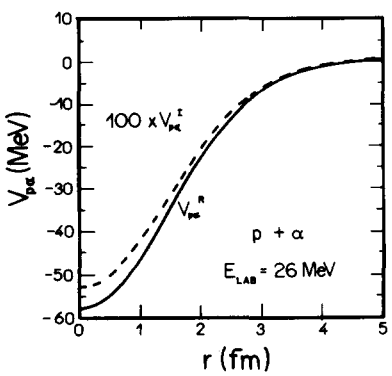

Fig. 30. Imaginary part (dashed curve) and real part (solid curve) of the optical potential for p + α scattering.

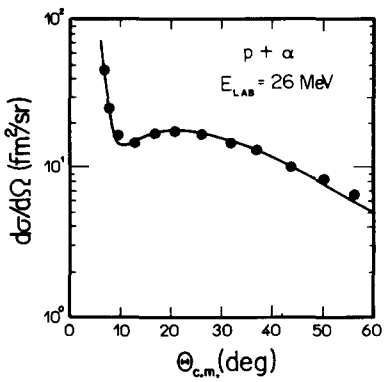

Fig. 31. Elastic scattering cross section for the system p + α at 26 MeV/nucleon. Data are from ref. [Pl 71]. Solid curve is a calculation using the potential of fig. 30 (see text for details).

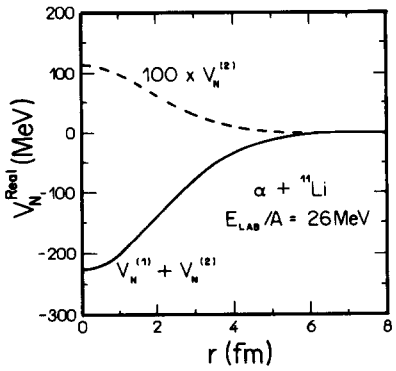

Fig. 32. Real part of the second-order correction for the α–^{11}Li optical potential (dashed line). The solid line is the sum of the first- and second-order potentials [eqs. (3.27) and (3.29)].

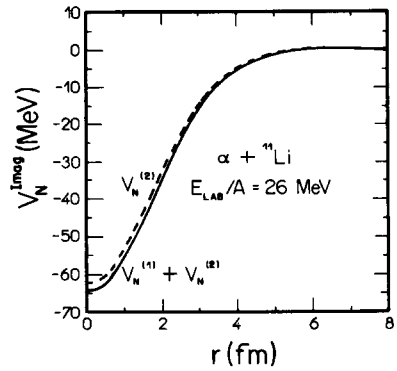

Fig. 33. Same as fig. 32, but for the imaginary part of the potentials.

where $\langle t_{NN} \rangle$ is the medium-modified nucleon–nucleon t-matrix calculated in the forward direction. We have compared eqs. (3.27) and (3.28) and found the difference in the real and imaginary parts to be less than 10%. Thus, for simplicity we shall in the following use eq. (3.27) for $V_N^{(1)}(r)$.

In ref. [HRB 91] a detailed discussion of second-order potential which contains the nucleon–nucleon short-range effects has been given. Within a single folding framework, this potential, which we denote by $V_N^{(2)}(r)$ is given by

$$V_N^{(2)} = -\frac{ik_\alpha}{2E_\alpha} R_{corr} \int [V_{p\alpha}(r - r')]^2 \rho_{Li}(r') \, d^3r' , \tag{3.29}$$

where $R_{corr.}$ is the correlation length and is generally taken to be -0.411 fm and $k_\alpha(E_\alpha)$ is the wave number (energy) of the α particle. In figs. 32 and 33 we show the real and the imaginary parts of $V_N^{(2)}(r)$ and the sum $V_N^{(1)}(r) + V_N^{(2)}(r)$. The effect of $V_N^{(2)}(r)$ is quite noticeable.

3.2.4. The elastic scattering of α + ^{11}Li

Before we show our results for the angular distribution of the elastic scattering of the system α + ^{11}Li at $E_{lab} = 26$ MeV A, we first discuss the nature of the refraction in this system, exemplified by the momentum transfer function $q(b)$ of eq. (3.13) (the right-hand side of this equation). In fig. 34 we show $q(b)$ for α + ^{11}Li (solid line) calculated with $V_N^{(1)}$ and with $V_N^{(1)} + V_N^{(2)}$. Very little change is seen when the second-order potential is added. However, the absorption content of $V_N^{(1)} + V_N^{(2)}$ is quite different from $V_N^{(1)}$, as will be seen next. For comparison we also exhibit (dashed curve) $q(b)$ for α + ^{12}C at the same energy ($E_{lab} = 26$ MeV A). Again a small effect is seen to arise from $V_N^{(2)}$. Notice that the nuclear rainbow (the dip at negative q) is at a larger negative q in ^{12}C than in ^{11}Li. The large-b behavior of $q(b)$ is slightly different in the two systems.

The cross section for α + ^{11}Li calculated with $V_N^{(1)}$ and $V_N^{(1)} + V_N^{(2)}$ is shown in fig. 35. We see here a drastic change in behavior at larger angles ($\theta > 10°$), which arises from the different absorption content in the two potentials. Figure 36 is the result of the same calculations, but for the system α + ^{12}C. Again for comparison, we show in fig. 37 the α + ^{12}C as compared to the α + ^{11}Li results. This figure implies stronger refraction seen in α + ^{11}Li, which corroborates the findings of section 3.1 on the ^{11}Li + ^{12}C systems.

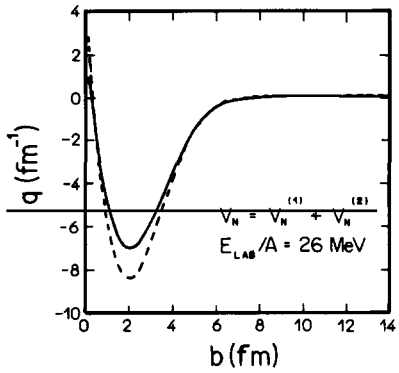

Fig. 34. Classical momentum transfer (eq. 3.13) as a function of impact parameter for the reactions $\alpha + {}^{11}$Li (solid line) and $\alpha + {}^{12}$Li (dashed line).

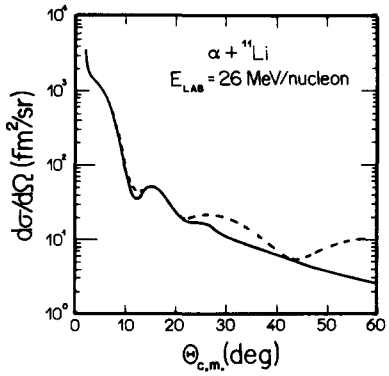

Fig. 35. Elastic cross section for the system $\alpha + {}^{11}$Li at 26 MeV/nucleon. The dashed line was calculated with the first-order optical potential. The solid line includes the contribution of the second-order potential.

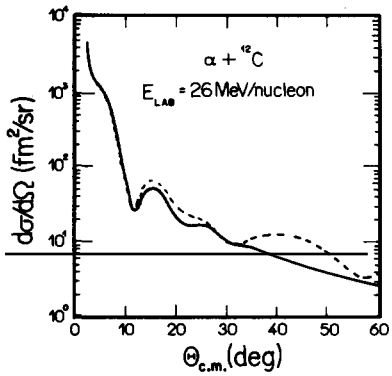

Fig. 36. Same as fig. 35, but for the system $\alpha + {}^{12}$C at 26 MeV/nucleon.

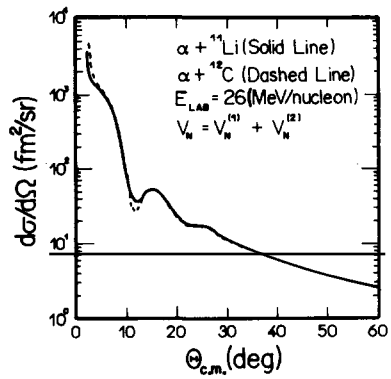

Fig. 37. Comparison between the elastic cross section for the systems $\alpha + {}^{11}$Li and $\alpha + {}^{12}$C at 26 MeV/nucleon. Both calculations include the contribution of the second-order potential.

To better understand the nature of the angular distribution, we show in fig. 38 the near and far contributions to $d\sigma/d\Omega$ both for $V_N^{(1)}$ and $V_N^{(1)} + V_N^{(2)}$. It is clear that, in both cases, the angular distribution is far side dominated, indicating great sensitivity to the nuclear potential at shorter distances. However, the oscillations (Airy) in the far side amplitude, are washed out when $V_N^{(1)} + V_N^{(2)}$ is used. This shows that $V_N^{(2)}$ contributes basically to absorption in such a way as to damp the contribution to $f_{far}(\theta)$ arising from the inner stationary phase point. This feature is common to both $\alpha + {}^{11}$Li and $\alpha + {}^{12}$C.

3.3. Polarization potentials

3.3.1. Derivation

The mean effect of the coupling between the elastic channel and excited states is expressed by the optical potential [Fe 62]. Instead of deriving this potential from first principles, one frequently adopts a phenomenological approach, expressing it in terms of a few parameters. These parameters, which may have a weak energy and/or mass dependence, are then fitted to a set of

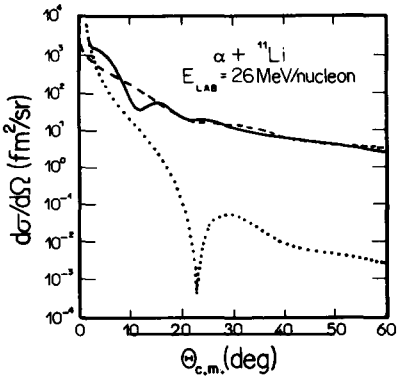

Fig. 38. Near (dotted curve) and far side (dashed curve) contribution to the elastic scattering cross section (solid) for the system $\alpha + {}^{11}Li$ at 26 MeV/nucleon.

scattering data. When, however, a few channels have strong influence on the elastic scattering, it is necessary to handle the coupling with these channels separately. One possible approach is to express such effects as a correction to the optical potential. If one is able to obtain this correction, usually known as a polarization potential, the calculation of the elastic and the reaction cross sections reduces to the simple task of solving a one-channel Schrödinger equation. This approach has been used in several situations (for a review see ref. [HBC 84]), including the cases of rotational [LTS 77; BKG 78; DCH 79a] and vibrational [DCH 79b] excitations and that of transfer channels [BPW 81; SB 82; FH 80].

In this section we discuss the derivation of the polarization potential resulting from the coupling to states corresponding to the removal of a neutron pair from ^{11}Li projectiles. This potential has been calculated by Canto et al. [CDH 91a] for high-energy collisions with light targets. These authors neglect the effects of the Coulomb field and use the eikonal approximation. In a more recent paper [CDH 91b], the calculation has been extended to lower energies and Coulomb effects have been included. This section describes the polarization potentials obtained with the more general treatment of the latter, and its applications.

Following the procedure introduced by Feshbach [Fe 62] for the derivation of the optical potential, one defines the projection operators

$$P = |\phi_0\rangle\langle\phi_0| , \qquad Q = 1 - P ,$$

where $\phi_0(\boldsymbol{x}) \equiv \phi_0(x)$ represents the bound state of the 2n + ^9Li system while Q is the projector onto states of the 2n pair in the continuum. The polarization potential can then be written

$$V(\boldsymbol{r}, \boldsymbol{r}') = \langle \boldsymbol{r};\, \phi_0 | v Q G^{(+)} Q v | \phi_0;\, \boldsymbol{r}' \rangle , \tag{3.30}$$

where v is the coupling interaction and $G^{(+)}$ is the optical Green's operator. In order to evaluate eq. (3.30), we write the projector Q in its spectral form

$$Q = \int |\phi_q\rangle\langle\phi_q| \, \mathrm{d}q , \tag{3.31}$$

with q standing for the set of quantum numbers that characterize the continuum states.

With the introduction of representations in the space of the relative coordinate $\boldsymbol{r}$ and with the assumption that the interaction v is local, the polarization potential can be put in the form

$$V(\boldsymbol{r}, \boldsymbol{r}') = \mathscr{F}(r) G^{(+)}(\boldsymbol{r}, \boldsymbol{r}') \mathscr{F}(r') , \tag{3.32}$$

with the scalar form factor

$$\mathscr{F}(r) = U(r) \left(\int \phi_0^2(x) u^2(x) \, \mathrm{d}x \right)^{1/2} . \tag{3.33}$$

In the derivation of eq. (3.33), the following assumptions have been made:

- the energies of the relevant states ϕ_q of eq. (3.31) are small as compared to the collision energy,
- the matrix element $\langle \phi_0 | v | \phi_0 \rangle$ is negligible,
- the coupling potential is separable in the form: $v(\boldsymbol{r}, x) \approx U(r) u(x)$, where $U(r)$ is the real part of the ^{11}Li-target optical potential and $u(x)$ is an internal excitation form factor [BH 91a; BCH 92].

Performing the partial-waves expansion of the polarization potential and writing the l-projected Green's function explicitly, one gets the l-components of the polarization potential

$$V_l(r, r') = \mathscr{F}(r) [-(2\mu/\hbar^2 k) f_l(kr_<) h_l^{(+)}(kr_>)] \mathscr{F}(r') . \tag{3.34}$$

Above, $f_l(kr_<)$ and $h_l^{(+)}(kr_>)$ are, respectively, the regular and the outgoing solutions of the radial equation with the optical potential.

For practical applications, it is convenient to use the trivially equivalent local potential, defined as [LTS 77]

$$V_l^{\mathrm{pol}}(r) = \frac{1}{f_l(kr)} \int V_l(r, r') f_l(kr') \, \mathrm{d}r' , \tag{3.35}$$

and adopt the on-shell approximation for the Green's function [LTS 77]. This approximation amounts to replacing $h_l^{(+)} \to \mathrm{i} f_l$ and its validity has been discussed in details in ref. [PC 90]. It leads to a separable Green's function and the trivially equivalent local potential takes the form

$$V_l^{\mathrm{pol}}(r) = -\mathrm{i} \frac{2\mu}{\hbar^2 k} \mathscr{F}(r) |S_l^{(1)}| \int_0^\infty \mathscr{F}(r') F_l^2(kr') \, \mathrm{d}r' , \tag{3.36}$$

where $S_l^{(1)}$ is the l-component of the optical S-matrix and $F_l(kr)$ is the regular Coulomb function [AS 64]. To get eq. (3.36), the authors have approximated the radial wave function as $f_l(kr) \simeq |S_l^{(1)}|^{1/2} F_l(kr)$.

In the r-region of interest for the 2n-removal process, only the tail of $U(r)$ is relevant. Therefore, the form factor can be written

$$\mathscr{F}(r) = \mathscr{F}_0 \mathrm{e}^{-r/\alpha}, \quad \mathscr{F}_0 = C \mathrm{e}^{R_0/\alpha} . \tag{3.37a, b}$$

In eq. (3.37b), C is a constant which can be obtained from eq. (3.33), $R_0 = R_{^{11}\mathrm{Li}} + R_{\mathrm{target}}$, and α is the diffusivity associated to the optical potential $U(r)$. Substituting eq. (3.37a) into eq. (3.36), one gets

$$V_l^{\mathrm{pol}}(r) = -\mathrm{i}W_0(l, E)\mathrm{e}^{-r/\alpha} . \tag{3.38}$$

The strength $W_0(l, E)$ is given by

$$W_0(l, E) = (|\mathscr{F}_0|^2/E)\,|S_l^{(1)}|\,I_l(\eta, s) , \tag{3.39}$$

in terms of the radial integral

$$I_l(\eta, s) = \int_0^\infty \mathrm{e}^{-s\rho} F_l^2(\rho)\,\mathrm{d}\rho , \quad s = 1/k\alpha , \tag{3.40}$$

where η is the Sommerfeld parameter.

Using the asymptotic WKB approximation for $F_l(\rho)$ [AW 75],

$$F_l(\rho) \approx \left(1 - \frac{2\eta}{\rho} - \frac{l(l+1)}{\rho^2}\right)^{-1/4} \sin\left[\tfrac{1}{4}\pi + \int_{\rho_0}^{\rho}\left(1 - \frac{2\eta}{\rho} - \frac{l(l+1)}{\rho^2}\right)^{1/2} \mathrm{d}\rho\right], \tag{3.41}$$

where $\rho \equiv kr$ and ρ_0 is the value of ρ calculated at the turning point of the Rutherford trajectory, one obtains

$$I_l(\eta, s) = (\mathrm{e}^{-\pi s}/2s)\,[\eta s K_0(X) + XK_1(X)] . \tag{3.42}$$

In eq. (3.42), $K_0(X)$ and $K_1(X)$ are modified Bessel functions with the argument

$$X = \eta s[1 + l(l+1)/\eta^2]^{1/2} . \tag{3.43}$$

The variable X measures the distance of closest approach in a Rutherford trajectory, in units of α. To a good approximation, the radial integral $I_l(\eta, s)$ can be parametrized as

$$I_l(\eta, s) \approx (0.75/s)\mathrm{e}^{-0.83X} . \tag{3.44}$$

The use of this parametrization in eq. (3.44) leads to a very useful formula for the strength of the polarization potential.

For a comparison with the results of ref. [CDH 91a], the high-energy and large-l limit was investigated. In this limit the polarization potential of eq. (3.38) was shown to be identical to that obtained within the eikonal approximation [CDH 91a].

3.3.2. Nuclear 2n-removal cross section

Using the above described polarization potential, one obtains an expression for the ^{11}Li nuclear 2n-removal cross section.

The starting point is the formal definition of the nuclear break-up cross section

$$\sigma^{2n} = (k/E)\langle \Psi_k^{(+)}| - \mathrm{Im}(V^{\mathrm{pol}})|\Psi_k^{(+)}\rangle \,, \tag{3.45}$$

where $|\Psi_k^{(+)}\rangle$ is the exact elastic scattering wave function and V^{pol} is the 2n-removal polarization potential, which accounts for the effect of the breakup process on the elastic scattering. If the total optical potential that generates $|\Psi_k^{(+)}\rangle$ is denoted by U^{el} then the bare interaction taking into account other channel-coupling effects is $U^{\mathrm{opt}} \equiv U^{\mathrm{el}} - V^{\mathrm{pol}}$.

Performing a partial-waves expansion, one may write eq. (3.45) as

$$\sigma^{2n} = \frac{\pi}{k^2} \sum_{l=0}^{\infty} (2l+1) T_l^{2n} \,, \tag{3.46}$$

$$T_l^{2n} = \frac{4k}{E} \int_0^{\infty} \mathrm{d}r\, |f_l^{\mathrm{el}}(kr)|^2 [\, -\mathrm{Im}(V_l^{\mathrm{pol}})] \,. \tag{3.47}$$

In the above equation $f_l^{\mathrm{el}}(kr)$ is the optical radial wave function, which is the regular solution of the elastic-channel Schrödinger equation with the potential U^{el}.

One now employs the same kind of approximation used in eq. (3.34), namely $f_l^{\mathrm{el}}(kr) \approx |S_l^{(0)}|^{1/2} \hat{f}_l(kr)$, where $S_l^{(0)}$ is the nuclear elastic S-matrix calculated with U^{opt} and $\hat{f}_l(kr)$ represents the scattering wave function generated by the potential $V^{\mathrm{Coul}} + V^{\mathrm{pol}}$. Approximating $\hat{f}_l(kr)$ by the properly normalized analytic extension of eq. (3.41), we obtain

$$\hat{f}_l(\rho) \approx N \left[1 - \frac{2\eta}{\rho} - \frac{l(l+1)}{\rho^2} + \mathrm{i} \frac{\mathrm{Im}(V_l^{\mathrm{pol}})(\rho/k)}{E} \right]^{-1/4}$$

$$\times \sin\left[\tfrac{1}{4}\pi + \int_{\rho_0}^{\rho} \left(1 - \frac{2\eta}{\rho} - \frac{l(l+1)}{\rho^2} + \mathrm{i} \frac{\mathrm{Im}(V_l^{\mathrm{pol}})(\rho/k)}{E} \right)^{1/2} \mathrm{d}\rho \right], \tag{3.48}$$

where the normalization factor N is given by

$$N^2 = \int_0^{\infty} \mathrm{d}r\, |\hat{f}_l(kr)|^2 = \exp\left(- \int_{\rho_0}^{\infty} \mathrm{d}\rho \frac{\mathrm{Im}(V_l^{\mathrm{pol}})/E}{[1 - 2\eta/\rho - l(l+1)/\rho^2]^{1/2}} \right) \equiv |\hat{S}_l| \,. \tag{3.49}$$

If we now expand $|\hat{f}_l(\rho)|^2$ to lowest order in $\mathrm{Im}(V_l^{\mathrm{pol}})/E$, substitute it in eq. (3.47) and perform the integration, we obtain

$$T_l^{2n} = 2|S_l^{(0)}||\hat{S}_l| \sinh\left(\int_{\rho_0}^{\infty} \mathrm{d}\rho \frac{\mathrm{Im}(V_l^{\mathrm{pol}})/E}{[1 - 2\eta/\rho - l(l+1)/\rho^2]^{1/2}} \right)$$

$$= \left[1 - \exp\left(-2 \int_{\rho_0}^{\infty} \mathrm{d}\rho \frac{\mathrm{Im}(V_l^{\mathrm{pol}})/E}{[1 - 2\eta/\rho - l(l+1)/\rho^2]^{1/2}} \right) \right] |S_l^{(0)}| = (1 - |\hat{S}_l|^2)|S_l^{(0)}| \,. \tag{3.50}$$

Using the explicit form of V^{pol} [eqs. (3.44)–(3.48)] it is easy to show that $|\hat{S}_l|$ can be written as

$$|\hat{S}_l| = \exp[-(2\mathscr{F}_0^2/E^2)|S_l^{(0)}|I_l^2(\eta, s)] \,. \tag{3.51}$$

At high energies it is safe to set $\eta = 0$ and for the distant collisions under consideration we may set $|S_l^{(0)}| \simeq |S_l^{(1)}| \simeq 1$. Under these conditions the nuclear breakup cross section agrees with that found using the eikonal approximation (ref. [CDH 91a]).

3.3.3. *Applications*

The polarization potential discussed in the previous section was applied to collisions with a ^{12}C target. In this case the Coulomb field is weak and the 2n-removal process is dominated by the nuclear interaction. A typical strong absorption optical potential was used to determine $S_l^{(1)}$ and the value $\mathscr{F}_0 = 2.7$ MeV was adopted for the form-factor strength. This value resulted from a fit of the theoretical reaction cross section at $E_{lab} = 50$ MeV A to the experimental value of Shimoura et al. [Sh 91]. In this fit, the reaction cross section was approximated by the sum of the contributions from the 2n-removal process and from the absorption arising from the optical potential.

The strengths of the polarization potential at the bombarding energies $E_{lab} = 20$, 50 and 100 MeV A are shown in fig. 39, as functions of the angular momentum.

The accuracy of the approximations involved in the derivation of eq. (3.50) can be tested in a comparison with the exact expression of eq. (3.47). This comparison is shown in fig. 40, for three

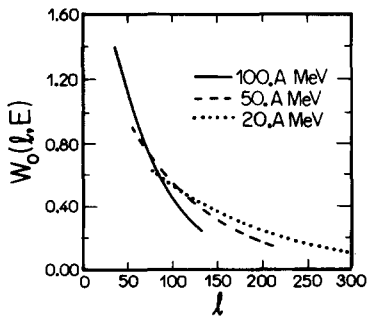

Fig. 39. The strengths of the imaginary part of the polarization potential as a function of l for different collision energies.

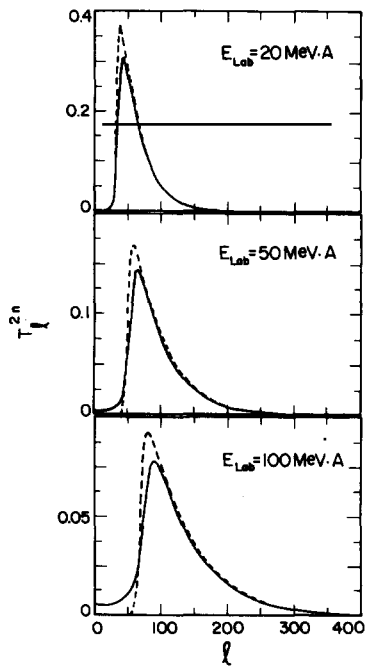

Fig. 40. The transmission coefficient as a function of l for three different energies. The solid lines represent the results of the calculation using eq. (3.47) and the dashed lines those using the approximation of eq. (3.50).

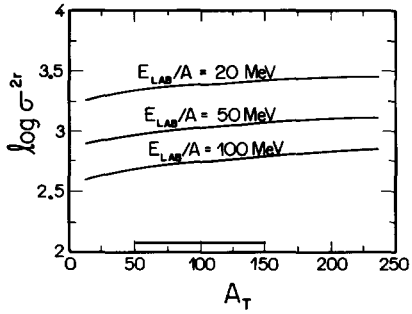

Fig. 41. The ^{11}Li 2n-removal cross section in collisions with a ^{12}C target, as a function of the laboratory energy.

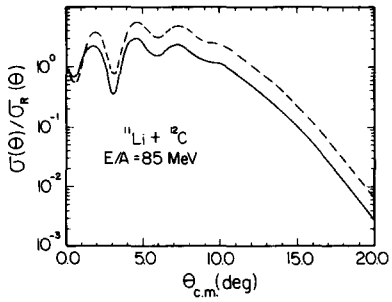

Fig. 42. The angular distribution in the elastic scattering of ^{11}Li + ^{12}C, normalized to the Rutherford cross section. The solid (dashed) line is the result of an optical-model calculation without (with) the inclusion of the polarization potential.

different collision energies. For the calculation of the transmission coefficient of eq. (3.47), the wave function $f_l^{\rm el}(kr)$ was obtained by solving the radial Schrödinger equation with the full interaction potential $U^{\rm el}$.

Figure 41 shows the energy dependence of the predicted 2n-removal cross section as a function of the collision energy. It shows a significant increase for low energies. Figure 42 shows the effects of the polarization potential on the angular distribution of the ^{11}Li + ^{12}C elastic scattering, at $E_{\rm lab} = 85$ MeV A. The dashed line corresponds to the optical-model calculation of Satchler et al. [SMH 91] while the solid line was obtained with the addition of the polarization potential to the same calculation. In this case the potential $V^{\rm pol}$ was calculated within the eikonal approximation (see ref. [CDH 91a]). The comparison indicates that the absorption resulting from the 2n-removal process leads to an average increase of 40% in the damping.

The extension of the calculations to other targets is straightforward. It is sufficient to scale the strength of the form factor in terms of the radius $R_{\rm T}$ of the new target. According to eq. (3.37b), we have

$$\mathscr{F}_0(A_{\rm T}) = \mathscr{F}_0(^{12}{\rm C})\exp\left[(R_{\rm T} - R_{\rm C})/\alpha\right], \tag{3.52}$$

where $R_{\rm C}$ stands for the radius of the ^{12}C target. The resulting 2n-removal cross sections are shown in fig. 43 for the three energies considered in the previous figures, as a function of the target mass.

So far in our discussion, we have ignored completely the real part of the breakup polarization potential. In order to complete our discussion in the chapter we give below a brief account of this question.

We calculate the real part of $V_{\rm pol}$ using the dispersion relation, which reads

$$\mathrm{Re}\, V_{\rm pol}^{(E)} = \frac{\rm P}{\pi}\int \frac{\mathrm{Im}\, V_{\rm pol}(E')}{E - E'}\,{\rm d}E', \tag{3.53}$$

where P stands for the principal value of the integral. The above formula assumes a similar r-dependence for Re $V_{\rm pol}$ and Im $V_{\rm pol}$. Using the Im $V_{\rm pol}$ calculated in this chapter we obtain a real part which is dominantly repulsive and reaches, at most, the value of 0.5 MeV. This value could, to some extent, affect the value of the elastic angular distribution and the sub-barrier fusion cross

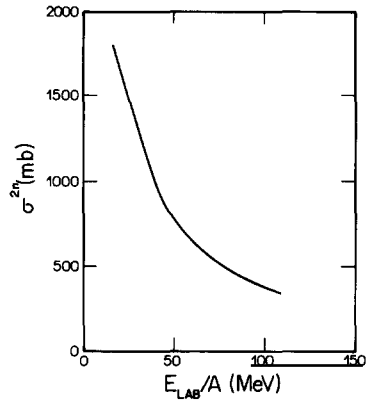

Fig. 43. Target mass dependence of the ^{11}Li nuclei 2n-removal cross section. For simplicity a sharp-cutoff model for $|S_i^{(0)}|$ (eq. 3.50) is used.

section discussed in chapter 5. For lack of space we leave the detailed discussion of the above to another publication [Hu 92].

Finally, we point out that several works have also treated the elastic scattering problems of ^{11}Li, and other neutron-rich nuclei, on nuclear targets. We cite, e.g., the works of Yabana, Ogawa and Suzuki [YOS 92a, b] and Takigawa et al. [TUK 92].

4. Pion production with radioactive nuclei

In this chapter we will investigate the possibility to further determine the coordinate and momentum space distribution of neutrons inside weakly bound isotopes via pion production with radioactive beams.

In the next section, we discuss the inclusive π^+ and π^- production cross section in reactions of radioactive beams in the context of a Glauber-type multiple-collision model, and we focus on the possibility of probing the difference between proton and neutron densities by studying the ratio of π^+ and π^- production cross sections. Section 4.2 contains our results regarding the pion energy spectra studied within a modified Fermi gas model.

4.1. Inclusive π^+ and π^- production cross section

In principle, pion production in nucleus–nucleus collisions can be described with nuclear transport models developed during the last decade [LB 91; Ba 89; Ca 90]. These models have been successful to describe particle production in heavy ion collisions. However, they are semiclassical in nature and therefore lack the capability to properly take into account the special nuclear structure features of weakly bound nuclei near the drip line. It is therefore necessary to construct a more phenomenological model. The model we present in the following [LHB 91] is not able to provide a complete time-dependent description of heavy-ion reactions, as the above-mentioned transport models can. But the model is more precise as far as utilizing nuclear-structure information is concerned. In the following, we perform a calculation similar to the one presented by Lombard and Maillet [LM 88; TLM 87], but using the shell-model densities and energy-dependent cross sections.

Within a Glauber-type multiple-collision model, the total number of nucleon–nucleon collisions in the reaction of A + B at an impact parameter b is

$$N(b) = \bar{\sigma}(E) \int_{\mathcal{O}} dx\, dy \int dz_1\, dz_2\, \rho_A(x^2 + y^2 + z_1^2)^{1/2} \rho_B(x^2 + (y-b)^2 + z_2^2)^{1/2}\,, \tag{4.1}$$

where $\mathcal{O}$ is the overlap region of nuclei A and B, and $\bar{\sigma}(E)$ is the momentum-averaged total nucleon–nucleon cross section. For ^{11}Li, since the core nucleon and halo neutron have different momentum distributions, it may be written as

$$\bar{\sigma}(E) = \tfrac{9}{11}\,\bar{\sigma}_{\text{core}}(E) + \tfrac{2}{11}\,\bar{\sigma}_{\text{halo}}(E)\,. \tag{4.2}$$

Since we wish to analytically carry out the bulk of our calculations, following Karol [Ka 75] we assume that the nucleon density distribution is a Gaussian function

$$\rho(r) = \rho(0) \exp(-r^2/a^2)\,. \tag{4.3}$$

The integration in eq. (4.1) can then be performed analytically to yield the result

$$N(b) = \frac{\bar{\sigma}(E)\pi^2 \rho_A(0)\rho_B(0) a_A^3 a_B^3}{a_A^2 + a_B^2} \exp\left[-b^2/(a_A^2 + a_B^2)\right]. \tag{4.4}$$

Similar forms for the proton–proton and neutron–neutron collision numbers can be obtained in terms of their density-distribution parameters.

Under the assumption that pions are produced through Δ resonances, and neglecting the π^+ and π^- produced in neutron–proton collisions, the inclusive π^+ and π^- cross section can then be written as [LM 88]

$$\frac{d\sigma_{\text{inc}}^{\pi^+}}{d\Omega} = |f_{n\Delta}(q)|^2 Z_A Z_B \frac{\pi^2 \rho_{ZA}(0)\rho_{ZB}(0) a_{ZA}^3 a_{ZB}^3}{a_{ZA}^2 + a_{ZB}^2} \times 2\pi \int_0^\infty b\, db \exp\left[-\frac{b^2}{a_{ZA}^2 - a_{ZB}^2} - \frac{\bar{\sigma}(E)(AB-1)\rho_A(0)\rho_B(0) a_A^3 a_B^3}{a_A^2 + a_B^2} \exp\left(-\frac{b^2}{a_A^2 + a_B^2}\right)\right], \tag{4.5}$$

$$\frac{d\sigma_{\text{inc}}^{\pi^-}}{d\Omega} = |f_{n\Delta}(q)|^2 N_A N_B \frac{\pi^2 \rho_{NA}(0)\rho_{NB}(0) a_{NA}^3 a_{NB}^3}{a_{NA}^2 + a_{NB}^2} \times 2\pi \int_0^\infty b\, db \exp\left[-\frac{b^2}{a_{NA}^2 - a_{NB}^2} - \frac{\bar{\sigma}(E)(AB-1)\rho_A(0)\rho_B(0) a_A^3 a_B^3}{a_A^2 + a_B^2} \exp\left(-\frac{b^2}{a_A^2 + a_B^2}\right)\right], \tag{4.6}$$

where ρ_{Ni} and ρ_{Zi} are the neutron and proton coordinate-space densities of nucleus i, and $f_{n\Delta}(q)$ is the amplitude for the process $N + N \to N + \Delta$.

At beam energies smaller than 1 GeV/nucleon, available experimental data [VA 80; Ki 86] show that pions are mainly produced through Δ resonances, direct processes account for less than 20% and higher resonances have negligible cross sections. From the experimental data of n + p collisions [VA 80] and the calculated ratio of the isospin-space matrix elements [TLM 87], it is shown that the intensities of π^+ and π^- produced in n + p collisions are smaller than in p + p and n + n collisions, respectively, by an order of magnitude. We therefore expect that the above equations are good approximations for the present purpose of our calculation.

Since we are interested in the ratio of the inclusive π^+ and π^- production, the main ingredients in the model calculation are then the density parameters and the momentum-averaged cross sections.

We start out by obtaining realistic density distributions for protons and neutrons for all isotopes under consideration. This is accomplished by using a binding-energy adjusted shell-model program [BBS 89]. As examples for the calculated density distributions, we display in fig. 44 the neutron and proton densities for ^{12}C (upper part) and ^{11}Li (lower part) by the solid lines (see also fig. 22).

The results of the Gaussian fit to the calculated density distributions are represented by the dotted lines. In table 8, we list the obtained values for $\rho(0)$ and a for proton and neutron density distributions for all Li isotopes used in the subsequent calculations as well as the corresponding values for ^{12}C.

For calculating the momentum-averaged nucleon–nucleon cross sections, we choose our momentum-space distribution functions such that our results agree with known experimental data.

One such comparison is performed in fig. 1 (see section 2.1). In the upper part, we use a Fermi gas model for the momentum distribution of the neutrons in ^{11}Li. We assume different Fermi momenta for core and halo neutrons. The fitted values are P_F(core) = 158 MeV/c and P_F(halo) = 38 MeV/c which coincide with those inferred from the experimental data by using the Goldhaber model. By randomly picking two neutron momenta from within these Fermi spheres and adding their momenta, one obtains a recoil spectrum for ^{9}Li in the projectile rest frame, employing the assumptions entering the Goldhaber model [Go 74]. By picking two neutrons from the halo, one obtains the dotted curve in fig. 1. The dashed curve is the result of using the same procedure on two core neutrons. The solid curve is the result of an addition of the two contributions with the proper weights as measured in the experiment of Kobayashi et al. [Ko 88].

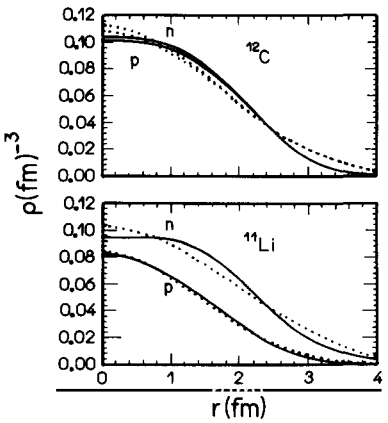

Fig. 44. Density distributions for ^{12}C and ^{11}Li. The solid lines are calculated with the binding-energy adjusted shell model. The dotted lines are the Gaussian fits to the density profiles.

Table 8
Parameters of the Gaussian fits to the nucleon density distribution in Li-isotopes and ^{12}C as calculated by Bertsch, Brown and Sagawa [BBS 89]

	$\rho_n(0)$ (fm^{-3})	a_n (fm)	$\rho_p(0)$ (fm^{-3})	a_p (fm)	$\rho(0)$ (fm^{-3})	a (fm)
^{12}C	0.1148	2.110	0.1120	2.128	0.2268	2.120
^{7}Li	0.1051	1.897	0.1121	1.688	0.2168	1.797
^{8}Li	0.1151	1.984	0.0996	1.755	0.2134	1.885
^{9}Li	0.1215	2.071	0.0989	1.760	0.2178	1.952
^{11}Li	0.1115	2.346	0.0851	1.851	0.1922	2.175

For purposes of comparison, all curves in the upper part of fig. 1 were normalized to the same value. In the lower part of this figure, we compare the simulated ^{9}Li transverse momentum spectra to the data of Kobayashi et al. [Ko 88]. One can see that we are able to reliably reproduce the experimental observables.

We obtain the momentum distribution averaged nucleon–nucleon cross sections by integrating $\sigma(\sqrt{s})$ weighted with the momentum distributions of target and projectile,

$$\bar{\sigma}(E_{\text{beam}}) = \int f_A(\boldsymbol{p}_A)\, f_B(\boldsymbol{p}_B - \boldsymbol{p}_{\text{beam}})\, \sigma(\sqrt{s}\,(\boldsymbol{p}_A, \boldsymbol{p}_B))\, d^3\boldsymbol{p}_A\, d^3\boldsymbol{p}_B\,. \tag{4.7}$$

Here, $f_i(\boldsymbol{p})$ are the momentum distributions of target $i = A$ and projectile $i = B$.

For the purpose of this calculation, we use the well known parametrizations of Cugnon [CMV 81] for the free-space elastic and inelastic nucleon–nucleon cross sections as a function of the available center of mass energy, $\sqrt{s}$, in a nucleon–nucleon collision,

$$\sigma_{\text{el}}(\sqrt{s}) = \frac{35}{1 + 100(s - 1.8993)} + 20\,, \qquad \sqrt{s} > 1.8993\,, \tag{4.8}$$

$$\sigma_{\text{inel}}(\sqrt{s}) = \frac{20(\sqrt{s} - 2.015)^2}{0.015 + (\sqrt{s} - 2.015)^2}\,, \qquad \sqrt{s} > 2.015\,. \tag{4.9}$$

In this parametrization, $\sqrt{s}$ is measured in GeV and σ in mb.

In fig. 45, we display the results for $\bar{\sigma}_{\text{inel}}(E_{\text{beam}})$ and $\bar{\sigma}_{\text{total}}(E_{\text{beam}})$ for three different cases. The solid lines are for free nucleons. In this case, the distribution functions f are δ-functions, and we have $\bar{\sigma}(E_{\text{beam}}) = \sigma_{\text{NN}}$. The threshold energy for pion production is in this case $E^{\text{th}}_{\text{beam}}$/nucleon = 290 MeV.

The dashed and dotted lines represent the case that the target is a carbon nucleus. $f_A(\boldsymbol{p})$ is then a Fermi gas distribution function with Fermi momentum of 221 MeV/c determined from the carbon fragmentation experiment [Ko 89]. The dashed lines are obtained by using the momentum distribution of ^{11}Li core neutrons for f_B, and the dotted line represents the case that the halo neutron momentum distribution is used. In these cases, the threshold energies for pion production are 70 MeV and 120 MeV, respectively.

One can see from fig. 45 that the distribution-averaged value of the total nucleon–nucleon cross section is largely unaffected by the momentum distribution of nucleons in target and projectile. However, the averaged inelastic cross section shows a very large effect close to the threshold.

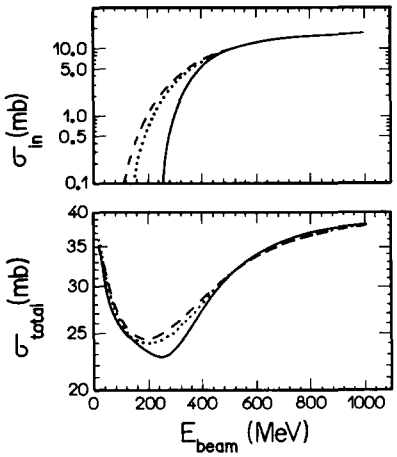

Fig. 45. Nucleon momentum-average nucleon–nucleon cross sections in the reaction ^{11}Li + ^{12}C. Solid lines are the free-space nucleon–nucleon cross sections. Dotted lines are for carbon nucleons colliding with halo neutrons and dashed lines are for carbon nucleons colliding with the core nucleons of ^{11}Li.

Table 9
Comparison of the computed normalized cross section differences between negative- and positive-pion production, E, for two different values of $\bar{\sigma}$ and the same quantity obtained from simple counting of nucleons, E_0, for reactions of different Li isotopes with ^{12}C

E (mb)	^{7}Li + ^{12}C	^{8}Li + ^{12}C	^{9}Li + ^{12}C	^{11}Li + ^{12}C
40	0.1153	0.2221	0.2955	0.3951
25	0.1143	0.2210	0.2939	0.3927
E_0	0.1429	0.2500	0.3333	0.4545

In table 9, we present the results of our calculation for the ratio

$$E = (\sigma_{\rm inc}^{\pi^-} - \sigma_{\rm inc}^{\pi^+})/(\sigma_{\rm inc}^{\pi^-} + \sigma_{\rm inc}^{\pi^+}) , \tag{4.10}$$

for the systems ^{A}Li + ^{12}C (A = 7, 8, 9, 11) with $\bar{\sigma}$ = 40 mb and 25 mb. These two values for $\bar{\sigma}$ are chosen to represent the case for nucleus–nucleus interactions around the pion production threshold ($E_{\rm beam} \approx 200$ MeV/nucleon $\rightarrow \bar{\sigma} \approx 25$ mb) and for reactions at higher beam energies ($E_{\rm beam} \approx 800$ MeV/nucleon $\rightarrow \bar{\sigma} \approx 40$ mb). For comparison, we also present the ratio E_0 for the two cross sections, which results from simple counting arguments of neutrons and protons, or by assuming that protons and neutrons have the same density distribution in eq. (4.5),

$$E_0 = (N_{\rm A}N_{\rm B} - Z_{\rm A}Z_{\rm B})/(N_{\rm A}N_{\rm B} + Z_{\rm A}Z_{\rm B}) . \tag{4.11}$$

Our calculations confirm the finding of ref. [LM 88] that the ratio E is sensitive to the difference between proton and neutron density distribution and therefore the pion production is a useful tool for determining the size of the neutron-rich nuclei. However, in our results the effect is not quite as dramatic as claimed to be. We attribute this to the more realistic density distributions used in our calculations.

4.2. Pion energy spectra

In this section we study another aspect of exotic nuclei via pion energy spectra, namely the momentum distribution of nucleons inside these nuclei.

In the present exploratory study of pion spectra with exotic nuclei, we use a modified Fermi gas model. It was first used by Bertsch in the study of threshold pion production [Be 77]. The assumption is made that only the first collision of a nucleon pair can create a pion, and we further assume that pion reabsorption and the final-state Pauli blocking for the two colliding nucleons can be neglected. For the individual nuclei, we assume that the phase-space distribution function can be separated into coordinate and momentum parts. For the momentum space distribution of the colliding nuclei we use a simplified form of two homogeneously filled Fermi spheres, the centers of which are separated by the beam momentum

$$f_{AB}(\boldsymbol{p}) = \theta(p_{F_A} - |\boldsymbol{p}|)\, A + \theta(p_{F_B} - |\boldsymbol{p} - \boldsymbol{p}_{beam}|)\, B\,, \tag{4.12}$$

where p_{F_A} and p_{F_B} are the Fermi momenta of the projectile of mass A and target of mass B, respectively. We will use the Fermi momenta for carbon and ^{11}Li extracted from the experimental data, as we have discussed in the previous section.

Pion energy spectra in the reaction A + B can then be calculated as a sum of the pion energy distribution in each nucleon–nucleon collision with all possible momenta within the Fermi spheres

$$\left(\frac{d\sigma_\pi}{dE}\right)_{AB} = C\int\left(\frac{d\sigma_\pi}{dE}\right)_{NN}(s) f_A(\boldsymbol{p}_A) f_B(\boldsymbol{p}_B)\, d^3p_A\, d^3p_B\,, \tag{4.13}$$

where C is a constant coming from the integration over the impact parameter, which is irrelevant for the following discussions. s is the center-of-mass energy squared of the two colliding nucleons.

To calculate the pion energy distribution $(d\sigma_\pi/dE)_{NN}$ in each nucleon–nucleon collision, we assume that pion production is proceeding via the Δ resonance. The mass distribution of the Δ resonance is taken from Kitazoe et al. [Ki 86] and is given by

$$P(M_\Delta) = 0.25\Gamma^2(q)/[(M_\Delta - M_0)^2 + 0.25\Gamma^2(q)] \tag{4.14}$$

where $M_0 = 1232$ MeV, and the width $\Gamma(q)$ of the resonance is parametrized as

$$\Gamma(q) = 0.47q^3/[1 + 0.6(q/m_\pi)^2]m_\pi^2\,. \tag{4.15}$$

q is the momentum of the pion in the Δ rest frame.

The Δ is assumed to be produced isotropically in the nucleon–nucleon center-of-mass frame, and we also assume that the decay of the resonance has an isotropic angular distribution in the Δ rest frame. The decay of the resonance is then calculated using a Monte Carlo integration technique. This leads to a pion energy spectrum in the Δ rest frame which is finally Lorentz-transformed into the laboratory frame.

The integration in eq. (4.13) for calculating the pion spectra in the reaction A + B is performed with the Monte Carlo integration method. Our calculation therefore generates pairs of colliding nucleons from the projectile and the target, isospin quantum numbers are assigned to these nucleons according to the N/Z ratios of the projectile and the target. We use available experimental

data [VA 80; LM 70] for pion production cross sections in nucleon–nucleon collisions in all possible isospin channels.

One such calculation is performed for the reaction ^{11}Li + ^{12}C at various beam energies. To show the sensitivity of the pion energy spectra on the nucleon momentum distribution of the radioactive nuclei, we show in fig. 46 the π^- spectra calculated by using the core Fermi momentum and halo Fermi momentum for the ^{11}Li projectile, respectively. The solid histograms are calculated with $p_{F_A} = p_F(\text{halo}) = 38$ MeV/c and the dotted histograms are calculated with $p_{F_A} = p_F(\text{core}) = 158$ MeV/c. These two calculations simulate the situations that nucleons coming from ^{12}C collide with the halo and core nucleons of the ^{11}Li, respectively.

A strong sensitivity of the pion spectra on the nucleon momentum distribution can be seen, especially at beam energies smaller than about 300 MeV/nucleon. Moreover, the different slopes of the two curves signalling the different momentum distribution of the neutron halo from that of core nucleons can be seen experimentally. The presently available radioactive beam facilities can produce high quality ^{11}Li and ^{9}Li beams, the different neutron momentum distributions of core and halo neutrons in ^{11}Li would then show up as contributions to the pion energy spectra with different slopes in ^{11}Li and ^{9}Li induced reactions. We estimate that a beam of 10^5 ^{11}Li per second at a beam energy of 300 MeV/nucleon would produce about 10^4 pions per second. With this production rate, a high quality experiment using a pion spectrometer could be performed.

As can be seen from fig. 46, the difference in the slope of the pion spectra is not so obvious at beam energies above 600 MeV/nucleon. This can be understood by looking at the distribution of the center-of-mass energy squared s of the two colliding nucleons in the reaction A + B,

$$F(s) = \int f_A(\boldsymbol{p}_A) f_B(\boldsymbol{p}_B - \boldsymbol{p}_{\text{beam}})\, \delta(s - 2m_n^2 - 2E_A E_B + 2\boldsymbol{p}_A \cdot \boldsymbol{p}_B)\, d^3p_A\, d^3p_B\,,$$

where we take on-shell nucleons so that $E_i = (p_i^2 + m_n^2)^{1/2}$ for i = A, B.

In fig. 47 we present the distribution of $s^{1/2} - (2m_n + m_\pi)$, which is the maximum of the pion kinetic energy in the center of mass of the two colliding nucleons. The calculation is done for the

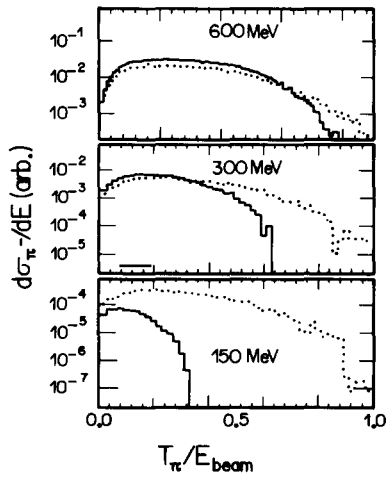

Fig. 46. Pion kinetic energy spectra in the reaction ^{11}Li + ^{12}C at beam energies of 600, 300 and 150 MeV/nucleon. The solid lines are calculated with $p_{FA} = p_F$ (halo) and the dotted lines are calculated with $p_{FA} = p_F$ (core).

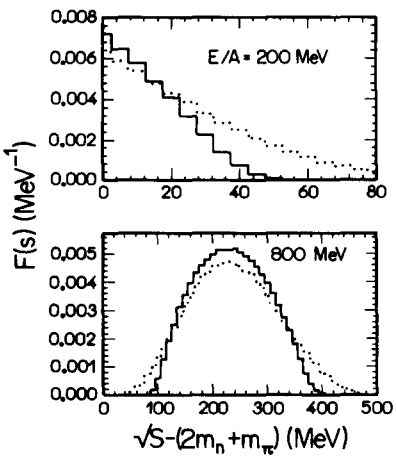

Fig. 47. Distribution of the center-of-mass energy above pion-production threshold for pairs of colliding nucleons in the reaction ^{11}Li + ^{12}C. The solid and dotted lines are calculated under the same conditions as in fig. 46.

reaction ^{11}Li + ^{12}C at beam energies of 200 MeV/nucleon and 800 MeV/nucleon. Again the solid histograms are the results using $p_{F_A} = p_F$(halo) and the dotted ones using $p_{F_A} = p_F$(core). The effect of different internal momentum distributions is obvious at lower energies; as the beam energy gets much larger than the Fermi energy, the effect gets less obvious.

In summary, we have studied both the coordinate and momentum space structure of the exotic nuclei via pion production. Through a Glauber-type multiple-collision model calculation for the inclusive π^+ and π^- production cross sections, implemented with the shell-model calculated densities for neutrons and protons as well as the nucleon momentum-averaged nucleon–nucleon cross sections, it is shown that the ratio of the π^+ and π^- production cross section is sensitive to the difference between the proton and neutron densities. This ratio would be a useful tool for determining the size of the exotic nuclei.

Within a modified Fermi gas model for the momentum distribution and assuming that the pion production proceeds via Δ resonance as well as using the available experimental data for pion productions in nucleon–nucleon collisions, we find that pion energy spectra are strongly sensitive to the internal momentum distribution of the exotic nuclei. We further discussed a possible experiment to determine the momentum distribution of the neutron halo via pion energy spectra.

Pion production with radioactive nuclei provides a complementary way for further determining the properties of the exotic nuclei. Similar effects can be obtained through the study of hard photons. Here, final-state interactions are completely negligible in contrast to the pion production case. This makes the γ potentially "clearer" to study than the π.

5. Near-barrier fusion of exotic nuclei

Recently, the low-energy fusion of radioactive beams, such as ^{11}Li, with heavy-target nuclei has been discussed [IMC 89; Hu 91a, b; DD 92]. The principal motivation is twofold: (i) the enhancement of the fusion cross section σ_f that arises from the existence of the halo neutrons can be used to further understand these exotic nuclei, and (ii) the relevance of such studies to the potential production of superheavy cold compound nuclei, using heavier exotic nuclei such as ^{60}Ca or ^{70}Fe, with reasonably measurable cross sections.

In the calculations made so far, two features of the halo are taken into account: the lowering of the static Coulomb barrier and the coupling of the entrance channel to the low-lying soft giant dipole resonance (SGD) (the pygmy resonance). Both of these effects lead to an enhanced fusion cross section.

In this chapter we discuss the near-barrier fusion of exotic nuclei with heavy spherical and deformed target. We discuss the effect of the coupling to the pygmy resonance as well as to the breakup channel.

The existence of the pygmy resonance at about 1.2 MeV has recently been firmly established through the study of the double charge exchange reaction ^{11}B(π^-, π^+)^{11}Li [Ko 91]. One anticipates, on general grounds, that this state has a large width due to the very low binding energy of the dineutron ($\sim$0.2 MeV). Thus it is of great importance in any fusion calculation to consider the finite lifetime of the pygmy resonance. This tends to hinder the fusion process, in opposition to the enhancement factors already reported. The purpose of this chapter is to calculate the fusion cross section which takes into account the above effect by coupling the pygmy resonance to the breakup channel. As fig. 48 shows, when a neutron-rich projectile approaches a heavy deformed target nucleus, then within the soft giant dipole picture of section 1.2, the interaction induces a dipole oscillation of the excess neutrons with respect to the projectile core. This allows a closer nuclear

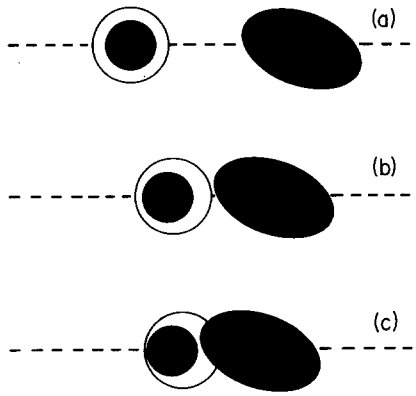

Fig. 48. When a neutron-rich projectile approaches a heavy deformed nucleus, the interaction sets in a dipole oscillation of the excess neutron with respect to the core, allowing a closer nuclear contact with target.

contact with the target, increasing the fusion probability. On the other hand, within the cluster picture, also discussed in section 1.2, the greater probability of breakup could easily result in a lowering of the fusion cross section. Therefore the thrust of this chapter is to take into account both cluster and SGD features of neutron-rich nuclei in the calculation of the near-barrier fusion cross section.

5.1. *Effects of the coupling to the pygmy resonance*

In a coupled channel description of a heavy-ion reaction, the fusion cross section can be calculated from the total reaction cross section as [HRB 91]

$$\sigma_f = \sigma_R - \sigma_D \,, \tag{5.1}$$

where σ_D is the direct reaction cross section and σ_R is given by

$$\sigma_R = (k/E)\langle \Psi_k^{(+)} | -\mathrm{Im}\, V | \Psi_k^{(+)} \rangle \,, \tag{5.2}$$

where $\langle r | \Psi_k^{(+)} \rangle$ is the wave function that describes the elastic scattering and V is the optical potential that generates it. It can be shown [Hu 84; HRB 91] that the cross section σ_f (eq. 5.1) can be written in the form

$$\sigma_f = \frac{k}{E} \sum_i \langle \Psi_{k_i}^{(+)} | -\mathrm{Im}\, V_i^0 | \Psi_{k_i}^{(+)} \rangle \,, \tag{5.3}$$

where V_i^0 is the bare optical potential in channel i (no channel coupling) and $| \Psi_{k_i}^{(+)} \rangle$ is the exact scattering state in that channel. Equation (5.3) has been used by several authors to calculate σ_f using coupled-channels codes [DLW 83]. Other models based on this equation but with the further assumption of infinite absorption once the barrier is penetrated have also been developed [LR 84]. Here we generalize the second class of models by incorporating the effect of the breakup channel (included in $| \Psi_{k_i}^{(+)} \rangle$).

To be more specific, we deal here with a case involving the coupling of the elastic channel to a resonant state in the projectile. If this resonant state is approximated by an excited state whose width is very small, then σ_f can be written as (ignoring the excitation energy of the state) [LR 84]

$$\sigma_f = \tfrac{1}{2}[\sigma_f^0(E+F) + \sigma_f^0(E-F)] , \tag{5.4}$$

where σ_f^0 is the one-channel fusion cross section, F is the channel coupling potential evaluated at the barrier radius, and E is the collision energy in the c.m. frame. One possible way to take into account the effect of the nonzero width of the resonance is to consider F in eq. (5.4) to be the maximum value of a Lorentzian strength whose form is

$$\mathscr{F}' = \tfrac{1}{4}\Gamma^2 \mathscr{F}'_0/[(Q-1.2)^2 + \tfrac{1}{4}\Gamma^2] . \tag{5.5}$$

Thus, effectively, the effect of the coupling is reduced.

5.2. *Effects of the coupling to the breakup channel*

To include the breakup channel coupling effect, in eq. (5.4), namely the nonzero width of the excited state, it is convenient first to express the cross section as a sum of partial wave contributions

$$\sigma_f^0 = \frac{\pi}{k^2}\sum_{l=0}^{\infty}(2l+1)\,T_l^f , \qquad T_l^f(E) = \left\{1 + \exp\left[\frac{2\pi}{\hbar\omega}\left(V_B + \frac{\hbar^2 l(l+1)}{2\mu R_B^2} - E\right)\right]\right\}^{-1} . \tag{5.6}$$

Above, R_B and V_B are the Coulomb barrier radius and height, respectively. When incorporating the breakup channel coupling effect, the partial fusion probability, T_l^f, has to be multiplied by the breakup survival probability, $1 - T_l^{bu}$. Thus

$$\sigma_f^{0b} = \frac{\pi}{k^2}\sum_{l=0}^{\infty}(2l+1)(1-T_l^{bu})\,T_l^f . \tag{5.7}$$

And finally,

$$\sigma_f = \frac{\pi}{2k^2}\left(\sum_{l=0}^{\infty}(2l+1)(1-T_l^{bu})\,T_l^f(E+F) + \sum_{l=0}^{\infty}(2l+1)(1-T_l^{bu})\,T_l^f(E-F)\right)$$

$$= \tfrac{1}{2}[\sigma_f^{0b}(E+F) + \sigma_f^{0b}(E-F)] . \tag{5.8}$$

Here the Coulomb breakup does not contribute since it is significant only at l larger than those for which fusion is relevant. The nuclear breakup transmission factor, T_l^{bu}, has been recently calculated for several radioactive systems [CDH 91a,b]. The major conclusion of these studies is that the dynamic polarization potential which enters in the evaluation of T_l^{bu}, via

$$T_l^{bu} = 1 - \exp\left(-2\int_{\rho_0}^{\infty}\frac{\operatorname{Im} V_{pol}/E}{[1-(2\eta/\rho)-l(l+1)/\rho^2]^{1/2}}\,d\rho\right) \tag{5.9}$$

is very sensitive to the binding energy of the breakup cluster. In eq. (5.9) η is the Sommerfeld parameter and ρ_0 is the distance of closest approach, multiplied by the wave number k, obtained from $1 - 2\eta/\rho_0 - l(l+1)/\rho_0^2 = 0$. A closed-form expression for $T_l^{\rm bu}$ was derived in ref. [CDH 91b] and it reads

$$T_l^{\rm bu} = 1 - \exp\left[-(4\mathscr{F}_0^2/E^2)\,|S_l^{(1)}|\,I_l^2(\eta, s)\right], \tag{5.10}$$

where $\mathscr{F}_0$ is a coupling strength factor of eq. (3.37b), which was found to be 4.859 eV for ^{11}Li + ^{208}Pb, $|S_l^{(1)}|$ is the modulus of the optical S-matrix in the breakup channel and $I_l(\eta, s)$ is a Coulomb radial integral evaluated and discussed in ref. [CDH 91b] (see section 3.3). The sensitivity of $V_{\rm pol}$ and $T_l^{\rm bu}$ to the binding energy of the dineutron in ^{11}Li resides in the l-dependence of $I_l(\eta, s)$.

In ref. [Fi 91], the breakup effect on near-barrier fusion of several light heavy-ion systems has been extensively studied. In particular the data on the systems ^{9}Be + ^{29}Si, ^{11}B + ^{27}Al, ^{12}C + ^{24}Mg and ^{19}F + ^{19}F have been investigated. The greater breakup probability of several of the participating nuclei was found to be responsible for the correspondingly smaller fusion cross section, calculated according to eq. (5.7). This comparison supports the validity of the above discussed model.

5.3. *Application to the fusion of ^{11}Li with ^{208}Pb and ^{228}U at near-barrier energies*

In the following, we apply the results of the previous section to the fusion of ^{11}Li with very heavy ions [Hu 92]. We use the fusion calculation of Takigawa and Sagawa [TS 91] as a background for the study of the effect of the coupling to the breakup channel. We take the height of the Coulomb barrier ($V_{\rm B} = 26$ MeV) its radius ($R_{\rm B} = 11.1$ fm) and curvature ($\hbar\omega = 3$ MeV) from fig. 1 of ref. [TS 91] and use these parameters in the Hill–Wheeler transmission coefficients of eq. (5.6). The strength F was adjusted to reproduce the values of σ_f of ref. [TS 91]. We found $F \sim +3.0$ MeV. The breakup effect was then investigated through the modified fusion cross section of eqs. (5.8) and (5.10), taking $|S_l^{(1)}| = [1 - T_l^{\rm f}(E - 0.2)]^{1/2}$. The result of our calculation is shown in fig. 49. It is clear that the inclusion of the breakup coupling and thus the lifetime of the pygmy resonance, reduces σ_f by as much as a factor of 100 at energies slightly below the barrier. More important is the fact that the breakup of the projectile renders the fusion cross section *lower* than the one-dimensional calculation at energies extending from slightly below the barrier to energies above the barrier (24 MeV $< E <$ 45 MeV). At energies less than 24 MeV the enhancement sets in. The increase of the enhancement with increasing E^{-1} is, however, much slower than the case without breakup, eq. (5.4). Only at energies $E \lesssim 10$ MeV, does the breakup effect subside completely, letting the pygmy resonance act as a complete vibrational enhancer.

Figure 50 exhibits more clearly the above features through the behaviour of the enhancement factor ε, defined as the ratio of the fusion cross section to the one-dimensional cross section σ_f^0. The breakup effect is contained in the interval 10 MeV $< E <$ 45 MeV. Further, there is a sharp dip at the barrier. This dip is easily understood. At energies above the barrier, the nuclear breakup process inhibits fusion. This inhibition becomes less effective as the energy approaches the barrier, which acts as a natural threshold. At sub-barrier energies, the increase in the distance of closest approach leads to a further reduction in the breakup effects. These striking features arising from the halo should be easy to verify experimentally. The saturation value of ε is 250 and it represents simply the value of $\frac{1}{2}\exp(2\pi/\hbar\omega F)$ [eq. (5.6) at the energy $E - F$], which is attained at much lower energies ($\sim$ 10 MeV) than predicted by Takigawa and Sagawa [TS 91].

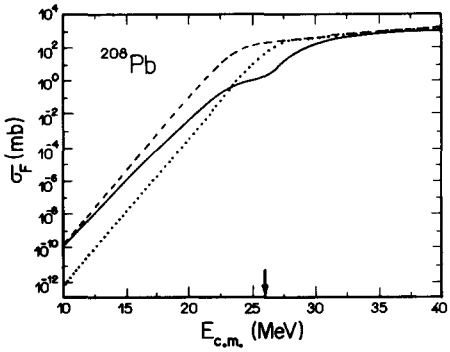

Fig. 49. Excitation function for the fusion cross section of ^{11}Li + ^{208}Pb. The dotted curve is the one-dimensional Hill–Wheeler cross section (eq. 5.6), the dashed curve is the pygmy resonance enhanced cross section (eq. 5.4) and the full curve represents the result with inclusion of the breakup coupling (eq. 5.8) (see text for details).

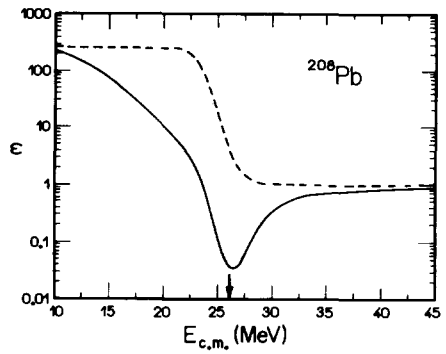

Fig. 50. The enhancement factor ε versus $E_{c.m.}$ for ^{11}Li + Pb. The dashed curve is eq. (5.4)/eq. (5.6) while the full curve represents eq. (5.8)/eq. (5.6).

We have repeated the above calculation for the deformed nucleus ^{238}U. Here the enhancement of σ_f arises from both the coupling to the pygmy resonance of the projectile and the coupling to the states of the target rotor. Taking only the 0^+ and 2^+ states of ^{238}U into consideration, the fusion formula reads [Hu 91b] (the sudden limit is assumed)

$$\sigma_f = \tfrac{1}{2}\{0.562[\sigma_f^0(E + F + 0.73\beta_2 f(R_B)) + \sigma_f^0(E - F + 0.73\beta_2 f(R_B))] + 0.438[\sigma_f^0(E + F - 1.37\beta_2 f(R_B)) + \sigma_f^0(E - F - 1.37\beta_2 f(R_B))]\}\,, \tag{5.11}$$

where $f(R_B)$ is the rotational coupling form factor given approximately by

$$f(R_B) = (1/\sqrt{4\pi})\, V_B\,(R_2/R_B)\,(1 - \tfrac{3}{5}(R_2/R_B))\,. \tag{5.12}$$

In eqs. (5.11) and (5.12) R_2 is the radius of ^{238}U (7.4 fm), β_2 is the deformation parameter ($\beta_2 \simeq 0.27$), we estimate V_B to be about 29 MeV. One thus gets $f(R_B) = 3.3$ MeV.

In fig. 51 we present the fusion cross sections calculated according to eq. (5.9) (one-dimensional barrier penetration model, dashed line), to eq. (5.11) (pygmy resonance vibration and target rotation coupling model, dotted line) and with the inclusion of the breakup survival probability in eq. (5.11), obtained by replacing σ_f^0 by σ_f^{0b} (full curve). We find here a fusion behaviour similar to that of the ^{11}Li + ^{208}Pb system except that the enhancement is larger by a factor of 11. The corresponding enhancement factors are shown in fig. 52, which shows very similar behaviour to fig. 50. The saturation value of ε is 1000, which is attained at about $E = 13$ MeV. Again one sees the sharp dip of ε at the barrier energy (29 MeV).

In this section, we have calculated the influence of the nonzero width of the pygmy resonance on the fusion of ^{11}Li with heavy spherical and deformed nuclei at close-to-barrier energies. This is accomplished by taking into account in the multi-dimensional fusion calculation, the effect of the breakup channel $^{11}\text{Li} \rightarrow {}^{9}\text{Li} + 2n$. The usual vibrational and vibrational + target rotational enhancement of the sub-barrier fusion cross section is appreciably reduced. Further, the enhancement factor ε is found to exhibit nontrivial structure around the barrier. This is clearly related to

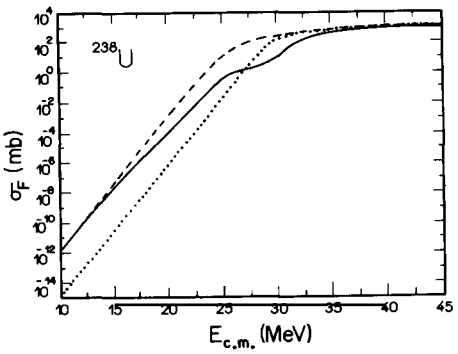

Fig. 51. Same as fig. 49 for ^{11}Li + ^{238}U (dotted curve). The dashed curve is the pygmy resonance + target rotation enhanced cross section (eq. 5.11). The full curve includes the effect of the ^{11}Li breakup on eq. (5.11).

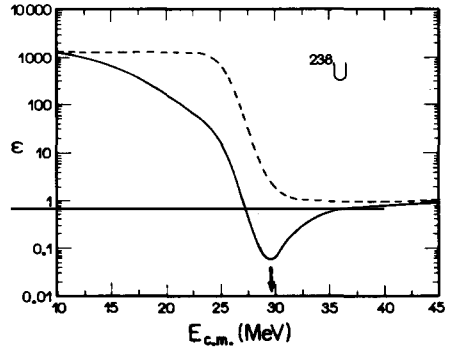

Fig. 52. The enhancement factor ε versus $E_{c.m.}$ for ^{11}Li + ^{238}U. The dashed curve is eq. (5.8)/eq. (5.6) while the full curve includes the breakup effect. See text for details.

the halo neutrons in ^{11}Li and should be easily verified experimentally. Similar effects should be present in exotic B- and Be-induced fusion reaction.

Before ending, we should mention that the above findings are quite relevant to the discussion of using radioactive beams to produce superheavy elements. In ref. [Hu 91b] the sub-barrier fusion cross section for ^{70}Fe + ^{208}Pb was calculated including only the effects of the pygmy oscillation, and it was found that the enhancement was quite great. Similar conclusions were reached by ref. [DD 92] for the system ^{54}Ca + ^{144}Sm. It is obvious that these calculated enhancements are great overestimates in view of the easily breakable nature of these loosely bound nuclei. Further, considerations of extra–extra push limitations of fusion, recently taken into account by ref. [Ag 92] clearly points to a much more modest enhancement.

6. Nuclear astrophysics and exotic nuclei

6.1. Coulomb dissociation experiments

It is well known [Fo 84], that a variety of stellar environments are so hot and dense that the nuclear reaction rates are comparable with natural decay processes. These conditions characterize nuclear burning in, for example, cataclysmic binaries, accreting neutron stars, and supernovae, all of which are important nucleosynthetic sources. Of special interest in this context is the radiative capture reaction which is one of the most important in the formation of various elements in the universe (for a review see, e.g., ref. [RB 90]). An example of such reaction is ^{7}Be(p, γ)^{8}B, the decay of which is believed to yield about 70–80% of the neutrinos of our sun that are detectable using the ^{37}Cl(ν, e$^-$)^{37}Ar reaction. Although there are some experiments on proton-capture reactions on ^{7}Be, which has a half-life of 54 days, disagreement among the results are found [Ba 80; Ba 83; BS 86]. Thus, an independent measurement, based on alternative techniques, would be useful. Such statement is valid for other radiative capture reactions of interest in astrophysics.

For example, recently, an alternative mechanism for the primordial nucleosynthesis of intermediate-mass nuclei ($12 \leq A \leq 28$) has been proposed [Ap 87; MF 88; Ma 90]. In this scheme, heavier nuclei are formed via neutron capture or proton and alpha chains. The important reactions

in this scenario consist of the following:

$$^{1}H(n,\gamma)^{2}H(n,\gamma)^{3}H(d,n)^{4}He(^{3}H,\gamma)^{7}Li(n,\gamma)^{8}Li(\alpha,n)^{11}B(n,\gamma)^{12}B$$

$$^{12}B(\beta,\bar{\nu})^{12}C(n,\gamma)^{13}C(n,\gamma)^{14}C(n,\gamma)^{15}C \ldots \tag{6.1}$$

In addition, there is an important branch which turns the reaction flow back to the lighter elements,

$$^{8}Li(n,\gamma)^{9}Li(\beta^{-},\nu)^{9}Be(p,\alpha)^{6}Li\,. \tag{6.2}$$

Of the above reactions, it is important to determine the following neutron-capture cross sections:

$$^{7}Li(n,\gamma)^{8}Li(n,\gamma)^{9}Li\,; \qquad ^{12}C(n,\gamma)^{13}C \text{ and } ^{14}C(n,\gamma)^{15}C\,. \tag{6.3a, b}$$

The $^{8}Li(n,\gamma)^{9}Li$ reaction is important because it may compete strongly with the α-capture reaction $^{8}Li(\alpha,n)^{11}B$, thus reducing the predicted yields of $A \geq 12$ isotopes. In fact, there could be as much as a 50% reduction in $A \geq 12$ isotopes, depending on the cross section for the $^{8}Li(n,\gamma)^{9}Li$ reaction [WSK 89]. It may be impossible to ever have a ^{8}Li target due to its short half-life (838 ms) so the cross section for the capture reaction may never be measured.

Likewise, the subsequent reactions in the above chain involving ^{14}C and ^{15}C provide an alternative route to the production of heavy elements. For example, Kajino et al. [KMF 90] have found that, depending on the value of the cross section used for the reaction $^{14}C(n,\gamma)^{15}C$, the sequence of carbon-capture reactions and β decays can provide the main route to the synthesis of heavy elements. This contradicts other nucleosynthesis calculations, where the reaction $^{14}C(\alpha,\gamma)^{18}O$ is considered the primary means through which heavy elements are synthesized. However, estimates of the ^{14}C capture cross section vary significantly. Only an upper limit to the measured thermal neutron-capture cross section currently exists, and extrapolating this to a neutron energy of 30 keV with the $1/\sqrt{E}$ law implies an upper limit of ≤ 1 nb. Calculations which consider only ^{14}C neutron capture followed by E2 transitions to the $5/2^{+}$ state of ^{15}C agree with this value. However, Kajino et al. also include the E1 transitions to the ^{15}C ground state, and they calculate a cross section of 0.1 mb, an increase by a factor of 10^{5}. If the cross section is indeed this high, then this reaction could compete with the $^{14}C(\alpha,\gamma)^{15}C$ reaction as the primary path to heavy element synthesis [KMF 90]. Considering the large discrepancy in theoretical estimates for this cross section (5 orders of magnitude), a measurement is warranted. As with the $^{8}Li(n,\gamma)^{9}Li$ reaction, to measure the $^{14}C(n,\gamma)^{15}C$ reaction in the forward direction would be very difficult, if not impossible.

As we have seen in previous sections, reactions with radioactive secondary beams have provided unique opportunities to study the nuclear structure of exotic nuclei, far from the stability line. Reactions of nuclei with half-lifes of the order of milliseconds are now possible to study experimentally. In this section is shown that, besides the possibilitiy to study entirely new phenomena, unobservable with current methods, radioactive beams can give direct information on the astrophysical S-factors for radiative capture reactions leading to the formation of unstable nuclei. This possibility arises because of the huge Coulomb dissociation cross sections of radioactive projectiles, due to their low binding energy.

The Coulomb dissociation method was proposed and shown by Baur, Bertulani and Rebel [BBR 86] as an important tool to extract useful information on radiative capture cross sections of interest in astrophysics. The first experiments done to test this method for the reactions $\alpha(t, \gamma)^7Li$, $\alpha(d, \gamma)^6Li$ and $p(^{13}N, \gamma)^{14}O$ have been encouraging [Ut 90a; Ki 89, 91; Mo 91]. Reactions with high-energy release, like $^{12}C(\alpha, \gamma)^{16}O$, can also be studied in this way. Nonetheless, one has to rely on precise coincidence measurements of the angular and energy distributions of fragments b and c. Another disadvantage of this method is that one has no control on the final-state interactions of, e.g., the influence of the Coulomb and nuclear fields of the target after the breakup.

The Coulomb dissociation method works as follows. The Coulomb dissociation cross section for the reaction a + A → b + c + A is given by [BB 88c]

$$\sigma_{CD} = \sum_{\pi\lambda} \int n_{\pi\lambda}(\varepsilon)\, \sigma_\gamma^{\pi\lambda}(\varepsilon) \frac{d\varepsilon}{\varepsilon} \tag{6.4}$$

where $\sigma_\gamma^{\pi\lambda}(\varepsilon)$ is the photo-disintegration cross section γ + a → b + c, with the photon energy ε, and multipolarity π = E (electric) or M (magnetic), and $\lambda = 1, 2, \ldots$ (order). The photo-disintegration cross section is related to the radiative capture cross section through the detailed balance theorem

$$\sigma(\gamma + a \to b + c) = \sum_{\pi\lambda} \sigma_\gamma^{\pi\lambda}(\gamma + a \to b + c) = \frac{(2J_b + 1)(2J_c + 1)}{2(2J_a + 1)} \frac{k^2}{k_\gamma^2} \sigma(b + c \to a + \gamma)\,, \tag{6.5}$$

where $k^2 = 2\mu E/\hbar^2$, E is the center-of-mass energy of the relative motion of the b + c system, μ is the reduced mass of b + c, $k_\gamma = \varepsilon/\hbar c = (E + Q)/\hbar c$, and Q is the energy release in the radiative capture. The radiative capture cross section is usually written in terms of the astrophysical S-factor as

$$\sigma(B + c \to a + \gamma) = [S(E)/E] \exp[-2\pi\eta(E)]\,, \quad \eta = Z_b Z_c e^2/\hbar v\,, \tag{6.6}$$

where $v = \sqrt{2\mu E}$. This definition factors out the steep increase of the radiative capture cross sections at low relative energies [RB 90].

As indicated in eq. (6.5), the radiative capture cross section is a sum over all multipolarities. In most cases, a multipolarity of one (or two) dominates the process. This also occurs with the Coulomb-induced breakup cross section given by eq. (6.4), depending on the function $n_{\pi\lambda}(\varepsilon)$. These functions are interpreted as the number of equivalent (virtual) photons, provided by the Coulomb field of nucleus A, incident on nucleus a. They can be calculated for all bombarding energies with good accuracy, as was shown in ref. [AB 89]. In very high-energy collisions, simple analytical formulas were obtained [BB 88c]. Also, for all multipolarities, $n_{\pi\lambda}(\varepsilon)$ decreases rapidly with ε, thus enhancing the lower-energy part of the photo-disintegration cross section, which enters eq. (6.4).

Formula (6.4) has the same structure if one measures differential cross sections, instead of total ones. Only the quantities $n_{\pi\lambda}$ are replaced by similar ones, which depend on differentiated variable (e.g., $\theta_{c.m.}$, ε, etc.). Therefore, a direct relationship always exists between the measurement and the photo-disintegration, or the radiative capture cross section, respectively.

The simplest measurements take advantage of resonances that may exist for a particular energy E. In this case, the aim is to obtain the total strength below the resonance, its width, etc. The first successful experiment along these lines was done by Motobayashi et al. [Mo 91]. In this experiment

the cross section of the Coulomb dissociation reaction ^{208}Pb(^{14}O, ^{13}Np)^{208}Pb was measured at E_{lab} = 87.5 MeV/nucleon. The aim was to determine the radiative width Γ_γ of the 1^- state in ^{14}O at ε = 5.17 MeV, which dominates the radiative capture process ^{13}N(p, γ)^{14}O, a key reaction in the hot CNO cycle of hydrogen burning in stars. In fact, this reaction competes with the β^+ decay of ^{13}N and determines the conditions for starting the hot CNO cycle rather than the regular CNO cycle. This transition is expected to take place in various astrophysical circumstances, such as supermassive stars, novae, supernovae outburst [WW 81] or at the surface of neutron stars [FHM 81].

The result of this experiment is shown in fig. 53 where the angular distribution of ^{14}O excited to its 1^- state is shown. This state was identified by its decay products p + ^{13}N. Since coupling effects or multi-step contributions are negligible, a one-step excitation model (see, e.g., ref. [AB 91]) is enough to describe the scattering data. In this model the only parameter needed to reproduce the data is a deformation parameter $\beta_{N,C}$ which determines the strength of the excitation. The contribution from the nuclear breakup can be estimated by assuming a simple collective vibration mode with $\beta_N = \beta_C$, where β_N and β_C denote the nuclear and Coulomb deformation parameters, respectively. At forward angles of $\theta \leq 5°$, a coherent sum of the nuclear and Coulomb amplitudes is only different by 5% on average from the pure Coulomb dissociation cross sections. The best fit to the experimental data was obtained with a deformation parameter β_C = 0.046, corresponding to a radiative width $\Gamma_\gamma = 3.1 \pm 0.6$ eV. This error is the smallest of the three existing measurements, indicating high experimental efficiency of the Coulomb dissociation method. The other experiments are the results of branching-ratio measurements of Fernandez et al. (2.7 ± 1.3 eV) [FAG 89] and the one of Aguer et al. (7.6 ± 3.8 eV) [Ag 89].

Nonresonant reactions are more difficult to analyse via the Coulomb dissociation method. In order to determine the radiative capture cross section (6.6) an accurate measurement of the relative energy E of the fragments has to be made after the breakup. But "post-acceleration" effects (i.e., the additional acceleration of the fragments by the Coulomb field of the target) may prevent a direct association between the measured energy and that originated from the direct breakup mechanism. Nonetheless, for certain cases the method has been shown to work [BH 91a].

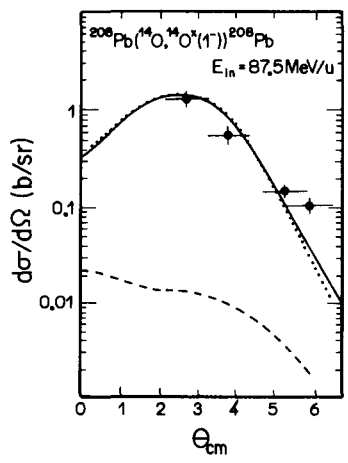

Fig. 53. Experimental and calculated angular distributions for the reactions ^{208}Pb(^{14}O, ^{13}Np)^{208}Pb exciting the 1^- state of ^{14}O. The solid curves are obtained by the coherent sum of the nuclear and Coulomb excitation amplitudes assuming Γ_γ = 3.1 eV for ^{14}O(1^-). The dashed and dotted curves represent the nuclear and Coulomb breakup contributions, respectively, to the ^{208}Pb(^{14}O, ^{13}Np)^{208}Pb reaction.

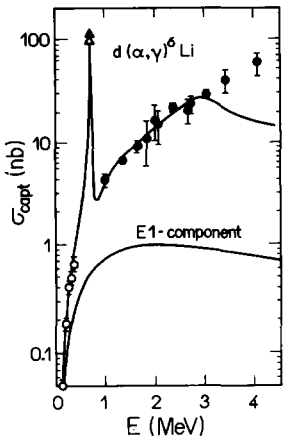

Fig. 54. Cross section for the d(α, γ)^{6}Li capture reaction. The low-energy data (open circles) were obtained by means of the Coulomb dissociation method [Ki 91] and added to the graph of ref. [Ro 81].

Successful experiments for the study of α(d, γ)^{6}Li and α(t, γ)^{7}Li by the Coulomb dissociation method has been performed (see, e.g., refs. [Ut 90a; Ki 91]).

The reaction of the Coulomb breaking-up of ^{6}Li into α-particle and deuteron fragments is especially suited for the use of the method, since the identical charge-to-mass ratio of the fragments minimizes the post-acceleration effects. The production of Li isotopes through ^{4}He(t, γ)^{7}Li and ^{4}He(d, γ)^{6}Li fusion reactions at temperatures corresponding to energies of about 300 keV is an important clue of the nucleosynthesis in the primordial fireball [Sc 85; SW 77]. The ^{4}He(d, γ)^{6}Li cross section is unknown at these energies, and the present conclusion that ^{7}Li is produced in the big-bang nucleosynthesis, but that ^{6}Li, however, is produced predominantly in spallation reactions, is based on a purely theoretical extrapolation of the cross section [Au 81].

In the experiment of Kiener [Ki 91] a very elaborate measurement of the triple-differential laboratory cross sections $d^3\sigma/d\Omega_\alpha d\Omega_d dE_{\alpha d}$ was done. Analogous to the ideas behind eqs. (6.4)–(6.6) this measurement can be related to the radiative capture cross section ^{4}He(d, γ)^{6}Li. In order to display the experimental progress due to the use of the Coulomb dissociation method, their data (with $E \geq 100$ keV) are plotted (open circles) in fig. 54 together with the previous (higher-energy) results of the standard experimental approach [Ro 81]. These results can be considered as an experimental confirmation of theoretical conclusions on the capture cross section at astrophysical energies.

The examples displayed in figs. 53 and 54, with their applications, give strong support to the Coulomb dissociation method as an alternative tool to access information on the radiative capture cross section of astrophysical interest. While some of these reactions can be studied in a standard capture experiment, the ones involving radioactive targets, like those of eqs. (6.3a, b) could be better studied by using the Coulomb dissociation method. The most promising cases are the reactions proceeding through resonances, and for which no available data exist due to the difficulty of using radioactive targets.

6.2. Direct measurements

Most nuclides with $A \gtrsim 70$ are synthesized by neutron capture. The s-process describes neutron capture over slow time scale compared with typical beta-decay lifetimes near the line of stability,

and thus leads to the formation of a continuous chain of stable heavy elements from the iron group to ^{209}Bi. The r-process, on the other hand, corresponds to neutron capture on a time scale which is rapid compared with β-decay lifetimes.

In an explosive astrophysical environment the neutron densities can become so high that successive neutron captures can occur out to nuclei far from stability. Furthermore, the temperatures become so high ($T \sim 3 \times 10^8$ K) that the Boltzmann population of nuclear excited states can lead to dramatic changes of the neutron-capture and β-decay rates. In this context there is a class of reactions which one thinks [Ma 86] are important quantities to improve the regime of input to the s-process in such environments. Important unstable nuclei for which the neutron-capture cross section has not been measured are, e.g., ^{79}Se, ^{85}Kr, ^{107}Pd, ^{147}Pm, ^{151}Sm, ^{166}Ho, ^{186}Re, ^{192}Ir and ^{205}Pb.

The astrophysical site for the r-process is still not known. There are two fundamental time scales which are basic input data to this process. One is just how high the neutron density must be to reproduce the r-process abundances. The other is that the neutron density must remain high in order to produce the actinides (which cannot be produced by the s-process due to α-decay at ^{210}Bi). This quantity depends on the sum of the neutron-capture and β-decay lifetimes as one moves away from stability. The r-process must live enough for nuclei to capture far from stability, and then for beta to decay up to the mass numbers of the actinides. Before the astrophysical site for the r-process can be determined, more refined determinations of neutron-capture cross sections and β-decay rates are desirable.

Anytime there is thermonuclear hydrogen burning, there is a possibility for proton reactions on unstable nuclei. A well known example is the reaction ^{7}Be(p, γ)^{8}B in the sun. Other examples are the ^{22}Na(p, γ)^{23}Mg reaction in the Ne–Na cycle, and the reactions of ^{26}Al in the Mg–Al cycle. When the temperatures are high, other reaction rates also become important. For $T \gtrsim 2 \times 10^8$ K the waiting point for the normal hydrogen-burning CNO-cycle shifts [MD 84] from ^{14}N to ^{13}N, and then, via the ^{13}N(p, γ)^{14}O reaction, it shifts to the production of ^{14}O and ^{15}O. This is the hot (beta-limited) CNO cycle, which is particularly significant in the evolution of supermassive ($M > 10^4 M_{sun}$) stars. This hot hydrogen-burning scenario can be studied via the Coulomb dissociation method, as discussed in section 6.1, or by producing a beam of radioactive heavy ions to be focussed onto a target of hydrogen or ^{4}He.

The reaction ^{8}Li(α, n)^{11}B is critical in predicting the abundances of ^{11}B and heavier nuclei in the standard (homogeneous) model (SM) [WFF 67; SW 77; Wa 84] or in the inhomogeneous models (IM) [AHS 87, 88; AFM 87; Ma 90; KB 90], as ^{11}B is the nuclide through which most heavier nuclides must pass, and that reaction apparently regulates the dominant pathway by which ^{11}B is made [KB 90]. Observation of this reaction, however, is complicated by the 840.3 ms half-life [Sa 90] of ^{8}Li. A recent measurement [Pa 90] of the inverse reaction ^{11}B(n, α)^{8}Li gives the ground-state–ground-state cross section for ^{8}Li(α, n)^{11}B. However, several ^{11}B excited states can be populated in ^{8}Li(α, n)^{11}B, so inference of the cross section of interest from measurement of the inverse reaction may underestimate the actual value by a large factor. This statement also applies for the Coulomb dissociation method. The use of inverse (or nondirect) measurements has to be analysed carefully case by case.

Of course, the best possible measurement is the direct one. For the reaction ^{8}Li(α, n)^{11}B a direct measurement has been recently reported using a ^{8}Li radioactive beam [Bo 92]. Their results are shown in fig. 55. Also indicated in that figure is the ground-state–ground-state excitation function inferred from the study of the inverse reaction [Pa 90]; it can be seen that the cross section to all possible ^{11}B states exceeds that to just the ground state by a fairly constant factor of about 5 for the data shown. Since all the nuclides heavier than 11 amu pass through ^{11}B on their way to higher

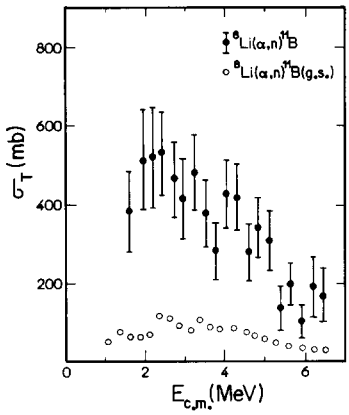

Fig. 55. Total cross section for the ^{8}Li(α, n)^{11}B reaction as a function of the center-of-mass energy. The points with error bars are from ref. [Bo 92]. The open circles are a sampling of the data of ref. [Pa 90] for the cross section to just ^{11}B (g.s.).

masses, the heavier-element abundances might thus be expected to increase with this reaction rate, provided β-decay of ^{8}Li is the dominant ^{8}Li destruction mechanism.

7. Momentum and angular distributions in exotic beam induced reactions

7.1. Momentum distribution

Fragmentation reactions with secondary beams of radioactive nuclei have shown that the total reaction cross section and the transverse momentum distribution of the fragments are sensitive to the separation energy of the last neutrons and to the size of the density profile in these nuclei [Ko 88]. These two quantities are linked since the "size" of the nucleus is roughly proportional to the inverse of the square root of the separation energy. Using the Goldhaber model for soft fragmentation, the authors of ref. [Ko 88] were able to relate the widths of the narrow peaks in the momentum distributions with the separation energies and sizes of the radioactive nuclei. However, this approach is not free of bias. The interaction of the fragments with the target broadens the narrow peak and makes the extraction of quantitative information about these quantities strongly model-dependent and potentially inaccurate.

We show here that a better measure of the interaction size of the radioactive projectile is obtained by the longitudinal momentum distribution of its fragments. It is also shown that the Coulomb and nuclear fragmentation amplitudes have longitudinal momentum distributions with very nearly equal widths. This fact has indeed been verified in a recent experiment at the NSCL/MSU [Or 92]. On the other hand, the transverse momentum distributions are substantially broadened by the size and diffuseness of the interaction with the target and contain Coulomb and nuclear contributions with different widths. The interpretation of the "wide" (core-neutron) component of the transverse momentum distributions is therefore less straightforward than that of the longitudinal ones.

We follow below the recent work of Bertulani and McVoy [BM 92], using a simple cluster description of the radioactive nuclei. The conclusions drawn are however of general validity. The cluster model only serves as a guide to obtain an analytical insight into the results. The systems studied experimentally involve reactions of the form

$$a + A \rightarrow b + x + A^* \equiv b + X\,. \tag{7.1}$$

According to ref. [HM 85], a spectator model of a ≡ b + x gives the singles spectra of the particle b as

$$\frac{d\sigma}{d\Omega_b dE_b} = \rho(E_b)\frac{2E_*}{\hbar v_a k_x}\int d^2b_x |\tilde{\phi}_a(\boldsymbol{q}, \boldsymbol{b}_x)|^2 [1 - |S_{xA}(b_x)|^2] , \tag{7.2}$$

$$|\tilde{\phi}_a(\boldsymbol{q}, \boldsymbol{b}_x)|^2 = \left| \int d^3r_b \exp(i\boldsymbol{q}_b \cdot \boldsymbol{r}_b) S_{bA}(b_b)\phi_a(\boldsymbol{r}_b - \boldsymbol{r}_x)\right|^2 . \tag{7.3}$$

The quantity $S_{iA}(b_i)$ is the S-matrix for the scattering of cluster i (i = b, x) from the target A. We obtain it from a complex optical potential by means of the eikonal approximation. For the optical potential we use the $t\rho\rho$ formalism (see, e.g., ref. [HRB 91]), which is obtained by folding the nuclear densities of the participant nuclei weighted by the nucleon–nucleon scattering cross section, with medium correction effects. We shall here concentrate on reactions involving ^{11}Li, ^{11}Be, and ^{6}He, and compare our results with the measurements of the momentum distributions of the ^{9}Li, ^{10}Be, and ^{4}He fragments, respectively. The Hartree–Fock densities for these nuclei were taken from ref. [BBS 89], except for the ^{6}He, which was taken from ref. [Su 91]. The density distributions of the knocked-out neutrons were taken as the difference between the neutron distributions of the original nuclei and of the observed fragments.

In eq. (7.3), ϕ_a represents the cluster wave function for the incoming a = b + x projectile. If one assumes that the fragment b does not interact with the target, i.e., $S_{bA}(b) \equiv 1$, one finds

$$d\sigma/d\Omega_b dE_b = \rho(E_b)\sigma^R_{xA}|\phi_a(\boldsymbol{q}_b)|^2 , \tag{7.4}$$

where σ^R_{xA} is the total reaction cross section of fragment x with the target A, and $\phi_a(\boldsymbol{q}_b)$ is the Fourier transform of $\phi_a(\boldsymbol{r}_b - \boldsymbol{r}_x)$ with respect to $\boldsymbol{q}_b$. The above result is known as the Serber model limit [Se 47]. It tells us that in this approximation the breakup mechanism measures the momentum-space internal wave function of the projectile, so that the singles spectrum of fragment b provides important information about the internal structure of the projectile. This is especially useful for the study of extremely short-lived nuclei in secondary beam reactions.

Unfortunately, the Serber model is only a rough approximation for most cases and the elastic scattering (including absorption) of the fragment b on the target has to be included, leading to an unavoidable broadening of the momentum distributions [Ut 90a, b]. The physical origin of this broadening is simple diffraction (i.e., the uncertainty principle), as an examination of eq. (7.3) makes clear. For instance, if $S_{bA} \equiv 1$, the Fourier transform given by this equation would be exactly the Fraunhofer diffraction pattern (as a function of $\boldsymbol{q}_b$) of the "source distribution" $\phi_a(\boldsymbol{r}_b - \boldsymbol{r}_x)$. Including the factor $S_{bA}(b_b)$, with $|S_{bA}(b_b)| \leq 1$, effectively decreases the transverse width of the source by eliminating the part that overlaps with the target A, and this will of course broaden the transverse diffraction pattern.

This broadening makes it harder to extract the internal momentum structure of the projectile. However, since for high-energy collisions the S-matrix S_{bA} does not depend on the longitudinal coordinate, the longitudinal momentum distribution is expected to be much less altered by the S_{bA} absorption. In particular, a gaussian shape is quite appropriate for the light projectiles considered here, and in this case the longitudinal and transverse parts of the integral of eq. (7.3)

factorize completely. That is, if one takes for the projectile cluster wave function the approximation

$$\phi_a \propto \exp[(-\boldsymbol{b}_b - \boldsymbol{b}_x)^2 \Delta^2] , \tag{7.5}$$

one finds

$$\begin{aligned} d\sigma/dq_\parallel^{(b)} = (2\pi)^2 (E_x/\hbar v_a k_x) (C_\Delta^2/\Delta^2) \exp[-(q_\parallel^{(b)})^2/2\Delta^2] \\ \times \int d^2 b_x \, b_x \exp(-2\Delta^2 b_x^2)[1 - |S_{xA}(b_x)|^2] \\ \times \int db_b \, b_b \exp(-2\Delta^2 b_b^2) I_0(4 b_x b_b \Delta^2) |S_{bA}(b_b)|^2 , \end{aligned} \tag{7.6}$$

where the C_Δ is a normalization constant and I_0 a Bessel function. That is, the dependence on $q_\parallel^{(b)}$ is given by a Gaussian function multiplied by a geometrical factor. Therefore, the longitudinal momentum distribution measures the internal momentum function of the projectile and is insensitive to the details of the nuclear interaction. This fact was pointed out by Friedman in the general context of nuclear fragmentation reactions [Fr 83].

Due to their low separation energies, the projectiles near the β-instability line are also easily Coulomb excited/fragmented. It is well known that the electromagnetic excitation cross sections induced in nuclear collisions are directly related to the cross sections induced by real photons [BB 88c]. The proportionality factor is the so-called number of virtual photons, which is a slowly varying function of the photon energy. Therefore, the momentum distribution of the fragments will be determined by a matrix element of the form (in the dipole approximation)

$$\mathcal{M}_{if} = \int r Y_{1m}(\hat{r}) \phi_f^*(r) \phi_i(r) \, d^3 r . \tag{7.7}$$

We again assume that the initial wave function ϕ_i has a gaussian form, and use plane waves for the final state. This neglects the final-state interaction of b with A, an approximation appropriate to the Coulomb fragmentation, which takes place farther from A than does the nuclear fragmentation. With these assumptions, one finds that the momentum distribution of the fragments due to the Coulomb interaction has a gaussian shape in all three components of $\boldsymbol{q}_b$,

$$d^2\sigma/dq_b^2 = \text{const} \times q_b \exp(-q_b^2/2\Delta^2) . \tag{7.8}$$

Integrating over $k_T^{(b)}$ one gets to a good approximation another gaussian distribution for the longitudinal momentum distribution, this time from the electromagnetic fragmentation process.

Recently, the longitudinal momentum distribution of ^{9}Li has been obtained from the fragmentation of ^{11}Li projectiles with 70 MeV A has been measured at the NSCL/MSU using several targets [Or 92]. The data was taken using light and heavy targets, thus probing the effects of the nuclear and the Coulomb interaction on the breakup. As shown in fig. 56, this width can be explained by using eq. (7.5) and a calculation for the electromagnetic breakup of the projectile [BB 88c] with the value $\Delta = 20$ MeV/c, for all targets. A recent detailed calculation by Esbensen and Bertsch for the electromagnetic dissociation of ^{11}Li on tantalum [EB 91], accounting for

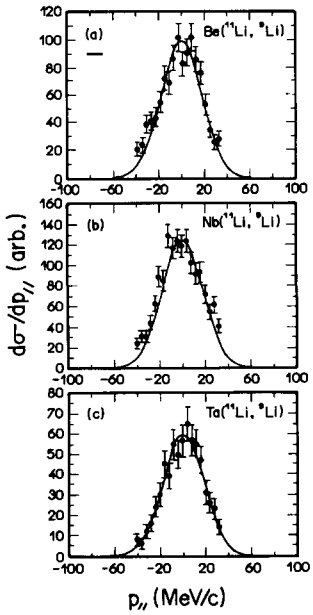

Fig. 56. Longitudinal momentum distributions of ^{9}Li from the breakup of ^{11}Li incident on (a) Be, (b) Nb and (c) Ta, at 70 MeV A. The data are from [Or 92] and the curves are from eqs. (7.2) and (7.6), normalized to the data.

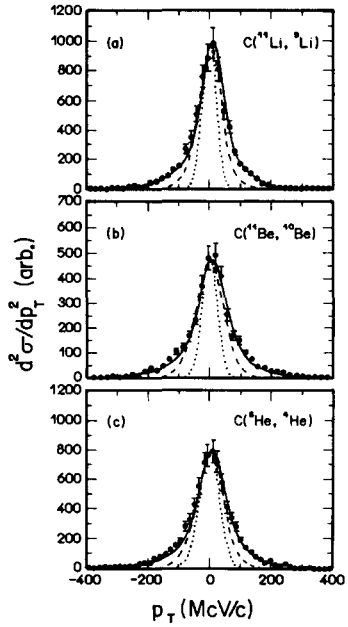

Fig. 57. Transverse momentum distributions of (a) ^{9}Li fragments from the breakup of ^{11}Li, (b) ^{10}Be fragments from the breakup of ^{11}Be and (c) ^{4}He fragments from the breakup of ^{6}He projectiles incident on C at 800 MeV A. The data are from ref. [Ko 88]. The dotted and dashed curves describe halo neutron only, the dotted curve neglecting final-state neutron interactions with the target, and the dashed curve including them via eqs. (7.6) and (7.9). The solid curves are two-Gaussian fits to the data, using a width determined by the binding of the core and halo neutrons of the projectile.

initial- and final-state correlations between the valence neutrons in ^{11}Li, has also obtained this value for the momentum width. This momentum width can be approximately related to the separation energy of the ^{11}Li by $E_B \simeq \Delta^2/\mu_{bx} = 0.26$ MeV, which agrees well with the experimental value in direct measurements. Although approximate, this relation shows that in fact the separation energy can be obtained from the measurements of the widths of the longitudinal momentum distributions.

Using the gaussian shape for ϕ_a and integrating eq. (7.2) over $q_{\parallel}^{(b)}$, one obtains for the transverse momentum distribution

$$\frac{d^2\sigma}{dq_{T(b)}^2} = \sqrt{2\pi}\frac{E_x}{\hbar v_a k_x}\frac{C_\Delta^2}{\Delta}\int d^2b_x\, b_x \exp(-2\Delta^2 b_x^2)[1-|S_{xA}(b_x)|^2] \tag{7.9}$$

$$\times \sum_{m=-\infty}^{m=\infty}\left|\int db_b\, b_b \exp(-\Delta^2 b_b^2) J_m(q_T^{(b)} b) I_m(2b_x b_b \Delta^2) S_{bA}(b_b)\right|^2 ,$$

where J_m and I_m are Bessel functions. In contrast to eq. (7.5), the above relation shows that the transverse momentum distribution depends on the target size parameters.

Figure 57 shows the transverse momentum distributions of ^{9}Li, ^{10}Be and ^{4}He from the breakup of ^{11}Li, ^{11}Be and ^{6}He projectiles, respectively, incident on carbon at 800 MeV A. For this target

only the nuclear contribution to the breakup needs to be considered. The data are from ref. [Ko 88]. The dotted curves are the result of the Serber model calculation following eq. (7.3). The momentum parameters Δ were determined by the separation energies of the fragments with the approximate formula $\Delta = \sqrt{\mu_{bx} E_B}$ which give the values 0.25 MeV, 0.5 MeV and 0.97 MeV for ^{11}Li, ^{11}Be and ^{6}He, respectively. The dashed curves were obtained using the more correct approach of eq. (7.2).

In the case of ^{11}Li the result of the Serber model agrees with the one obtained for the longitudinal momentum distribution data of NSCL/MSU, since the momentum distribution given by this model is isotropic. The interaction of the fragments with the target broadens the peak, and this is displayed by the dashed curves in this figure. However, it is also seen that the wings of the momentum distributions cannot be reproduced by using a single gaussian parametrization for the ground-state wave function. This is due to the simple cluster-model picture that we have adopted. More realistic models are able to describe these wings (wide component) [Zh 91a, b], but our analysis is consistent with the idea that the narrow peak measures the separation energy of the halo fragments.

An attempt to explain the wings of the momentum distributions displayed in fig. 57 (solid lines), can be made by assuming that also neutrons from the core of the projectile could be removed with appreciable probability [Ko 88]. One can assume that the cross sections for the removal of the loosely bound valence neutrons and the more tightly bound from the core add incoherently. The results are shown by the solid lines in fig. 57. In this calculation we added two results of eq. (7.8): the results which yield the dashed lines in fig. 57, with other results with the internal momentum widths $\Delta_2 = 55$ MeV/c, 92 MeV/c and 79 MeV/c, for ^{11}Li, ^{11}Be and ^{6}He, respectively. The Hartree–Fock densities for the core nucleons were taken from refs. [BBS 89; Su 91]. These momentum widths are much wider than the one cited before, and are related to the separation energies of the core neutrons. The contributions of the two gaussian simulations for the internal wave functions were chosen so as to reproduce as well as possible the experimental data. The excellent agreement with the experimental data (solid lines in fig. 57) should therefore be approached with some caution, since any two gaussian fits can reproduce the transverse momentum data [Ko 88]. Nonetheless, the ratio between the two contributions gives roughly the spectroscopic factors for the removal of neutrons from the core and from the halo, respectively. This ratio, $\sigma_{wide}/\sigma_{narrow}$, is however large, being about 0.4 for the fragmentation of ^{11}Li. It is hard to believe that so many events could be originated by the removal of tightly bound neutrons. We are more inclined to think that the observed wings are the results of three-body effects, as claimed by Zhukov et al. [Zh 91a, b].

Another interesting feature shown in fig. 57 is a small shift of the peaks with respect to the central position ($q_T = 0$). This shift arises from the phase of the S_b-matrices originating in the real part of the potential, but is small and has been neglected in our calculations.

In order to test the dependence of these results on the ^{11}Li wavefunction, we have used Yukawa wavefunctions instead of gaussians. No appreciable deviation from the previous results was found, as long as appropriate values for the size parameter were chosen.

The above analysis shows that the longitudinal momentum distribution which results from the fragmentation of weakly bound light projectiles is insensitive to the interaction, and provides a reliable probe of the internal momentum wave function of the projectile. On the other hand, the transverse momentum distribution depends on the reaction mechanism, and the extraction of definite information about the halo size is not free of bias. One interesting problem to be studied is the extension of the experimental measurements to look for the possible existence of wings in the longitudinal momentum distributions, which do not appear in the data of ref. [Or 92]. The

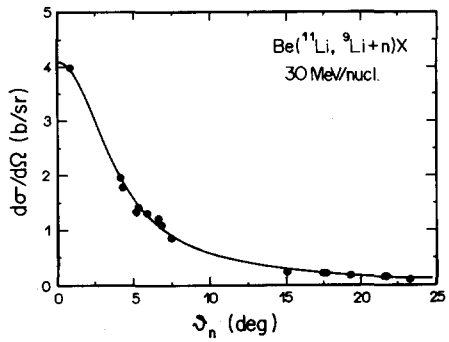

Fig. 58. The angular distribution of the neutrons in the Be(^{11}Li, ^{9}Li + n)x at 30 MeV/nucleon. Data points are from ref. [An 90] and the solid curve, the result of the calculation according to section 7.2.

existence of such wings would provide a more definitive measure of the contribution of more tightly bound nucleons, from the core of the projectiles, which have been assumed to explain the wings of the transverse momentum distribution [Ko 88].

7.2. Angular distribution of neutrons

The spectator model above discussed [HM 85] can also be used to describe the angular distributions of emitted neutrons in the fragmentation of ^{11}Li at lower energies. In particular we discuss here the data of Anne et al. [An 90] and take the reaction Be(^{11}Li, ^{9}Li + n)X at 30 MeV A, as an example. We avoid the complications of eqs. (7.6) and (7.9) observing that (see appendix A) the yield of dineutrons within the cluster model is given by (ignoring the Coulomb contribution)

$$Y_{2n} = \frac{1}{\sigma^2} \sum_{j=0}^{\infty} [1 - \hat{T}_j^{2n}(\sigma)]\, \hat{T}_j^{^9\mathrm{Li}}(\sigma)\,, \tag{7.10}$$

where the quantities σ and $\hat{T}_j^x(\sigma)$ are defined in the appendix. Since the reaction is inclusive, we take Y_{2n} to be an angle-integrated incoherent cross section and consider j as an angular momentum. We then have for the two-neutron angular distribution [BH 92]

$$\frac{d\sigma_{2n}}{d\Omega_{2n}} = \frac{1}{2\sigma^2} \sum_{j=0}^{\infty} [1 - \hat{T}_j^{2n}(\sigma)]\, \hat{T}_j^{^9\mathrm{Li}}(\sigma)[P_j(\cos\theta)]^2\,. \tag{7.11}$$

Taking $\sigma = 0.136\,\mathrm{fm}^{-1} = 24\,\mathrm{MeV}/c$, which is the value associated with the correct separation energy of the two neutrons in ^{11}Li, we obtain the excellent agreement with the data of Anne et al. [An 90], shown in fig. 58.

Of course for ^{11}Li interaction with heavier targets, the Coulomb contribution becomes dominant. We refer the reader to the discussion of Esbensen [Es 91].

8. Conclusions

In this report the several facets of neutron-rich nuclei are discussed and analysed. In particular, the reactions of nuclei such as ^{11}Li with light and heavy targets are exhaustively described both at

low and intermediate energies. The signature of the neutron halo is sought in elastic scattering, pion production, sub-barrier fusion and breakup reactions. The major conclusions of this report are the following. From simple three-body considerations, the dineutron in ^{11}Li is weakly bound to the core ^{9}Li through an effective $1/r^2$-like interaction. This fact allows the introduction of the appropriate name for these exotic systems: Rydberg nuclei. It is difficult to distinguish between the simple cluster model and the excitation of the low-lying "soft" giant dipole resonance (the pygmy resonance) through an analysis of the ~ 1 GeV A fragmentation reactions. Both models give similar Coulomb dissociation cross sections. Detailed calculation within the cluster model in fact give a very good account for the fragmentation cross section both at intermediate and high energies.

In so far as the dipole strength distribution is concerned, we have shown here that a hybrid RPA–cluster calculation can be formulated in a reasonably consistent way. In such a calculation three species of particles are considered: protons, neutrons and dineutrons. This way, a special, clearly needed, attention to two-body correlations (pairing) is given. The resulting dipole strength distribution in ^{11}Li was found adequate when used to calculate the Coulomb dissociation cross section.

The elastic scattering of ^{11}Li on ^{12}C, p and α was then considered within the optical model and a more detailed multiple-scattering framework. The existence of the halo was found to be intimately related to conspicuous changes in the refractive aspects of the angular distribution. The effect of two-nucleon correlations is also assessed.

A detailed study of the effect of the breakup channel on the elastic scattering of ^{11}Li was made.

The corresponding dynamic polarization potential was found to be predominantly absorptive and of a long-range nature. The inclusion of this potential in the calculation of $d\sigma/d\sigma_R$ was then done and an important 40%, almost angle-independent, damping of the angular distribution was predicted. The real part of the polarization potential was calculated with the aid of a dispersion relation and was found to be repulsive and small.

The problem of pion production that accompanies the interaction of ^{11}Li with, e.g., ^{12}C, was then discussed and the halo effect considered. The fact that pions produced from the interaction of halo neutrons with the target have different spectral shapes from those coming from the interaction of core nucleons, is emphasized. The sub-barrier fusion of ^{11}Li on heavy spherical and deformed targets is then calculated taking into account both the pygmy resonance and cluster aspects. Important conspicuous structure in σ_F was found around the Coulomb barrier.

Finally, the astrophysical application of the nuclear physics of these exotic systems, and the major characteristics of the low-energy momentum and angular distributions of the ejectiles in the fragmentation of ^{11}Li were discussed in great detail.

Acknowledgements

The ideas developed in this report have matured through our very fruitful collaboration with many colleagues: Armando Aleixo, Gerhard Baur, Wolfgang Bauer, George Bertsch, Raul Donangelo, Helio Dias, Kazuo Ieki, Aaron Galonsky, Domenique Kalassa, Siegfried Krewald, Bao-An Li, Kirk McVoy, Nigel Orr, Mauricio Pato, Don Sackett, Ray Satchler, Brad Sherrill and T. Teruya.

This work was partially supported by the CNP$_q$ (Brazil) and the National Science Foundation (USA), under grant no. PHY-9017077.

Appendix A. Theory of the primary yield

Fragment emission in heavy-ion reactions at intermediate and higher energies is a common occurrence [Si 90]. Several models have been devised to calculate the cross section. These range from statistical [Ha 85], microscopic Monte Carlo [Mo 88; Fr 83] and others. A fully quantum mechanical treatment based on general reaction theory concepts is still lacking. Recently [HM 85, 89], a general reaction theory of nuclear fragmentation has been developed and applied successfully to several reactions involving a partial fusion of the projectile (incomplete fusion, IF). In these calculations, the inclusive spectator particle angular and energy distributions are usually presented. It is the purpose of this appendix to present a theory of the yield of spectator particles in these reactions. The expression for the inclusive inelastic breakup cross section derived here is used in section 2.1.

To be specific we consider the following process

$$a + A \equiv (b + x) + A \rightarrow b + \sum_{\text{all states}} (x + A) . \tag{A.1}$$

In the spectator–DWBA treatment of Hussein and McVoy [HM 85], the yield of b is given by

$$P_b = \int \frac{d^2\sigma}{d\Omega_b dE_b} d\Omega_b dE_b , \quad \frac{d^2\sigma}{d\Omega_b dE_b} = -\frac{2}{\hbar v_a} \rho(E_b) \langle \hat{\psi}_x^{(+)} | W_{xA} | \hat{\psi}_x^{(+)} \rangle , \tag{A.2a, b}$$

where $\rho(E_b)$ is the density of states of b and is equal to $\mu_b k_b/(2\pi)^3\hbar^2$, v_a is the velocity of the projectile and $\hat{\psi}_x^{(+)}$ is given by

$$|\hat{\psi}_x^{(+)}\rangle = (\chi_b^{(-)} | \phi_a \chi_a^{(+)}\rangle . \tag{A.3}$$

In (A.3) the χ refer to distorted waves, and ϕ_a is the intrinsic wave function of a. The symbol $(|\rangle$ implies that the b coordinates are integrated over. Finally $-W_{xA}$ is the imaginary part of the x–A optical potential. Note that eq. (A.2b) describes the inclusive inelastic breakup. The elastic breakup piece of $d^2\sigma/d\Omega_b dE_b$ is known to contribute less than 10% at moderate and higher energies [Ba 84].

Employing the Glauber approximation for the distorted waves allows writing the matrix element $\langle \hat{\psi}_x^{(+)} | W_{xA} | \hat{\psi}_x^{(+)} \rangle$ as a function of the momentum transfer $\boldsymbol{q}_b = \boldsymbol{k}_b - \boldsymbol{k}'_b$, where $\boldsymbol{k}_b$ ($\boldsymbol{k}'_b$) is the wave number of b in the incident (final) channel. Thus transforming the energy and angle integral in eq. (A.1) into a momentum-transfer integral allows the reduction to the following transparent form of P_b:

$$P_b = \frac{2}{v_a} \frac{E_x}{\hbar k_x} \sqrt{\frac{\pi}{\sigma^2}} \int d\boldsymbol{b}_b |S_b(b_b)|^2 \int d\boldsymbol{b}_x |\phi_a(|\boldsymbol{b}_b - \boldsymbol{b}_x|)|^2 [1 - |S_x(b_x)|^2] , \tag{A.4}$$

where b refers to the impact parameter, and $S(b)$ the elastic element of the S-matrix. In obtaining (A.4) a normalised Gaussian is used for $\phi_a(\boldsymbol{r}_b - \boldsymbol{r}_x)$ which, when cylindrical coordinates $\boldsymbol{r} = z\hat{\boldsymbol{z}} + b\hat{\boldsymbol{b}}$ are used, can be expressed as

$$\phi_a(|\boldsymbol{r}_b - \boldsymbol{r}_x|) = (\sigma^3/\pi\sqrt{\pi})^{1/2} \exp[-\tfrac{1}{2}\sigma^2(z_b - z_x)^2] \exp[-\tfrac{1}{2}\sigma^2(\boldsymbol{b}_b - \boldsymbol{b}_x)^2] . \tag{A.5}$$

The z_b and z_x integrals in the original formulas eqs. (A.1) and (A.2a) have already been performed in (A.4).

A further reduction of eq. (A.4) can be made by integrating over the polar angles of $\boldsymbol{b}_b$ and $\boldsymbol{b}_x$, which results in the following simple formula, after writing $E_x/\hbar k_x = v_x = v_a$,

$$P_b = \frac{\sigma^2}{\pi} \int_0^\infty b_b \, db_b \, |S_b(b_b)|^2 \exp(-\sigma^2 b_b^2) \int_0^\infty b_x \, db_x \, [1 - |S_x(b_x)|^2]$$

$$\times \exp(-\sigma^2 b_x^2)[4\pi^2 J_0(-2i\sigma^2 b_b b_x)] \,, \tag{A.6}$$

where J_0 is the cylinder Bessel function. The factor $4\pi^2 J_0(-2i\sigma^2 b_b b_x)$ was obtained from the relation [AS 64]

$$\int_0^{2\pi} d\phi \int_0^{2\pi} d\beta \exp[2\sigma^2 b_x b_x \cos(\beta - \phi)] = 4\pi^2 J_0(-2i\sigma^2 b_x b_b) \,.$$

To proceed further we use the following expansion of J_0 [AS 64]:

$$J_0(z) = \sum_{j=0}^{\infty} (-)^j z^{2j}/(2)^{2j}(j!)^2 \,. \tag{A.7}$$

With (A.7), eq. (A.6) can be finally written in the following simple form:

$$P_b = \frac{\pi}{\sigma^2} \sum_{j=0}^{\infty} [1 - \hat{T}_j^b(\sigma)] \, \hat{T}_j^x(\sigma) \,, \tag{A.8}$$

where we have introduced the symbol $\hat{T}$ to represent the following dimensionless integral:

$$\hat{T}_j^i(\sigma) = [(\sigma^2)^{j+1}/j!] \int_0^\infty b_i^{2j} \, db_i^2 \exp(-\sigma^2 b_i^2) T_i(b_i) \,, \tag{A.9}$$

where $T_i(b_i)$ is the transmission coefficient $1 - |S_i(b_i)|^2$ and i is either b or x. It is important to note that $\hat{T}$, eq. (A.9) becomes unity in the limit $|S| = 1$.

Equation (A.8) is an important result of this appendix. It expresses the projectile-like primary fragment yield in a conventional total reaction cross-section form, with the width σ^2 playing the role of the squared wave number, and the label j playing the role of angular momentum. It is easy to verify that eq. (A.8) reduces to the known limiting cases. To see this we first note that the integral $\hat{T}_j^i(\sigma)$ as a function of j looks very much like $T(b) \equiv 1 - |S(b)|^2$ versus b. Therefore $[1 - \hat{T}_j^b(\sigma)] \hat{T}_j^x(\sigma)$ should be a localized (window) in j. The value of j at which the "peaking" occurs can be estimated as follows. The function $b^{2j} \exp(-\sigma^2 b^2)$ peaks at $b^2 = j/\sigma^2$ and the b integral in $\hat{T}$ counts this peak as long as $b < b_g = [(E - E_B)/E]^{1/2} R$, where E_B is the height and R the position

of the Coulomb barrier characterizing $T(b)$. Thus the critical value of j which defines the boundary of the function $\hat{T}$ is

$$j_c = \sigma^2 [(E - E_B)/E] R^2 . \tag{A.10}$$

The function $1 - \hat{T}$ behaves in exactly the opposite way to $\hat{T}$ and thus $(1 - \hat{T}_j^b)\hat{T}_j^x$ has a window shape in j. The detailed form of this window depends upon the physical parameters that specify the functions $\hat{T}_j^b(\sigma)$ and $\hat{T}_j^x(\sigma)$.

An interesting case which received several considerations in the past is the Serber model [Se 47], $S_b = 1$. This limit corresponds to setting $1 - \hat{T}_j^b(\sigma) = 1$ in our formula eq. (A.9). Approximating $\hat{T}_j^x(\sigma)$ by a sharp cutoff from $\Theta(j_c - j)$, we obtain immediately for the yield,

$$P_b^{\text{Serber}} \simeq \frac{\pi}{\sigma^2} \sigma^2 \frac{E_x - E_B}{E_x} R_x^2 = \pi R_x^2 \frac{E_x - E_B}{E_x} = \sigma_{\text{reaction}}^x , \tag{A.11}$$

which is just the total reaction cross section of the participant particle (x).

The more realistic expression for P_b, eq. (A.8), gives, in the sharp-cutoff limit, the following sum rule:

$$P_b \simeq \frac{\pi}{\sigma^2} (j_c^x - j_c^b) \simeq \pi \left[\left(1 - \frac{E_B^x}{E_x} \right) R_x^2 - \left(1 - \frac{E_B^b}{E_b} \right) R_b^2 \right] = \sigma_{\text{reaction}}^x - \sigma_{\text{reaction}}^b , \tag{A.12}$$

which can be orders of magnitude smaller than P_b^{Serber}. Of course the energies E_x and E_b correspond to the incident channel, $E_x = (m_x/m_a)E_a$ and $E_b = (m_b/m_a)E_a$, and in the above equation $\sigma_{\text{reaction}}^x > \sigma_{\text{reaction}}^b$. Clearly when x is the light particle and b, the heavy one, the above approximation is not valid and one has to calculate eq. (A.8) exactly.

Appendix B. Uniform approximation for $K_{i\eta}(\xi)$

The modified Bessel function of imaginary order $K_{i\eta}(\xi)$ is discussed in most books and handbooks of special functions [AS 64; Gr 80]. No tables, however are given. Numerical integration of the integral that represents this function is necessary. This procedure, however, could generate large errors, depending on the value of η and ξ. It is the purpose of this appendix to perform a uniform approximation analysis that permits writing the function in terms of tabulated Airy function and its first derivative. In particular, we discovered that $K_{i\eta}(\xi)$ represents basically a rainbow scattering problem. The uniform approximation formulae are used for the evaluation of the low-energy CD cross section in section 2.3.

The integral representation of $K_{i\eta}(\xi)$ is given by in, e.g., Abramowitz and Stegun [AS 64] (p. 376),

$$K_{i\eta}(\xi) = \int_0^\infty \exp(-\xi \cosh t) \cos \eta t \, dt , \quad |\arg \xi| < \tfrac{1}{2}\pi . \tag{B.1}$$

Now since the integrand is even in t, we may rewrite (B.1) in the following form

$$K_{i\eta}(\xi) = \tfrac{1}{2} \int_{-\infty}^{\infty} \exp(-\xi \cosh t) \exp(i\eta t)\, dt \,. \tag{B.2}$$

We now change $t \to t + \frac{1}{2} i\pi$ and perform the integration along the line defined by $-\infty + i\pi < t < +\infty + \frac{1}{2} i\pi$. This leaves the result unchanged since the integrand in an analytic function. Using the relation $\cosh(t + \frac{1}{2} i\pi) = +i \sinh t$ we have

$$K_{i\eta}(\xi) = \tfrac{1}{2} \exp(-\tfrac{1}{2}\pi\eta) \int_{-\infty}^{\infty} \exp[-i(\xi \sinh t - \eta t)]\, dt \,. \tag{B.3}$$

Equation (B.3) is our starting point for applying the uniform approximation. According to the usual procedure of Chester, Friedman and Ursell [CFU 57], we map the function $\xi \sinh x - \eta x$ into

$$\xi \sinh t - \eta t = \tfrac{1}{3} \mu^3 + x\mu \,, \tag{B.4}$$

thus

$$K_{i\eta}(\xi) = \tfrac{1}{2} \int_{-\infty}^{\infty} \exp[i(\tfrac{1}{3}\mu^3 + x\mu)] \left(\frac{dt}{d\mu}\right) d\mu \,. \tag{B.5}$$

Before we proceed, we remark that the phase of the integrand in (B.2) is stationary when $\xi \cosh(\pm t) = \eta$, or

$$t = \pm \cosh^{-1}(\eta/\xi) \,, \quad \eta > \xi \,; \qquad t = \pm i \cos(\eta/\xi) \,, \quad \eta < \xi \,. \tag{B.6}$$

The situation can be easily understood from fig. 59 where $\xi \cosh t$ is plotted versus t. The minimum of $\xi \cosh t$ is at $t = 0$ and represents $\xi = \eta$, which is the "rainbow" η. For $\eta > \xi$ one is on the bright side of the rainbow whereas $\eta < \xi$ represents the dark side exemplified by two pure-imaginary stationary points (complex-conjugate of each other). When looked at from the cubic map, eq. (B.4), the stationary points are given by

$$\mu = \pm \sqrt{-x} \,. \tag{B.7}$$

The function $dt/d\mu$ is expanded as usual,

$$\frac{dt}{d\mu} = \sum_{n=0}^{\infty} a_n (\mu^2 + x)^n \,. \tag{B.8}$$

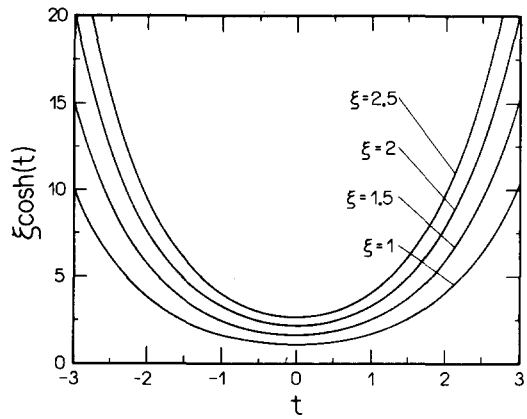

Fig. 59. The order "deflection function" $\xi \cosh t$ versus t for several values of ξ.

The coefficients in (B.8) are to be found by repeated differentiation of (B.4) at the stationary points (B.7). Thus, for a_0, a_1 and a_2, we need, $a_0 = (\mathrm{d}t/\mathrm{d}\mu)_{\mathrm{s.p.}}$, $a_1 2\mu = (\mathrm{d}^2t/\mathrm{d}\mu^2)_{\mathrm{s.p.}}$ and $2a_1 + 8\mu^2 a_2 = (\mathrm{d}^3t/\mathrm{d}\mu^3)_{\mathrm{s.p.}}$. Accordingly,

$$(\xi \cosh t - \eta)\, \mathrm{d}t/\mathrm{d}\mu = \mu + x\,, \tag{B.9a}$$

$$\xi \sinh t\, (\mathrm{d}t/\mathrm{d}\mu)^2 + (\xi \cosh t - \eta)\, \mathrm{d}^2t/\mathrm{d}\mu^2 = 2\mu\,, \tag{B.9b}$$

$$\xi \cosh t \left(\frac{\mathrm{d}t}{\mathrm{d}\mu}\right)^3 + 3\xi \sinh t \frac{\mathrm{d}t}{\mathrm{d}\mu}\frac{\mathrm{d}^2t}{\mathrm{d}\mu^2} + (\xi \cosh t - \eta)\frac{\mathrm{d}^3t}{\mathrm{d}\mu^3} = 2\,, \tag{B.9c}$$

$$\xi \sinh t \left(\frac{\mathrm{d}t}{\mathrm{d}\mu}\right)^4 + 6\xi \cosh t \left(\frac{\mathrm{d}t}{\mathrm{d}\mu}\right)^2 \frac{\mathrm{d}^2t}{\mathrm{d}\mu^2} + 3\xi \sinh t \left(\frac{\mathrm{d}^2t}{\mathrm{d}\mu^2}\right)^2 + 4\xi \sinh t \frac{\mathrm{d}t}{\mathrm{d}\mu}\frac{\mathrm{d}^3t}{\mathrm{d}\mu^3} + (\xi \cosh t - \eta)\frac{\mathrm{d}^4t}{\mathrm{d}\mu^4} = 0\,. \tag{B.9d}$$

At the stationary points $\xi \cosh t - \eta = 0$ and $\mu^2 = -x$, and thus eq. (B.9b) gives

$$\left(\frac{\mathrm{d}t}{\mathrm{d}\mu}\right)^2 = \frac{2\mu}{\xi \sinh t} = \frac{2\mu}{\xi\sqrt{\cosh^2 t - 1}} = \frac{2\mu}{\xi\sqrt{\eta^2/\xi^2 - 1}} = \frac{2\sqrt{-x}}{\sqrt{\eta^2 - \xi^2}} = \left(\frac{-4x}{\eta^2 - x^2}\right)^{1/2},$$

or

$$(\mathrm{d}t/\mathrm{d}\mu)_{\mathrm{s.p}} = [-4x/(\eta^2 - \xi^2)]^{1/4} \equiv a_0\,. \tag{B.10}$$

Equations (B.9c, d) give

$$a_1 = \frac{1}{2\mu}\left[\frac{d^2t}{d\mu^2}\right]^2_{s.p.} = \frac{2 - 4[-4x/(\eta^2 - \xi^2)]^{3/4}}{6\sqrt{\eta^2 - \xi^2}\,[-4x/(\eta^2 - \xi^2)]^{1/4}(-x)^{1/2}}, \qquad a_2 = \frac{[d^3t/d\mu^3]_{s.p.} - 2a}{8(-x)}, \tag{B.11}$$

$$[d^3t/d\mu^3]_{s.p.} = \frac{-\sqrt{\eta^2 - \xi^2}\,[dt/d\mu]^4_{s.p.} - 6\eta\,[dt/d\mu]^2_{s.p.}[d^2t/d\mu^2]^2_{s.p.} - 3\sqrt{\eta^2 - \xi^2}\,[d^2t/d\mu^2]^2_{s.p.}}{4\sqrt{\eta^2 - \xi^2}\,[dt/d\mu]_{s.p.}}. \tag{B.12}$$

From eq. (B.4) we have for the x that appear, in (B.10), (B.11) and (B.12), in the illuminated region, $\eta > \xi$,

$$-\sqrt{\eta^2 - \xi^2} + \eta\cosh^{-1}(\eta/\xi) = +\tfrac{2}{3}(-x)^{3/2}. \tag{B.13}$$

In the forbidden region, $\eta < \xi$,

$$\sqrt{\eta^2 - \xi^2} - \eta\sin^{-1}\sqrt{1 - \eta^2/\xi^2} = \tfrac{2}{3}x^{3/2}. \tag{B.14}$$

Inserting (B.8) (keeping up to second-order terms) into (B.5), we have finally the desired formula, in terms of Airy's function Ai(x) and its first derivative Ai'(x),

$$K_{i\eta}(\xi) = [a_0\,\mathrm{Ai}(x) - 2a_2\,\mathrm{Ai}'(x)]\,e^{-\pi\eta/2}\,\pi, \qquad \mathrm{Ai}(x) = \frac{1}{2\pi}\int_{-\infty}^{\infty} e^{i(\mu^3/3 + \mu x)}\,d\mu, \tag{B.15}$$

where a_0 and a_2 are given by eqs. (B.10) and (B.12) respectively. Notice that the a_1 term gives zero since it is odd. Higher-order corrections can be easily generated.

The discussion above can be made more transparent when compared with a scattering problem [FW 59]. Here one speaks about the scattering at a given angle, which is the conjugate variable to the integration variable, the orbital angular momentum. The representation eq. (B.1) of $K_{i\eta}(\xi)$ identifies the order η with the "angle". For a given value of η two values of t contribute, which are the two stationary points determined from the equation $\xi\cosh(\pm t) = \eta$, where the function $\xi\cosh t$ represents a deflection function. The analogy with a scattering problem is a bit ill-based since both positive as well as negative t contribute. In a scattering situation only positive values of the angular momentum enter in the discussion. In any case $K_{i\eta}$ for a fixed value of ξ exhibits a double-rainbow form as a function of η. The rainbow η is just $\eta = \xi$. For $\eta < \xi$ one is the shadow of the rainbow, whereas $\eta > \xi$ represents the illuminated region (oscillatory behaviour). Both positive and negative values of η can be considered.

In fig. 60 we present $K_{i\eta}(\xi)$ for $\xi = 0.1, 0.5, 1.0, 5.0$ and 10.0 versus η. The rainbow in the order of $K_{i\eta}(\xi)$ is clearly exhibited.

The analogy with scattering becomes more sound when discussing the behaviour of $K_{i\eta}(\xi)$ with respect to ξ for fixed η. To make full use of this analogy it is more convenient to use another

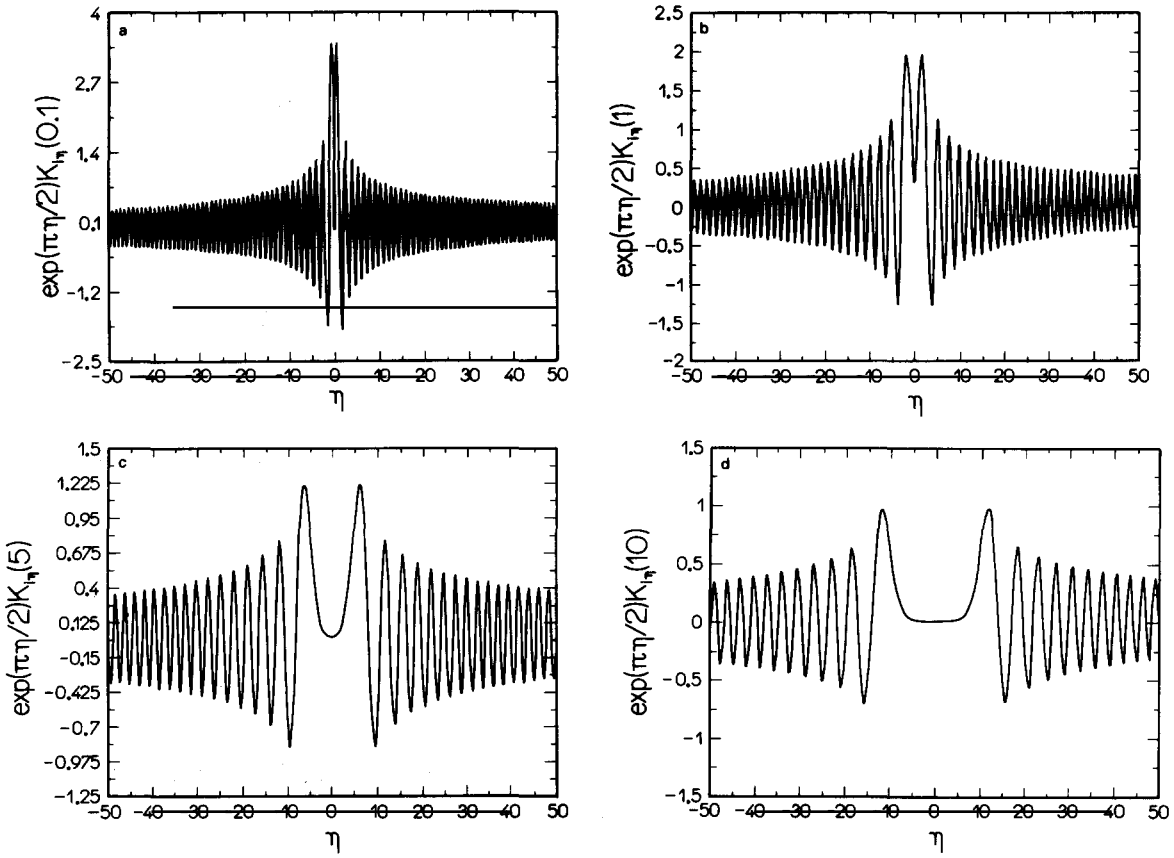

Fig. 60. Plot of $\exp(\pi\eta/2)K_{i\eta}(\xi)$ versus η for (a) $K_{i\eta}(0.1)$, (b) $K_{i\eta}(1)$, (c) $K_{i\eta}(5)$ and (d) $K_{i\eta}(10)$.

representation for the function. This new representation is obtained from eq. (B.1) by a change of variable $\sinh t = \lambda$. Then

$$K_{i\eta}(\xi) = \int \frac{d\lambda}{\sqrt{1+\lambda^2}} \exp(i\eta \sinh^{-1}\lambda - i\lambda\xi)\,, \tag{B.16}$$

which when integrated by parts, yields

$$K_{i\eta}(\xi) = \xi \int dx \exp(i\eta \sinh^{-1}\lambda - i\lambda\xi)\,. \tag{B.17}$$

The stationary points are determined from the condition

$$\eta(d/dx)\sinh^{-1}\lambda = \xi = \eta(1/\sqrt{\lambda^2+1})\,, \tag{B.18}$$

which is just eq. (B.6) rewritten in terms of the new variable λ. The deflection function $\eta/\sqrt{1+\lambda^2}$ is plotted in fig. 61. Again the rainbow value of ξ is $\xi = \eta$. In fig. 62 we show $K_{i0,1}(\xi)$, $K_{i1}(\xi)$, $K_{i5}(\xi)$

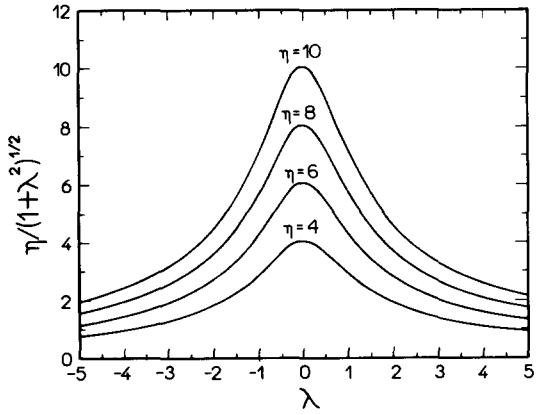

Fig. 61. The argument "deflection function" $\xi = \eta(1/\sqrt{1+\lambda^2})$, for several values of η.

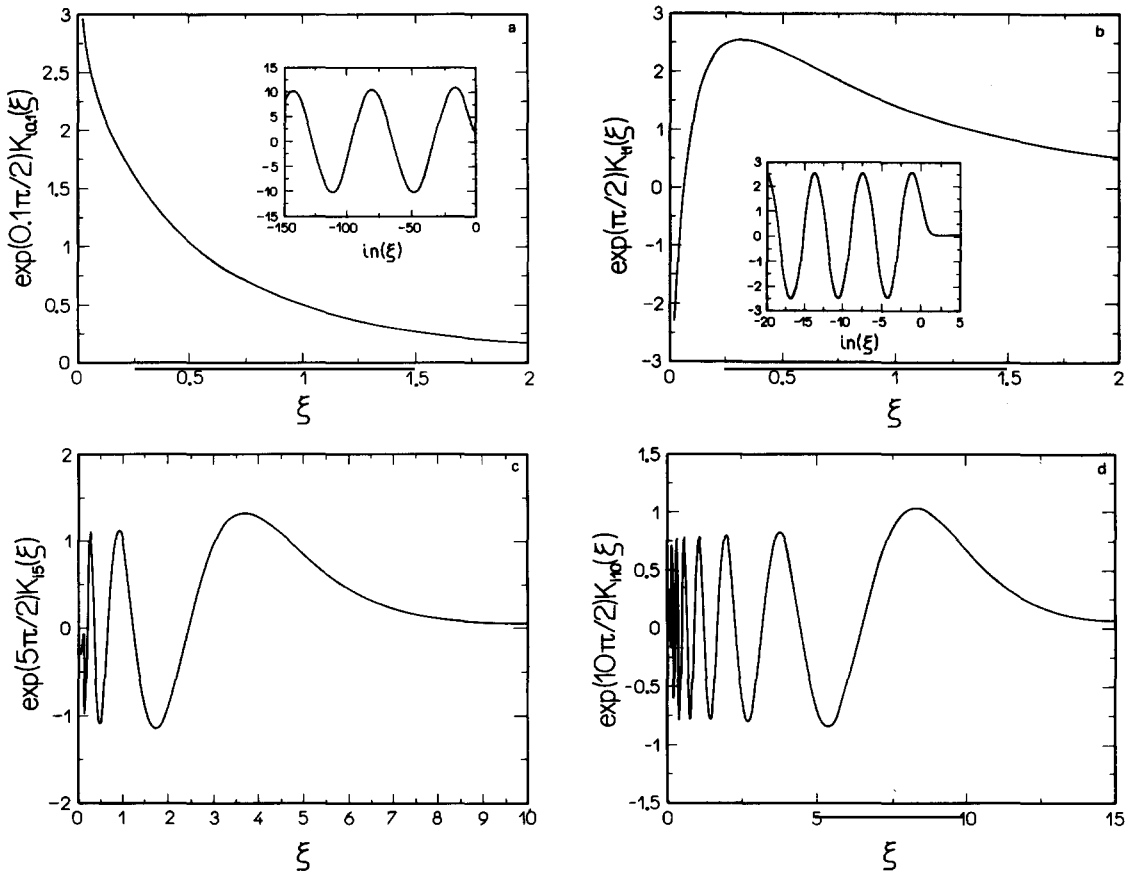

Fig. 62. (a) $K_{i0.1}(\xi)$, (b) $K_{i1}(\xi)$, (c) $K_{i5}(\xi)$ and (d) $K_{i10}(\xi)$ for very small values of ξ.

and $K_{i10}(\xi)$ which clearly show the Airy pattern that characterizes the rainbow in the argument.

In this appendix the uniform approximation is used to express the function $K_{i\eta}(\xi)$ in terms of Airy's function and its first derivative. It is found that $K_{i\eta}(\xi)$ represents, as a function of order η and argument ξ, a rainbow scattering situation. Further, we verified that the uniform series, eq. (B.15) is

rapidly convergent. In fact a_2/a_1 is almost always less than 1%. At the rainbow, $\eta = \xi$, we find the relation $a_2/a_1 = 1/(2^{2/3} \times 70 \times \eta^{4/3})$ [or $1/(2^{2/3} \times 70 \times \xi^{4/3})$], and thus, as long as $\eta(\xi)$ is not very small, the second term in (B.15) would contribute by, at most, a few percent. This appendix is partly based on recent work of Hussein and Pato [HP 92].

References

[AB 89] A.N.F. Aleixo and C.A. Bertulani, Nucl. Phys. A 505 (1989) 448.
[AB 91] A.N.F. Aleixo and C.A. Bertulani, Nucl. Phys. A 528 (1991) 436.
[ABH 91] A.N.F. Aleixo, C.A. Bertulani and M.S. Hussein, Phys. Rev. C 43 (1991) 2722.
[ABH 92] A.N.F. Aleixo, C.A. Bertulani and M.S. Hussein, Phys. Rev. C 45 (1992) 2403.
[AC 87] A. Aleixo, L.F. Canto, P. Carillho, R. Donangelo, L.S. de Paula and M.S. Hussein, J. Phys. G 13 (1987) 967.
[AFM 87] C. Alcock, G.M. Fuller and G.J. Mathews, Astrophys. J. 320 (1987) 439.
[Ag 89] P. Aguer et al., in: Proc. Inter. Symp. on Heavy Ion Physics and Nuclear Astrophysical Problems (Tokyo, 1989) (World Scientific, Singapore, 1989) p. 107.
[Ag 92] C.E. Aguiar, V. Barbosa, C.H. Dasso and R. Donangelo, submitted to Phys. Lett. B (1992).
[AHS 87] J.H. Applegate, C. Hogan and R.J. Scherrer, Phys. Rev. D 35 (1987) 1151.
[AHS 88] J.H. Applegate, C.J. Hogan and R.J. Scherrer, Astrophys. J. 329 (1988) 592.
[Al 82] Y. Alhassid, M. Gai and G.F. Bertsch, Phys. Rev. Lett. 49 (1982) 1482.
[Am 85] R.D. Amado, Analytical insight into intermediate energy hadron–nucleus scattering, in: Advances in Nuclear Physics, Vol. 5, eds J.W. Negele and E. Vogt (Plenum, New York, 1985).
[An 90] R. Anne et al., Phys. Lett. B 250 (1990) 19.
[Ap 87] J.H. Applegate, C. Hogan and R.J. Scherrer, Phys. Rev. D 35 (1987) 1151.
[AS 64] M. Abramowitz and I. Stegun, eds, Handbook of Mathematical Functions (U.S. GPO, Bureau of Standards, Washington, DC, 1964).
[Au 81] S.A. Austin, Prog. Part. Nucl. Phys. 7 (1981) 1.
[AW 66] K. Alder and A. Winther, Coulomb Excitation (Academic Press, New York, 1966).
[AW 75] K. Alder and A. Winther, Electromagnetic Excitation (North-Holland, Amsterdam, 1975).
[Ba 80] F.C. Barker, Aust. J. Phys. 33 (1980) 177.
[Ba 83] F.C. Barker, Phys. Rev. C 28 (1983) 1407.
[Ba 84] G. Baur, F. Rösel, D. Trautmann and R. Shyam, Phys. Rep. 111 (1984) 333.
[Ba 88] F.C. Barker, Phys. Rev. C 37 (1988) 2920.
[Ba 89] W. Bauer, Phys. Rev. C 40 (1989) 715.
[Ba 92] J.M. Bang and I.J. Thompson, Phys. Lett. B 279 (1992) 201.
[BB 87] G. Baur and C.A. Bertulani, Phys. Rev. C 35 (1987) 836.
[BB 88a] C.A. Bertulani and G. Baur, Nucl. Phys. A 480 (1988) 615.
[BB 88b] G. Baur and C.A. Bertulani, Nucl. Phys. A 482 (1988) 313c.
[BB 88c] C.A. Bertulani and G. Baur, Phys. Rep. 163 (1988) 299.
[BBH 91] C.A. Bertulani, G. Baur and M.S. Hussein, Nucl. Phys. A 526 (1991) 751.
[BBK 92] G. Baur, C.A. Bertulani and D. Kalassa, Nucl. Phys. A 550 (1992) 527.
[BBR 86] G. Baur, C.A. Bertulani and H. Rebel, Nucl. Phys. A 459 (1986) 188; in: Proc. Inter. Symp. on Weak and Electromagnetic Interactions in Nuclei (July 1986, Heidelberg) ed. H.V. Klapdor (Springer, Berlin, 1986) p. 980.
[BBS 89] G.F. Bertsch, B.A. Brown and H. Sagawa, Phys. Rev. C 39 (1989) 1154.
[BC 92] C.A. Bertulani and L.F. Canto, Nucl. Phys. A 539 (1992) 163.
[BCH 92] C.A. Bertulani, L.F. Canto and M.S. Hussein, Phys. Rev. C 45 (1992) 2995.
[Be 77] G.F. Bertsch, Phys. Rev. C 15 (1977) 713.
[BE 90] G.F. Bertsch, H. Esbensen and A. Sustich, Phys. Rev. C 42 (1990) 758.
[BE 91] G.F. Bertsch and H. Esbensen, Ann. Phys. 209 (1991) 15.
[BF 69] F.W. Byron and R.W. Fuller, Mathematics of Classical and Quantum Physics, Vol. I (Addison–Wesley, 1969) p. 148.
[BF 89] G.F. Bertsch and J. Foxwell, Phys. Rev. C 41 (1989) 1300.
[BH 90a] C.A. Bertulani and M.S. Hussein, Phys. Rev. Lett. 64 (1990) 1099.
[BH 91a] C.A. Bertulani and M.S. Hussein, Nucl. Phys. A 524 (1991) 306.
[BH 92] C.A. Bertulani and M.S. Hussein, to be published.
[BKG 78] A.J. Baltz, S.K. Kauffmann, N.K. Glendenning and K. Pruess, Phys. Rev. Lett. 40 (1978) 20; Nucl. Phys. A 327 (1979) 221.
[Bl 91] B. Blank et al., Z. Phys. A 340 (1991) 41.
[BM 92] C.A. Bertulani and K.W. McVoy, Phys. Rev. C 46 (1992) 2638.
[Bo 92] R.N. Boyd et al., Phys. Rev. Lett. 68 (1992) 1283.

[BPW 81] R.A. Broglia, G. Pollarolo and A. Winther, Nucl. Phys. A 361 (1981) 307, A 406 (1983) 369.
[Br 88] M.E. Brandan, Phys. Rev. Lett. 60 (1988) 784.
[BS 85] H.J. Bär and G. Soff, Physica C 128 (1985) 225.
[BS 86] F.C. Barker and R.H. Spear, Astrophys. J. 307 (1986) 847.
[BS 88] M.E. Brandan and G.R. Satchler, Nucl. Phys. A 487 (1988) 477.
[BS 92a] C.A. Bertulani and A. Sustich, Phys. Rev. C 46 (1992) 2340.
[BS 92b] C.A. Bertulani and H. Sagawa, Phys. Lett. B 300 (1992) 205.
[Bu 84] M. Buenerd et al., Nucl. Phys. A 424 (1984) 313.
[Ca 90] W. Cassing et al., Phys. Rep. 188 (1990) 363.
[CDH 91a] L.F. Canto, R. Donangelo and M.S. Hussein, Nucl. Phys. A 529 (1991) 243.
[CDH 91b] L.F. Canto, R. Donangelo, M.S. Hussein and M.P. Pato, Nucl. Phys. A 542 (1992) 131.
[CDS 92] L.F. Canto, R. Donangelo and H. Schulz, preprint NBI 92-91, submitted to Phys. Rev. C.
[CFU 57] C. Chester, B. Friedman and F. Ursell, Proc. Cambridge Philos. Soc. 53 (1957) 599.
[CH 92] L.F. Canto and M.S. Hussein, to be published.
[CIH 85] B.V. Carlson, M.P. Isidro Filho and M.S. Hussein, Phys. Lett. B 154 (1985) 89.
[CMV 81] J. Cugnon, T. Mizutani and J. Vandermeulen, Nucl. Phys. A 352 (1981) 505.
[DCH 79a] R. Donangelo, L.F. Canto and M.S. Hussein, Nucl. Phys. A 320 (1979) 422.
[DCH 79b] R. Donangelo, L.F. Canto and M.S. Hussein, Phys. Rev. C 19 (1979) 1801.
[DD 92] C.H. Dasso and R. Donangelo, Phys. Lett. B 276 (1992) 1.
[DLW 83] C. Dasso, S. Landowne and A. Winther, Nucl. Phys. A 405 (183) 381; A 407 (1983) 221.
[EB 92] H. Esbensen and G.F. Bertsch, Nucl. Phys. A 542 (1992) 310.
[Ef 70] V. Efimov, Phys. Lett. B 33 (1970) 563.
[Ef 81] V. Efimov, Nucl. Phys. A 362 (1981) 45.
[Es 91] H. Esbensen, Phys. Rev. C 44 (1991) 440.
[Fa 70] G. Fäldt, Phys. Rev. D 2 (1970) 846.
[FAG 89] P.B. Fernandez, E.G. Adelberger and A. Garcia, Phys. Rev. C 42 (1990) R804.
[Fe 62] H. Feshbach, Ann. Phys. 19 (1962) 287.
[FH 80] W.E. Frahn and M.S. Hussein, Phys. Lett. B 90 (1980) 358.
[FH 93] T. Frederico and M.S. Hussein, Mod. Phys. Lett. A 8 (1993) 295.
[FHM 81] M.Y. Fujimoto, T. Hanawa and S. Miyaji, Astrophys. J. 246 (1981) 267.
[Fi 91] M.C.S. Figueira et al., to be published.
[Fi 92] M.C.S. Figueira, E.M. Szanto, A. Szanto de Toledo, M.P. Pato, M.S. Hussein and L.F. Canto, IFUSP/P-957 (December 91), to be published.
[Fo 84] W.A. Fowler, Rev. Mod. Phys. 56 (1984) 149.
[Fr 83] W.A. Friedman, Phys. Rev. C 27 (1983) 569.
[FW 59] K.W. Ford and J.A. Wheeler, Ann. Phys. (NY) 7 (1959) 259, 287.
[GB 92] G.F. Bertsch and C.A. Bertulani, submitted to Nucl. Phys. A.
[GH 91] W.R. Gibbs and A.C. Hayes, Phys. Rev. Lett. 67 (1991) 1395.
[Gi 87] N. Van Giai et al., Phys. Lett. B 199 (1987) 155.
[Gl 55] R. Glauber, Phys. Rev. 99 (1955) 1515.
[Go 74] A.S. Goldhaber, Phys. Lett. B 53 (1974) 306.
[GR 80] I.S. Gradshteyn and I.M. Rhyzik, Table of Integrals, Series and Products (Academic Press, New York, 1980).
[Ha 85] B.G. Harvey, Nucl. Phys. A 445 (1985) 124.
[Ha 92] B.G. Harvey, LBL-preprint 1992.
[HBC 84] M.S. Hussein, A.J. Baltz and B.V. Carlson, Phys. Rep. 113 (1984).
[HJ 87] P.G. Hansen and B. Jonson, Europhys. Lett. 4 (1987) 409.
[HK 74] M. Harvey and F.K. Khanna, Nucl. Phys. 221 (1974) 77.
[HM 84] M.S. Hussein and K. McVoy, Prog. Part. Nucl. Phys. 12 (1984) 103.
[HM 85] M.S. Hussein and K. McVoy, Nucl. Phys. A 445 (1985) 124.
[HM 89] M.S. Hussein and R.C. Mastroleo, Nucl. Phys. A 491 (1989) 468.
[HO 89] Y. Hibayashi, S. Okabe and Y. Sakuragi, Phys. Lett. B 221 (1989) 227.
[HP 92] M.S. Hussein and M.P. Pato, Univ. São Paulo Preprint, unpublished.
[HPB 91] M.S. Hussein, M. Pato and C.A. Bertulani, Phys. Rev. C 44 (1991) 2219.
[HRB 91] M.S. Hussein, R.A. Rego and C.A. Bertulani, Phys. Rep. 201 (1991) 279.
[HS 90] A.C. Hayes and D. Strottman, Phys. Rev. C 42 (1990) 2248.
[Hu 84] M.S. Hussein, Phys. Rev. C 30 (1984) 1962.
[Hu 91a] M.S. Hussein, Phys. Rev. C 44 (1991) 446.
[Hu 91b] M.S. Hussein, Nucl. Phys. A 531 (1991) 192.
[Hu 92] M.S. Hussein, M.P. Pato, L.F. Canto and R. Donangelo, Phys. Rev. C, in press.
[Ie 93] K. Ieki et al., Phys. Rev. Lett. 70 (1993) 730.

[Ik 88] K. Ikeda, INS report JHP-7 (1988) [in japanese].
[IMC 89] S. Iljinov, M.V. Mebel and E.A. Cherespanov, in: Proc. Berkeley Conference on Radioactive Beams (World Scientific, Singapore, 1989) p. 289.
[Ja 70] D.F. Jackson, Nuclear Reactions (Methuen, London, 1970).
[Ja 75] J.D. Jackson, Classical Electrodynamics (Wiley, New York, 1975).
[Ja 78] J. Jaras et al., Phys. Rev. C 18 (1978) 2273.
[JJH 90] L. Johanssen, A.S. Jensen and P.G. Hansen, Phys. Lett. B 244 (1990) 357.
[Ka 75] P.J. Karol, Phys. Rev. C 11 (1975) 1203.
[KB 88] A.M. Kobos, M.E. Brandan and G.R. Satchler, Nucl. Phys. A 487 (1988) 457.
[KB 90] T. Kajino and R.N. Boyd, Astrophys. J. 359 (1990) 267.
[Ki 86] Y. Kitazoe et al., Phys. Lett. B 166 (1986) 35.
[Ki 89] J. Kiener, H.J. Gils, H. Rebel and G. Baur, Z. Phys. A 332 (1989) 359.
[Ki 91] J. Kiener et al., Phys. Rev. C 44 (1991) 2195.
[KMF 90] T. Kajino, G.J. Mathews and G.M. Fuller, Astrophys. J. 364 (1990) 7.
[Ko 87] S. Kox et al., Phys Rev. C 35 (1987) 1678.
[Ko 88] T. Kobayashi et al., Phys. Rev. Lett. 60 (1988) 2599.
[Ko 89] T. Kobayashi et al., Phys. Lett. B 232 (1989) 51.
[Ko 91] T. Kobayashi, in: Structure and Reactions of Unstable Nuclei (World Scientific, River Edge, NJ, 1992).
[Ko 92] J.J. Kolata et al., Phys. Rev. Lett. 69 (1992) 2631.
[LB 91] B.-A. Li and W. Bauer, Phys. Lett. B 254 (1991) 335.
[Le 92] M. Lewitowicz et al., GANIL-preprint (1992) to be published.
[LHB 91] B.-A. Li, M.S. Hussein and W. Bauer, Nucl. Phys. A 533 (1991) 749.
[LL 75] L.D. Landau and E.M. Lifshitz, Quantum Mechanics, 4th Ed. (Addison–Wesley, 1975).
[LM 70] W.O. Lock and D.F. Measday, Intermediate Energy Nuclear Physics (Methuen, London, 1970).
[LM 88] R.J. Lombard and J.P. Maillet, Europhys. Lett. 6 (1988) 323.
[LR 84] R. Lindsay and N. Rowley, J. Phys. G 10 (1984) 805.
[LTS 77] W.G. Love, T. Terasawa and G.R. Satchler, Phys. Rev. Lett. 39 (1977); Nucl. Phys. A 291 (1977) 183.
[LW 90] H. Lenske and J. Wambach, KFA Jülich, Annual Report 1990, unpublished.
[Ma 86] G.J. Mathews et al., Nuclei of the line of Stability, eds R.A. Meyer and D.S. Brenner (American Chemical Society, Washington, 1986).
[Ma 88] W.-H. Ma et al., Nucl. Phys. A 477 (1988) 713.
[Ma 90] G.J. Mathews, B.S. Meyer, C.R. Alcock and G.M. Fuller, Astrophys. J. 358 (1990) 36.
[MD 84] G.J. Mathews and F.S. Dietrich, Astrophys. J. 287 (1984) 969.
[MF 88] R.A. Malaney and W.A. Fowler, Astrophys. J. 333 (1988) 14.
[Mi 73] A.B. Migdal, Sov. J. Nucl. Phys. 16 (1973) 238.
[Mi 87] W. Mittig et al., Phys. Rev. Lett. 59 (1987) 1889.
[Mo 71] R. Mohan, M. Damos and W.C. Biedenharn, Phys. Rev. C 3 (1971) 1740.
[Mo 88] K. Möhring, T. Srokowski, D.H.E. Gross and H. Homeyer, Phys. Lett. B 203 (1988) 210.
[Mo 91] T. Motobayashi et al., Phys. Lett. B 264 (1991) 259.
[Mo 92] C.-B. Moon et al., Phys. Lett. B 297 (1992) 39.
[MP 78] M.H. Macfarlane and S.C. Pieper, Argonne National Laboratory report ANL-76-11 (1987).
[MS 84] K.W. McVoy and G.R. Satchler, Nucl. Phys. A 417 (1984) 157.
[OA 87] M. Oka and R.D. Amado, Phys. Rev. C 35 (1987) 1586.
[Or 92] N. Orr et al., Phys. Rev. Lett. 69 (1992) 2050.
[OYS 91] See e.g. Y. Ogawa, K. Yabana and Y. Suzuki, contributions to the Inter. Symp. on Structure and Reactions of Unstable Nuclei (June 1991, Niigata, Japan) p. 20.
[Pa 90] T. Paradellis et al., Z. Phys. A 337 (1990) 211.
[PC 90] L.S. de Paula and L.F. Canto, Phys. Rev. C 42 (1990) 2628.
[PD 81] J.C. Peng, R.M. DeVries and N.J. DiGiacomo, Phys. Lett. B 98 (1981) 244.
[Pl 71] D.J. Plummer et al., Nucl. Phys. A 174 (1971) 193.
[Ra 75] L. Ray, Phys. Rev. C 11 (1975) 1203.
[RB 90] C. Rolfs and C.A. Barnes, Annu. Rev. Nucl. Part. Sci. 40 (1990) 45.
[RC 86] J.O. Rasmussen, L.F. Canto and X.J. Qiu, Phys. Rev. C 33 (1986) 2033.
[Ri 92] K. Riisager et al., Nucl. Phys. A 540 (1992) 365.
[Ro 81] R.G. Robertson et al., Phys. Rev. Lett. 47 (1981) 1867.
[Sa 79] G.R. Satchler, Nucl. Phys. A 329 (1979) 233.
[Sa 89] Y. Sakuragi, Phys. Lett. B 220 (1989) 22.
[Sa 90] K.E. Sale et al., Phys. Rev. C 41 (1990) 2418.
[Sa 91] G.R. Satchler, private communication.
[SB 82] Fl. Stancu and D.M. Brink, Phys. Rev. C 25 (1982) 2450.

[SBB 92] R. Shyam, P. Banerjee and G. Baur, Nucl. Phys. A 540 (1992) 341.
[Sc 85] D.N. Schramm, Nature 317 (1985) 386.
[Se 47] R. Serber, Phys. Rev. 72 (1947) 1008.
[Sh 89] W.-Q. Shen et al., Nucl. Phys. A 491 (1989) 130.
[Sh 91] S. Shimoura et al., contributions to the Inter. Symp. on Structure and Reactions of Unstable Nuclei (June 1991, Niigata, Japan) p. 19.
[SH 90] H. Sagawa and M. Homma, Phys. Lett. B 234 (1990) 534.
[Si 90] R.H. Siemssen, in: Proc. Inter. Nuclear Physics Conference (São Paulo, Brazil, 1990) eds. M.S. Hussein et al. (World Scientific, Singapore, 1990) p. 569.
[SI 90] Y. Suzuki, K. Ikeda and H. Sato, Prog. Theor. Phys. 83 (1990) 180.
[SL 89] M.G. Saint-Laurent et al., Z. Phys. A 332 (1989) 457.
[SMH 91] G.R. Satchler, K.W. McVoy and M.S. Hussein, Nucl. Phys. A 552 (1991) 621.
[SY 83] Y. Sakuragi, M. Yashiro and M. Kamimura, Prog. Theor. Phys. 70 (1983) 1047.
[St 89] E. Stiliaris et al., Phys. Lett. B 223 (1989) 291.
[Su 91] Y. Suzuki, Nucl. Phys. A 528 (1991) 395.
[Su 92] A. Sustich, Z. Phys. A 342 (1992) 31.
[SW 77] D.N. Schramm and R.V. Wagoner, Annu. Rev. Nucl. Sci. 27 (1977) 37.
[Ta 85a] I. Tanihata et al., Phys. Lett. B 160 (1985) 380.
[Ta 85b] I. Tanihata et al., Phys. Rev. Lett. 55 (1985) 2676.
[Ta 88] I. Tanihata, Nucl. Phys. A 478 (1988) 795C.
[Ta 92] I. Tanihata, private communication.
[TDA 87] L. Tomio, A. Delfino and S.K. Adhikari, Phys. Rev. C 35 (1987) 441.
[Te 88] N. Teruya, H. Dias and A.F.R. de Toledo Piza, unpublished.
[Te 91] N. Teruya, C.A. Bertulani, S. Krewald, H. Dias and M.S. Hussein, Phys. Rev. C 43 (1991) R2049.
[Th 75] C. Thibault, R. Klapisch, C. Rigaud, A.M. Poskanger, R. Prieels, L. Lessard and W. Reisdorf, Phys. Rev. C 12 (1975) 644.
[TLM 87] A. Tellez, R.J. Lombard and J.P. Maillet, J. Phys. G 13 (1987) 311.
[To 87] A.F.R. de Toledo Piza, Rev. Bras. Fis. 17 (1987) 195.
[TS 90] Y. Tosaka, Y. Suzuki, Nucl. Phys. A 512 (1990) 46.
[TS 91] N. Takigawa and H. Sagawa, Phys. Lett. B 265 (1991) 23.
[TUK 92] N. Takigawa, M. Ueda, M. Kuratani and H. Sagawa, Phys. Lett. B 288 (1992) 244.
[Ut 90a] H. Utsunomiya et al., Phys. Lett. 65 (1990) 847; Nucl. Phys. A 511 (1990) 379.
[Ut 90b] H. Utsunomiya, Phys. Rev. C 27 (1990) 1309.
[VA 80] B.J. VerWest and R.A. Arndt, Phys. Rev. C 25 (1980) 1979.
[WA 79] A. Winther and K. Alder, Nucl. Phys. A 319 (1979) 518.
[Wa 84] T.P. Walker et al., Astrophys. J. 281 (1984) 493.
[WFF 67] R.V. Wagoner, W.A. Fowler and F. Hoyle, Astrophys. J. 148 (1967) 3.
[Wi 75] K.H. Wilcox, R.B. Weisenmiller, G.J. Wozniak, N.A. Jelly, D. Ashery and J. Cerny, Phys. Lett. B 59 (1975) 142.
[Wo 88] J.M. Wouters, R.H. Kraus, D.J. Vieira, G.M. Butler and K.E. Löbner, Z. Phys. A 331 (1988) 229.
[WSK 89] M. Wiescher, R. Steininger and F. Kappeler, Astrophys. J. 344 (1989) 464.
[WW 81] R.K. Wallace and S.E. Woosley, Astrophys. J. Suppl. 45 (1981) 289.
[Ya 89] T. Yamagata et al., Phys. Rev. C 39 (1989) 873.
[YOS 92a] K. Yabana, Y. Ogawa and Y. Suzuki, Nucl. Phys. A 539 (1992) 295.
[YOS 92b] K. Yabana, Y. Ogawa and Y. Suzuki, A 543 (1992) 722.
[Zh 91a] M.V. Zhukov, B.V. Danilin, D.V. Federov, J.S. Vaagen, F.A. Gareev and J.M. Bang, Phys. Lett. B 265 (1991) 19.
[Zh 91b] M.V. Zhukov et al., Nucl. Phys. A 529 (1991) 53; Nucl. Phys. A 539 (1992) 177.

Note added in proof

Note to section 2.4.3. Recently, Ieki et al. [Ie 93] have performed elaborate triple coincidence measurements of the Coulomb dissociation of ^{11}Li. As predicted in the theoretical papers quoted in section 2.4.3, the experiment indicates that higher order electromagnetic processes (reacceleration effect) are relevant. In fact, the semiclassical method described in this section has been applied [CDS 92] to obtain theoretical predictions for the fragment energy spectrum and longitudinal velocity distribution, which were obtained by Ieki et al. [Ie 93]. Theory and experiment are in good agreement.

The results of Ieki et al. [Ie 93] on the reacceleration effect seem to indicate that the breakup of ^{11}Li is more likely to occur via a direct breakup mechanism than via the excitation of a resonant state in the continuum; i.e., the peak in the dipole response function dB/dE (see, e.g., fig. 4) should be interpreted as a threshold effect rather than a resonance. This was indeed suggested by Bertulani and Baur [BB 88a]. However, the conclusions of Ieki et al. [Ie 93] are based on classical considerations.

Recently, Bertsch and Bertulani [GB 92] have addressed this problem by solving the time dependent Schrödinger equation nonperturbatively. For simplicity, a one-dimensional model for the reaction was used. The conclusion was that even when the breakup proceeds via the excitation of a resonance, the reacceleration effect is larger than expected from the naive classical model. In view of the potential importance of reacceleration both as a measuring tool and as an obscuring agent for the measurements of Coulomb breakup, more experimental and theoretical studies are clearly necessary.

As a final remark, we quote the work of Bertulani and Sagawa [BS 92b] on the nuclear excitation of multipole states in neutron-rich nuclei. They predict cross sections for soft multipole excitation of order of 100 mb/sr at forward angles in reactions at beam energies in the range 30–70 MeV/nucleon. It might be possible to distinguish the multipoles experimentally by the angular dependence at very forward angles.

Note to section 3.1.4. We end this section with few remarks concerning the recent data on the elastic scattering of ^{11}Li + ^{12}C and ^{11}C + ^{12}C at 60 MeV A published by Kolata et al. [Ko 92]. These authors confirmed, to a large extent, the predictions of Satchler et al. [SMH 91]. The ratio of the cross section to Rutherford, was found to be three times larger in ^{11}Li + ^{12}C as compared to that of ^{11}C + ^{12}C. If the cross sections themselves were compared (not their ratio to Rutherford) the enhancement in ^{11}Li + ^{12}C is found to be about 1.4. Both angular distributions are, as anticipated, far-side dominated and may exhibit a nuclear rainbow effect.

The Airy minimum predicted by Satchler et al. at $\theta \cong 14°$ was, however not found. The analysis performed by Kolata et al. also confirmed the need to include a weak, long-range, absorptive potential, to account for the measured reaction cross section.

Similar conclusions were reached by the GANIL group [Le 92]. These authors measured the angular distributions of ^{7}Li and ^{11}Li elastic scattering from ^{28}Si at $E_{lab} = 29$ MeV A. The ^{11}Li cross section was found to be far-side dominated and the need for a long-range breakup absorptive potential was clearly pointed out when the reaction cross section was extracted.

Note to section 3.2.2. Recently, the proton elastic scattering from the neutron-rich nuclei, ^{9}Li and ^{11}Li at $E_{lab} = 60$ and 62 MeV A under the inverse kinematical conditions has been reported by the RIKEN group [Mo 92].

In contrast to the heavy-ion experiment of Kolata et al. [Ko 92], the proton scattering was found to be basically influenced by absorption. In fact, Moon et al. [Mo 92] reported an appreciable reduction of the p + ^{11}Li cross section as compared to that of p + ^{9}Li. Our calculation above does not give such a reduction. The reason is the importance of the breakup channel in the ^{11}Li scattering, which we did not take into account.